

UNIVERSIDAD AUTÓNOMA DE MADRID
Department of Theoretical Condensed Matter Physics

**Modeling peak interaction forces of soft matter
with dynamic AFM in liquid**

by

Horacio Andrés Vargas Guzmán

Doctoral thesis

A thesis submitted to the Universidad Autónoma de Madrid in
accordance with the requirements of the degree of Ph.D. in Physics.

Supervised by: Prof. Ricardo García García

Instituto de Ciencia de Materiales de Madrid
Consejo Superior de Investigaciones Científicas
December 10, 2014

*A la memoria de mis abuelos,
a mis padres
y al porvenir de mis sobrinos (meine goldschaetze)*

Abstract

The atomic force microscope (AFM) is an instrument that has revolutionized the field of nanoscience and nanotechnology by enabling the characterization and manipulation of materials with nanometer (one billionth of a meter), molecular and atomic resolution. In the last 28 years a variety of experimental AFM techniques have been developed that go from contact to dynamic AFM modes or from working in air to liquid environments. A relevant research avenue within dynamic AFM modes is devoted to the generation of atomic and molecular resolution images of soft materials¹ in liquid environments. Whereby different applications are envisioned into areas of medicine (*nanomedicine*) and advanced materials. The research presented here focus on two dynamic AFM methods: amplitude modulation AFM (AM-AFM) and Bimodal AM. This thesis describes the study of the peak interaction forces of soft materials under low- Q environments imaged with AM-AFM and Bimodal AM. The peak/maximum interaction forces have been chosen because it rapidly enables tracking into the degree of invasiveness on the sample, its deformation and hence its resolution while imaging. This thesis proposes a theoretical modeling framework that can be divided in two closely related parts. The first part aims to refine the tip-sample interaction modeling for the description of elastic and viscoelastic phenomena of soft materials. The second part aims to obtain high-resolution imaging conditions from the numerical simulations of the dynamics of the cantilever-tip motion in liquid for an extensive range of dynamic AFM operational parameters and materials.

Chapter 1 contains a description of the instrument components and its most common operation modes. Followed by, the introductory concepts regarding high-resolution imaging, as well as, its state-of-the-art while imaging in liquid. Then, a brief definition of the physics of soft materials is provided. The motivation of this thesis is also presented.

Chapter 2, describes the mathematical modeling of the cantilever-tip as a point mass and also as a modified Euler-Bernoulli beam. Then, introduces the common used tip-sample interaction models, emphasizing the description of the contact mechanical and

¹The term soft materials in this thesis is referred to the mechanical properties of polymeric surfaces and biological systems (isolated or packed arrays of proteins) within Young moduli of 10-500 MPa.

viscoelastic force models. It also introduces an in-house developed simulations platform for modeling single and multifrequency dynamic force microscopy situations according to the framework described within this Chapter.

Chapter 3, it introduces the frequency dependent behaviour of conservative and non conservative forces within AM-AFM. Moreover, it describes the key variables of AM-AFM to study a viscoelastic material. In addition a method has been proposed to reconstruct the peak viscoelastic forces in time domain. Finally, an expression for estimating the contact time between tip and sample in AM-AFM is presented.

Chapter 4, shows the interplay of AM-AFM operational parameters to obtain high-resolution images of soft material in liquid. In addition an extensive study has been carried out to obtain the peak force dependence on each operational parameter (A_0 , A_{sp} , k). Furthermore, the observed phenomena of such study have been described by comparing soft and relatively rigid materials.

Chapter 5, contains a new scaling-law expression obtained for estimating the peak forces of soft materials in low-Q environments. It also contains a comparison of the former analytical expressions to estimate the force in AM-AFM and also numerical simulations of the Tatara and the Hertz contact mechanics models.

Chapter 6, reveals the behaviour of the peak interaction forces in Bimodal AM force microscopy in liquid within the range of soft materials described in this thesis framework. Moreover, it shows how the peak forces in Bimodal AFM can be more gently modulated varying A_{02} instead of A_{sp1} .

Finally, the Appendixes A and B are extensions to Chapters 2 and 5, respectively. Appendix A contains a introduction and description to the dynamic AFM simulator (dForce) and also provides an outlook for this scientific computing tool. Appendix B provides the details of the multivariate regression analysis performed to obtain the scaling-law expression for estimating the peak forces of soft materials in low-Q environments.

Resumen

El microscopio de fuerzas atómicas (AFM) es un instrumento que ha revolucionado el campo de la nanociencia y nanotecnología, ya que ha permitido la caracterización y manipulación de materiales con resolución nanométrica (una billonésima de metro), molecular y atómica. En los últimos 28 años se han desarrollado varias técnicas experimentales en microscopía de fuerzas. Las mismas pasan por distintos modos de operación, ya sean estos en AFM en modo contacto o dinámico y por su versatilidad de trabajo en aire o en líquidos. Una de las vetas de investigación más relevantes dentro de la microscopía de fuerzas en modo dinámico está orientada a la obtención de imágenes con resolución atómica y molecular de materiales blandos² en líquidos. Dentro de dicha area de investigación ya se han visionado distintas aplicaciones en campos como la medicina (nanomedicina) y materiales avanzados. El trabajo de investigación presentado en esta tesis doctoral está enfocado en dos métodos dinámicos de microscopía de fuerzas: en amplitud modulada (AM-AFM) y Bimodal AM. Este trabajo constituye el estudio de las fuerzas pico de materiales blandos en ambientes con Q -bajos desde imágenes obtenidas en AM-AFM y Bimodal AM. La fuerza pico o máxima ha sido elegida, ya que esta permite rastrear el grado de invasividad sobre una muestra, su deformación y por tanto su resolución durante la obtención de una imagen de AFM. En la presente tesis doctoral se propone un marco de modelización que se divide en dos partes interrelacionadas. La primera tiene como objetivo el uso de nuevos modelos de interacción entre punta y muestra para describir fenómenos elásticos y viscoelásticos en materiales blandos. La segunda parte tiene el fin de proporcionar las condiciones de trabajo para la obtención de imágenes con alta resolución a través de simulaciones numéricas de la dinámica del sistema palanca-punta para una extensa cantidad de parámetros operacionales y propiedades de materiales.

En el capítulo 1 se describen los elementos del instrumento y sus modos de operación más comunes. A continuación se hace una introducción a los conceptos básicos sobre la toma de imágenes con alta resolución. Así mismo se presenta el *state-of-the-art* en

²En esta tesis doctoral el término material blando se refiere al rango de módulo de Young entre 10-500 MPa, donde se encuentran las propiedades mecánicas de materiales poliméricos o sistemas biológicos (proteínas aisladas y/o empaquetadas).

la toma de imágenes en líquidos. También se define brevemente la física de materiales blandos. Por último se presenta la motivación de esta tesis doctoral.

En el capítulo 2 se describen los modelos matemáticos del sistema palanca-punta como ser: el de masa puntual y la teoría de Euler-Bernoulli. También se introducen los modelos de interacción entre punta y muestra, haciendo énfasis en la descripción de los modelos de contacto y viscoelasticidad. Así mismo, se introduce la plataforma de simulación desarrollada durante esta tesis para modelar la dinámica del microscopio de fuerzas en modo dinámico, ya sea este mono y/o multimodal (de acuerdo al marco teórico descrito en este capítulo).

El capítulo 3 introduce la dependencia en frecuencia de las fuerzas conservativas y disipativas en AM-AFM. Adicionalmente, se describen las variables clave de AM-AFM que permiten la interacción del instrumento con un material viscoelástico. También se presenta un método para reconstruir las fuerzas pico viscoelásticas dentro del dominio del tiempo. Finalmente se obtiene una ecuación para estimar el tiempo de contacto entre punta y muestra en AM-AFM.

En el capítulo 4 se obtienen los parámetros operacionales (A_0 , A_{sp} y k) necesarios para obtener imágenes de muestras blandas en líquidos con alta resolución. Así mismo se describen los fenómenos físicos que conllevan dicho estudio mediante comparaciones entre muestras blandas y relativamente rígidas.

En el capítulo 5 se presenta una nueva expresión analítica para estimar las fuerzas pico de materiales blandos en medios de Q -bajos basada en el modelo de Tatara. También contiene comparaciones preliminares de los modelos existentes para obtener la fuerza de interacción en AM-AFM y las simulaciones numérica para dos modelos de mecánica de contacto: Hertz y Tatara.

El capítulo 6 extiende las simulaciones numéricas hechas en AM-AFM a Bimodal AM y muestra el comportamiento de las fuerzas pico de materiales blandos en medio líquido como una función de las variables: A_{02} , A_{sp1} y k . Mediante dicho análisis se observa como la fuerza pico puede ser modulada de forma más suave variando A_{02} en lugar de A_{sp1} .

Por último, de los dos apéndices incluidos en la tesis, el apéndice A recoge detalles de diseño, desarrollo y perspectivas del simulador de AFM en modo dinámico presentado dentro del capítulo 2. Por su parte el apéndice B presenta detalles sobre la regresión de múltiples variables realizada para obtener la expresión de la fuerzas pico basada en el modelo de Tatara y presentada previamente en el capítulo 5.

Acknowledgements

This thesis would not have been possible without the financial and scientific support of the *ForceTool* group, headed by Prof. Dr. Ricardo García who has abundantly enriched my knowledge through scientific discussions. Deepest gratitude are also due to my advisor Prof. Dr. Rubén Pérez, for his revision and feedback. Backwards in time, I would like to acknowledge Lic. Nestor Avilés, who was the first authentic scientist I have ever met. He encouraged me to study physics besides my engineering major. I would like to thank essentially the CSIC and the Consolider Project *Force-For-Future* for providing me financial means like the top-notch simulation clusters used for the simulations along this thesis. The whole *R&D* ambiance of the UAM campus, has been the perfect place to discover little faculty libraries and also interact with people of diverse scientific background.

Personally, I want to express my love and gratitude to my entire family. Patricia, Gonzalo and Alejandra, for their endless love and being always the example to follow. Papá Mario and Mamá Irma, I will never forget those sunny days at the balcony. I would also like to thank my great aunts: Blanca and Dora; my aunts and uncles: Juanita, Beatriz, Pancho and Américo; my cousins, nieces and Lenka for their understanding and being always supportive of me and my endeavors. Special thanks also to my colleagues José Luis, Marco, Marta, Herr Dr. Dietz, Elena, Guilherme, Yu Kyoung, Jorge, Alma, Dani, Amir, Ana, Pablo and Fran for sharing their knowledge and invaluable assistance. Moving a bit towards the southern hemisphere. I want to thank my friends Sergio, Negrita, Monique, Micaela, Cayo, Nelson, Miryam, Niels, Caro, Ebe, Simeon, Javier, Rho, Cecilia, Marco, Andres and coming back to the northern hemisphere, the people from the ETH Zürich, Raphael, Lea, David and Barbara. Back to Spain, I would further like to thank my Master's colleagues: Joselo, Ana, Diego, Giovanni (specially for showing me the world of HPC languages), Juanpe, JL, as well as, my sports comrades: the bloody runners, the ICMC basketballers and the tennis players from 3 Cantos. Once in 3C, I would like also to thank my former colleagues that built such a close atmosphere over there. Yuspayarpan taqikunata!

Contents

List of symbols	XV
List of acronyms	XIX
1 Introduction and Motivation	1
1.1 Introduction	1
1.2 Atomic Force Microscope	2
1.3 Contact mode AFM	3
1.4 Dynamic modes	4
1.4.1 Amplitude modulation AFM	4
1.4.2 Frequency modulation AFM	6
1.4.3 Bimodal AFM	7
1.5 Concepts and conditions for high-resolution imaging	9
1.6 Physics of soft matter in AFM	11
1.7 State-of-the-art of high resolution AFM images in liquid	13
1.8 Motivation	13
2 Cantilever tip dynamics	15
2.1 The dynamics of the harmonic oscillator	15
2.2 The point-mass model in dynamic AFM	17
2.2.1 Dynamic AFM non-linearities	18
2.3 Extended Euler-Bernoulli equation	19
2.3.1 Euler-Bernoulli equation without interaction forces	20
2.3.2 Equivalence to the point-mass model	21
2.4 Introduction to tip-surface interaction forces F_{ts}	23
2.4.1 Hertzian mechanics	24
2.4.2 Electrostatic interactions (DLVO)	29
2.4.2.1 van der Waals forces	30
2.4.2.2 Electrical double layer forces	30
2.4.3 Viscoelastic forces	31
	XI

2.4.3.1	Creep	31
2.4.3.2	Stress relaxation	31
2.4.4	Interaction forces between tip and soft samples	32
2.4.4.1	Standard linear solid model	32
2.4.4.2	The Tatara model	34
2.5	Force microscopy simulator: dForce	37
3	Unmasking time-dependent viscoelastic forces	39
3.1	Introduction to time-dependent viscoelastic forces	39
3.1.1	Frequency dependent oscillation amplitude in AM-AFM	40
3.1.2	Frequency dependent viscoelastic samples: energy dissipation of polymeric samples	41
3.1.3	Viscoelastic material in response to a sinusoidal excitation	44
3.1.4	Contact time of a viscoelastic material in response to the dynamic AFM tip motion	46
3.2	Quantification of the viscoelastic interaction force from a piecewise material excitation	47
3.3	Observables of the time-dependent viscoelastic force reconstruction	52
3.3.1	AM-AFM phase shift ϕ	53
3.3.2	Maximum deformation δ_{max}	53
3.3.3	Contact time t_c	54
3.3.3.1	Estimation of the contact time t_c by means of the loss tangent for the Kelvin-Voigt model	54
3.4	Conclusions	56
4	Peak Forces in Amplitude Modulation AFM in Liquid	59
4.1	Peak forces and high-resolution imaging of soft-matter in liquid	59
4.1.1	Peak forces modeling for Hertz and Tatara contact mechanics models	59
4.2	Peak forces dependence on the set-point amplitude A_{sp}	61
4.3	Permanent contact and the degree of invasiveness	63
4.3.1	Sample deformation in terms of E_s , A_0 and R_t	63
4.4	Peak forces dependence on the force constant k	63
4.5	Interplay between operational conditions, the peak forces and soft matter mechanical properties	65
4.6	High-resolution imaging of molecular process and antibodies	66
4.6.1	Force estimation of molecular process imaging	66
4.6.2	Molecular resolution images of IgM antibodies in liquid	67
4.6.3	Conclusions	69

5	Scaling laws to estimate peak forces for soft-matter in liquid	71
5.1	Introduction to the estimation of the peak forces for soft matter in liquid	71
5.2	Numerical simulations and scaling laws in dynamic AFM	72
5.2.1	Solving the microcantilever-tip equations of motion	72
5.2.2	Preliminary comparison of simulated and analytical peak force values: Dependence on the Young modulus and the set-point amplitude	73
5.3	Free amplitudes and lateral resolution at small peak forces	76
5.4	Parametrized expressions to estimate peak forces for soft matter in liquid	78
5.4.1	Probing the accuracy of scaling laws for soft materials in liquid	79
5.4.2	Peak forces dependence on the sample Young modulus	80
5.5	Conclusions	81
6	Peak forces in Bimodal AFM	85
6.1	Introduction	85
6.2	Modeling bimodal force microscopy in liquid	86
6.3	Backbone aspects of Bimodal AM force microscopy in liquid	88
6.3.1	Experimental Bimodal AM in liquid	88
6.3.2	Peak forces in Bimodal AM force microscopy	88
6.4	Bimodal AFM interplay of the peak interaction forces with k_1 , A_{01} and E_s	93
6.5	Conclusions	100
7	Conclusions	101
7.1	Conclusions	101
7.2	Conclusiones	104
A	Interactive platform for understanding force microscopy experiments	107
A.1	Introduction	107
A.2	Simulator back and front-end design	108
A.2.1	Performance in scientific computing	108
A.3	Outlook and discussion	110
B	Expression to estimate the peak forces of soft material in liquids	111
B.1	Asymptotic approximations of the peak interaction forces of soft material in liquids	111
B.1.1	Multivariate regression analysis	111
	Bibliography	113
	Publications	129

List of symbols

$V_{A,B,C,D}$	Voltage of the four photodiode quadrants
z_0	Cantilever deflection
z_c, z_p	Tip-sample average distance (piezo distance)
F_{ts}	Tip-sample interaction forces
k	Cantilever's spring constant
A_0, A_{far}	Free/far amplitude of oscillation
f_0, f_{far}	Free/far resonance frequency
A_{sp}	Set-point amplitude
Δf	Frequency shift
f_{near}	Oscillation frequency whenever the tip is near to the surface
A_{near}	Oscillation amplitude whenever the tip is near to the surface
S	Area of contact between two interacting bodies
F	General force term
σ	Stress between two interacting bodies given by $\sigma = \frac{F}{S}$
l_0	Initial length of an elastic body
$\Delta l, \delta$	Deformation
E	Material's Young modulus
U	General energy term
a_{mol}	Molecular length-scale
a_{smol}	Supramolecular length-scale
k_B	Boltzmann constant
T	Temperature given in Kelvin
m	Mass of the microcantilever-tip system
$z(t)$	Instantaneous tip position
$\dot{z}(t)$	Instantaneous tip velocity
$\ddot{z}(t)$	Instantaneous tip acceleration
A	Oscillation amplitude
ω_0	Angular resonance frequency, given by $\omega_0 = 2\pi f_0$
ϕ	Phase shift
z_i	Initial tip position
v_i	Initial tip velocity

Q	Quality factor
γ	Damping factor given by $\gamma = \frac{m\omega_0}{Q}$
ω	Generic angular frequency
ω_d	Driven angular frequency
F_0	Force corresponding to the free resonance amplitude
$\Delta\omega$	Angular frequency shift
F_{exc}	Driven/excitation force given by $F_{exc} = F_0 \cos(\omega_d t)$
$d(t)$	Instantaneous tip-surface separation distance
$\dot{d}(t)$	Instantaneous tip-surface separation velocity
$\ddot{d}(t)$	Instantaneous tip-surface separation acceleration
m_{eff}	Effective cantilever-tip system mass
F_c	Conservative forces
F_{nc}	Non-conservative/dissipative forces
ρ_{env}	Medium density
ρ_c	Cantilever's material density
L_c	Cantilever's length
W_c	Cantilever's width
Th_c	Cantilever's thickness
E_c	Cantilever's Young modulus
I	Area moment of inertia
H	Hamaker's constant
R_t	Tip's radius
R_s	Sample's radius
F_{hydro}	Hydrodynamic forces
F_{sum}	Sum of forces given by $F_{sum} = F_{exc} + F_{ts} + F_{hydro}$
M_y	Moment of inertia in the 'y' axis
$\phi_n(x)$	n th Eigenmode modal shape
$w(x, t)$	Deflection of the cantilever beam at position x and time t
μ	Mass per unit area
$Y_n(t)$	n th eigenmode time dependent cantilever behaviour
ω_n	n th eigenmode resonance frequency
α_n	n th eigenvalues corresponding to the n th resonance frequency
ϕ_m	m th orthogonal modal shape
δ_{nm}	Kronecker's delta of the orthogonal n th and m th modal shapes
E_k	Kinetic energy
E_e	Elastic energy
a_{int}	Internal damping coefficient of the cantilever
a_{ext}	Hydrodynamic damping of the cantilever beam due to the fluid surrounding it

$z_n(t)$	n th tip's deflection
m_c	Cantilever-tip system mass given by $m_c = \rho_c W_c L_c T h_c$
m_n	n th cantilever-tip system mass
γ_n	n th damping coefficient
Q_n	n th quality factor
k_n	n th cantilever's spring constant
$\langle F_{ts} \rangle$	Tip-sample average force
a_c	Tip-sample contact radius
E_t	Tip's Young modulus
E_s	Sample's Young modulus
ν_t	Tip's Poisson ratio
$w(r)$	Vertical displacement of the sample at position r
$w_i(r)$	Vertical displacement of the i th body in contact at position r
P	Pressure
R^*	Effective radius of the tip and sample in contact given by $\frac{1}{R^*} = \frac{1}{R_s} + \frac{1}{R_t}$
s	Radial coordinate of the contact area of 2 bodies
θ	Angle of s to r (variable contact radius)
μ_T	Tabor's number
χ	Surface charge interfacial energy
γ^s	Surface interfacial energy
z_{eq}	Equilibrium interfacial separation
c	Cohesive parameter
ζ_{th}	Dugdale's potential
λ	Lame's coefficient
λ_D	Debye's length
e	Electron's charge
ϑ	Electron's valency
ϵ_0	Dielectric constant of vacuum
ϵ	Relative dielectric constant of the medium
C_i	Concentration of ions
ϵ	Strain
ϵ_0	Maximum strain
$\dot{\epsilon}$	Strain rate
$\dot{\delta}$	Deformation rate
E_0	Material's instantaneous ($t = 0$) Young modulus
E_∞	Material's infinite ($t = \infty$) Young modulus
$J(t)$	Time dependent creep compliance of a linear viscoelastic solid
$U_s(z, r)$	Lateral displacement of the sample at lateral (r) and vertical positions (z)
$w_i(z, r)$	Vertical displacement of the sample

L_i	Lateral equilibrium body stiffness
K_i	Vertical equilibrium body stiffness
n	Tatara's model vertical constitutive parameter
n_c	Tatara's model lateral constitutive parameter
k_{eff}	Effective spring constant according to the weakly perturbed oscillator
k_{eff}^l	Left shift due to a positive force gradient (dF_{ts}/dz)
k_{eff}^r	Left shift due to a negative force gradient (dF_{ts}^r/dz)
$\tan \delta$	Loss tangent
G_s	Storage modulus
G_l	Loss modulus
η	Viscous coefficient
σ	Stress
σ_0	Maximum applied stress
$\dot{\sigma}$	Stress rate
τ	Restitution/relaxation time
τ_{sls}	Restitution/relaxation time of the standard linear solid model (SLS)

List of acronyms

STM Scanning Tunneling Microscope

AFM Atomic Force Microscope

SPM Scanning Probe Microscopy

AM-AFM Amplitude Modulation Atomic Force Microscopy

FM-AFM Frequency Modulation Atomic Force Microscopy

MF-AFM Multifrequency Atomic Force Microscopy

HS-AFM High-Speed Atomic Force Microscopy

PLL Phase Locked Loop

OBD Optical Beam Deflection

CA Constant Amplitude (rel. to FM-AFM)

CE Constant Excitation (rel. to FM-AFM)

PI Proportional Integral controller

UHV Ultra-High Vacuum

ODE Ordinary Differential Equation

SHO Simple Harmonic Oscillator

LRF Long Range Forces

SRF Short Range Forces

FFT Fast Fourier Transform

LCM Least Common Multiple

SLS Standard Linear Solid

HPC High Performance Computing

Chapter 1

Introduction and Motivation

1.1 Introduction

In condensed matter physics, the nanoscale refers to the boundary length scale between atoms and the continuum world. The relevance of exploring phenomena occurring at the nanoscale has motivated researchers to develop different types of microscopes that could achieve nanometer resolution. In 1981, Gerd Binnig and Heinrich Rohrer invented the scanning tunneling microscope (STM) [1]. The STM provides sub-angstrom resolution and it is capable of imaging and manipulating surfaces at an atomic scale using the tunneling current between a conducting tip and a conducting sample. The tip is mechanically moved across the sample and the feedback system controls the tunneling current constant by varying the height of the tip. By gathering the data of the tip height and its coordinates, a 3D image of the surface topography can be built. The main constraint of this microscope is that the sample surface must be conductive.

Five years later, in 1986 Binnig, Quate and Gerber [2] invented the Atomic Force Microscope (AFM); the first microscope with atomic resolution that is capable of imaging non-conductive samples in air, liquid or vacuum environments. Since then, the development of new techniques has been engaged to new challenges, such as: surface properties quantification at the nanoscale, high-resolution imaging of soft and stiff samples, sub-surface images acquisition, high-speed images acquisition, molecular and atomic manipulation of surfaces, among others. In the field of life sciences, the AFM has opened doors to novel research results, such as: high-resolution imaging of single antibodies in the air and liquid [3, 4], observing sub-molecular structure and conformational changes of protein networks in biological membranes [5, 6, 7, 8, 9, 10], testing theoretical models on the basic structure of materials at an atomic scale [11, 12, 13], topological structures reconfiguration of DNA (DNA origami) [14], visualization of myosin motion over actin fibers [15], among others.

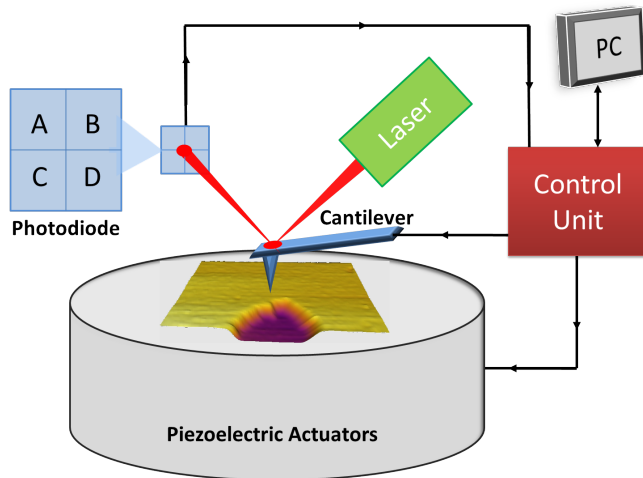


Figure 1.1: AFM scheme, depicting all the main components: the cantilever, the optical beam deflection (photodiode and laser), the piezoelectric actuators, the control unit and the Personal Computer (PC).

1.2 Atomic Force Microscope

The atomic force microscope falls under the category of microscopes known as **scanning probe microscopes** (SPM). These microscopes can achieve sub-nanometer resolution by mechanically scanning a sharp probe across the surface in a raster pattern while being sensible to the interacting forces between the probe and the surface. To this end, the AFM uses a microcantilever with a sharp tip attached at its free end, typically the tip radius is between 2 and 100 nm. The tip radius is of great importance for modeling its tip-surface interaction forces [16, 17] and hence elucidating their diverse nature, i.e.: elastic, viscous, electrostatic, hydrodynamic, magnetic, chemical, among others.

Those interaction forces are detected by accurately measuring the angle that the microcantilever has been deflected. The angle is measured using optical techniques, typically optical beam deflection (OBD) [18], where a laser beam is focused on the backside of the microcantilever and reflected onto a photodiode as shown in figure 1.1.

Figure 1.1 shows a detail of the photodiode, composed of four quadrants (A, B, C and D). Here, the corresponding amount of photons collected on each region are transduced into voltages: V_A , V_B , V_C and V_D . A combination of these four voltages is measured and converted to either vertical displacement (deflection) or lateral displacement (torsion). In order to adjust the height from the microcantilever to the surface and the microcantilever position on the XY -plane ceramic piezoelectric actuators are used. In AFM, piezo-

electric actuators can normally reach sub-nanometer precision by changing its size in response to the electrical potential placed across them. This effect is also known as inverse piezoelectricity. Eventually, the same inverse piezoelectric effect could be used to excite acoustically the microcantilever from its clamped base [19]. Nonetheless, for liquid environments other excitation methods are more suitable, such as the magnetic [20, 21, 22] or the photothermal methods [23, 24].

The accuracy of the AFM control system determines the quality of the imaging process. It is important to control the detected signal in such a manner that the image profile can be tracked continuously. This step can be achieved once the control system has gathered the operational parameters chosen previously by the AFM user and measures the feedback parameter (e.g. the deflection z_0 for the contact operation mode described in section 1.3). Then, the control system uses a feedback mechanism to change the Z -axis accordingly and thus maintaining the operational parameters set previously. It is important to note that the feedback parameters depend on the operation mode of the microscope [25].

Likewise, the information of apparent height in the Z -axis and the position in the XY -plane are gathered by a computer and then displayed as a topography image. The computer also provides an interface between the electronics and the AFM user. Nowadays, the operation mode can be also selected by the AFM user through the microscopes software suite. The most used operation modes are described in the next sections 1.3 and 1.4.

1.3 Contact mode AFM

Contact mode AFM was the original operation mode proposed by Binnig, Quate and Gerber [2]. The tip is brought into mechanical contact with the surface by means of the piezo distance z_c which produces a sample deformation ($\delta = z_c + z_0$) depending on its mechanical properties. Once in contact, the microcantilever starts to move across the surface and the AFM control system attempts to maintain a constant microcantilever deflection z_0 (see figure 1.2). The control system moves the piezoelectric actuator in the Z -axis by means of distance z_c until the fixed deflection value is fulfilled. This procedure is repeated on each point (pixel) of the surface until the topographical information of the image has been gathered. The interaction forces related to this imaging mode are purely repulsive, *i.e.* $F_{ts} > 0$ as depicted in figure 1.3. In the Z -axis, the total force obeys a linear dependence with the cantilever deflection (z_0), given by Hooke's law $F_{ts}(z_c + z_0) = -kz_0$. In addition to the microcantilever deflection, this operation mode also involves a well resolved lateral component. The lateral movement of the microcantilever is not being controlled by the instrument. Hence, the presence of lateral forces could make non-destructive imaging of soft materials a much more complex task

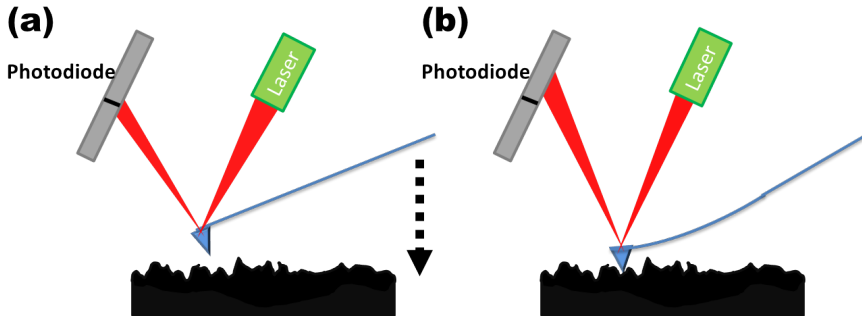


Figure 1.2: Scheme of the microcantilever, the optical beam detection system and a profile of a sample surface. (a) The microcantilever tip is brought into mechanical contact with the sample and (b) in contact mode while the sample is scanned the deflection of the cantilever is measured through the displacement of the beam on the photodiode.

to achieve. Being aware of this issue has motivated the AFM community in developing new imaging modes, such as the dynamics modes.

1.4 Dynamic modes

In dynamic AFM mode, the microcantilever tip oscillates in close proximity to the *surface-plane* where the tip-surface forces affect the microcantilever vibration. The resulting cantilever tip motion close to the surface can be approximated to a sinusoidal signal [16] (more details are given along Chapter 2),

$$z(t) = A \cos(\omega t - \phi) \quad (1.1)$$

where A is the oscillation amplitude, ω is the angular frequency and ϕ is the phase shift between the driven and resulting signals. The most used dynamical modes are Amplitude Modulation AFM (AM-AFM) and Frequency Modulation AFM (FM-AFM) [26, 27, 16]. In AM-AFM, the feedback mechanism maintains the oscillation amplitude constant while in FM-AFM the feedback mechanism maintains the frequency shift constant (see figure 1.4). The tip-surface interactions can be illustrated by the Lennard-Jones potential as shown in figure 1.3.

1.4.1 Amplitude modulation AFM

In AM-AFM, a sharp tip is attached at the end of a microcantilever that oscillates at or near its resonant frequency with a constant oscillation amplitude. When the tip is in

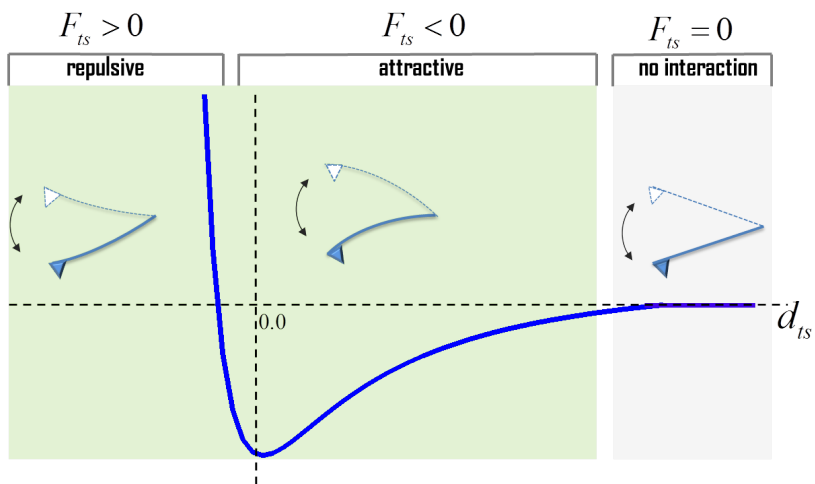


Figure 1.3: The Lennard-Jones potential illustrates the AFM operation in dynamic modes. The microcantilever is also depicted at different separation distances marked by colored regions along the black curve.

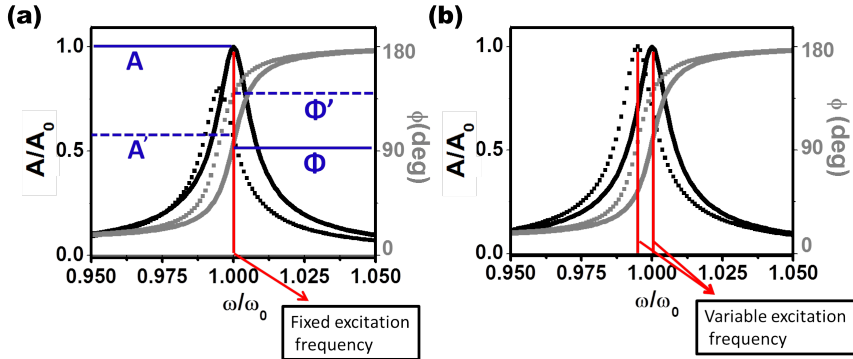


Figure 1.4: Resonance curve of a microcantilever. (a) The phase and amplitude in AM-AFM are represented for two cases: the free oscillation (full lines) and the oscillation response to an interaction force F_{ts} (dashed lines). An amplitude reduction is observed, as well as a phase shift denoted as prime('). (b) The phase and amplitude in FM-AFM are represented for two cases the free oscillation (full lines) and the oscillation response to an interaction force F_{ts} (dashed lines). A frequency shift is observed and since the operation mode is in constant amplitude, no amplitude variation is illustrated [27].

close proximity to the sample surface, the amplitude and the phase shift of the oscillation change with the strength of the interaction forces (see figure 1.4(a)). In such dynamic mode, the feedback loop keeps an amplitude value (A_{sp}) fixed while the probe is scanning the sample surface (see figure 1.5(a)). Two main observables are delivered: the amplitude A and the phase shift ϕ . The oscillation amplitude tracks the instantaneous variations in the amplitude A due to changes in the sample's topography (typically at the profile edges). The phase shift ϕ (between driven and response signals at the tip of the microcantilever) reflects changes in the dissipation of the sample and/or abrupt changes of topography. The latter are due to the non-ideal response of the electronic components in the feedback loop. The surface topography can be obtained by gathering the z_c distance to keep A_{sp} constant in every scanned pixel. An enhanced description of the theoretical aspects of this operation mode is given in Chapter 2.

1.4.2 Frequency modulation AFM

In FM-AFM, a microcantilever is driven by a sinusoidal signal at its resonant frequency. Initially, the tip is far from the sample surface and the control system captures both, the free amplitude (A_{far}) and its resonant frequency (f_{far}). By approaching the tip to the sample surface, interaction forces appear (see figure 1.4(b)). Then the resonant frequency changes (frequency shift $\Delta f_0 = f_{far} - f_{near}$) and its oscillation amplitude.

FM-AFM is divided in two sub-modes: constant excitation (CE) and constant amplitude (CA). The constant amplitude sub-mode, requires an additional gain control loop to maintain that amplitude fixed. The excitation of the sinusoidal signal is typically performed with a Phase Locked Loop (PLL). Such device is capable to demodulate the signal from the photodiode, and keep a constant phase shift between the excitation and the response signals whereby in FM-AFM the frequency shift is tracked by maintaining the phase shift value in $\pi/2$. Under such excitation scheme, a feedback loop attempts to keep the frequency shift constant while profiling the sample surface (see figure 1.5(b)). Along with the sample surface scan, two main observables are delivered: the frequency shift, tracks the instantaneous variations in the resonant frequency due to changes in the tip-sample separation, and the dissipation signal reflects changes in the mechanical properties of the sample and/or abrupt changes of topography. The surface topography can be obtained by gathering the z_c distance to keep the Δf_0 at every scanned pixel. One stated advantage of FM-AFM over AM-AFM is the system response timescales. Whereby in AM-AFM it is $t_{res} = 2Q/\omega_0$ and in FM-AFM $t_{res} = 1/\omega_0$ [16]. As a consequence, FM-AFM has shorter time response than AM-AFM in vacuum or in air. Currently, both techniques have shown its capabilities to deliver molecular and atomic resolution imaging. However, there is an on-going discussion among the AFM community to reflect meaningful information regarding the differences of both modes. Recently, it has been found that the reduction in both attractive forces (see figure 1.3) and quality factor that take place while imaging in liquid decreases the potential advantage on the feedback parameter of FM-AFM with respect to AM-AFM [28].

1.4.3 Bimodal AFM

Multifrequency AFM (MF-AFM) comprises several experimental methods that are based on the simultaneous detection of harmonics and/or eigenmodes of the microcantilever oscillation [30, 31, 32, 33, 34, 35, 36, 37]. Bimodal force microscopy is an AFM method that uses several eigenmodes frequencies for excitation and detection of the AFM observables [38, 39, 40]. The variety of observables to record the tip-surface force and operate the feedback has produced several bimodal AFM configuration modes [41]. The first of these configuration modes (Bimodal AM) is the one used along this thesis where the first two flexural eigenmodes of a microcantilever are simultaneously driven [38, 42, 43]. The output signal of the amplitude of the first eigenmode is used to image topography of the surface, or in other words as a main feedback parameter. The output signals of the second mode, namely: amplitude and phase shift are used for mapping changes in the mechanical, magnetic, or electrical properties of the surfaces (see figure 1.6).

Bimodal AFM has attracted the interest of many researchers in the force microscopy community because of its capabilities of separating topography from other interactions influencing the microcantilever motion. Hence, both resonance eigenmodes act as signal

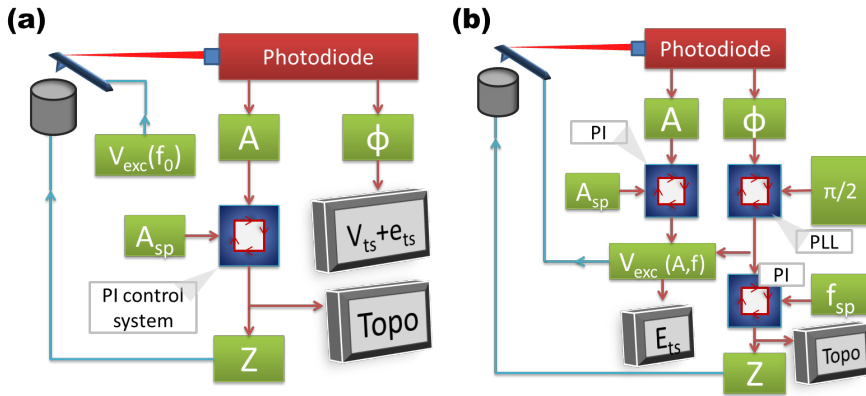


Figure 1.5: (a) Block diagram of AM-AFM showing its main components like the feedback mechanism and its observables: Amplitude (A), Phase (ϕ) and deflection (z_0). The common output images are also depicted, conservative interactions (V_{ts}), dissipative interactions (E_{ts}) and topography (**Topo**). (b) FM-AFM block diagram showing its components like the feedback mechanism and its frequency shift (f) and deflection (z_0). The common output images are also depicted, dissipative interactions (E_{ts}) and topography (**Topo**). Additional common boxes are: the driving force (V_{exc}), the phase-lock loop (PLL) and the proportional-integrative control system (PI). The schemes have been adapted from [29].

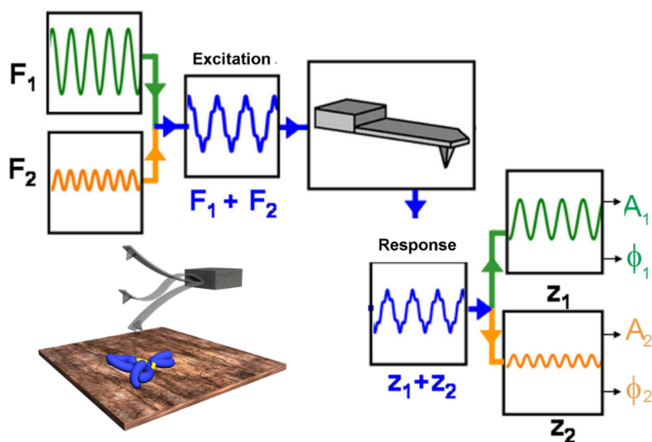


Figure 1.6: Bimodal AM scheme. The amplitude of the first mode is used for topography imaging while the signal from the second mode gives access to different mechanical or electromagnetic properties. The scheme has been adapted from [37].

channels that allow accessing and separating material properties [42, 43, 44]. In addition, bimodal AFM is compatible with air and liquid environments whereby its ability of imaging topographic and compositional contrast by applying forces below 100 pN has been verified [4, 44]. Furthermore, a recent bimodal AFM configuration (Bimodal FM) has been developed by new theoretical relationships that can be used to extract the underlying mechanical properties of materials based on several independently acquired observables [45, 46].

1.5 Concepts and conditions for high-resolution imaging

The physical and electronic limits of the instrument shall be addressed before attempting to obtain an image with high-resolution. The topography image of a sample can be directly related to a height function $h(x, y)$ whereby two types of resolutions are typically sought i.e. lateral and vertical resolutions. In what follows, to address such resolution types the term spatial resolution is used. The key factors involved in the spatial resolution imaging process of AM-AFM have been extracted from [25] (see figure 1.7).

In general, the imaging process involves an heterogeneous surface whereby the mechanical properties of the sample change and hence the resolution of the image. Under identical conditions (tip radius and applied force), the stiffer the sample the better the lateral resolution. Another key factor is the tip's radius which establishes the maximum

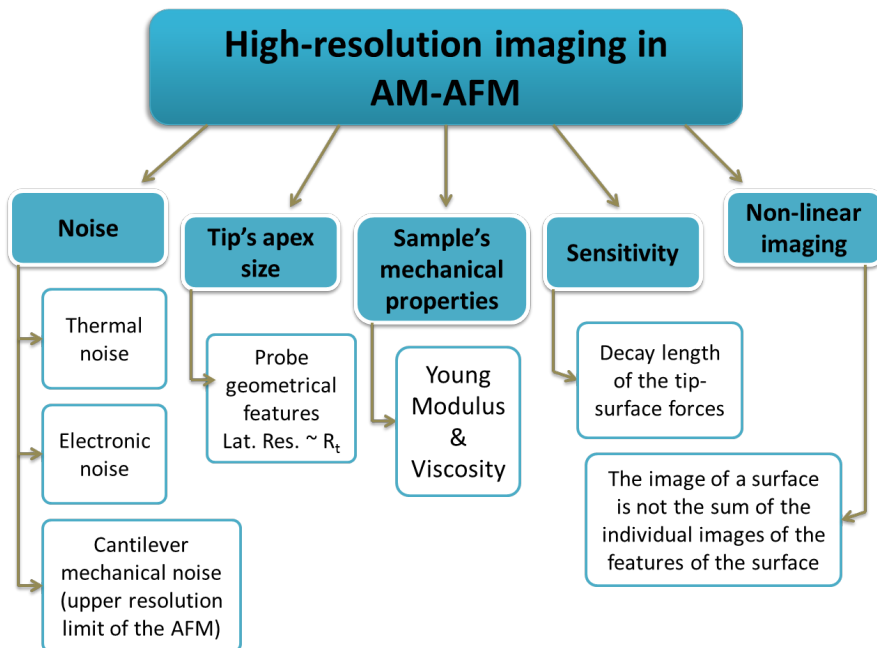


Figure 1.7: Key factors involved in the spatial resolution imaging process of AM-AFM. This summary is based on the reference book [25].

lateral resolution. The latter cannot be smaller than the size of the tip apex under mechanical contact. A more detailed explanation of the instrumental conditions for high-resolution imaging can be found in the work by Gan [47], Weihs *et al.* [48] and Schwarz *et al.* [49].

1.6 Physics of soft matter in AFM

In the framework of this thesis, the term soft matter is used for materials that distort easily in response to a external force [50]. Nonetheless, understanding this definition will be easier through an example. As depicted in figure 1.8, an elastic body with length l_0 is compressed to a final length $(l_0 - \Delta l)$ by an exerted stress σ to the upper cross sectional areas (face). Each face has an area S and hence the applied stress is given by $\sigma = F/S$. An elastic body deformation ($\delta = \Delta l$) represents the particles motion with respect to each other and is commonly characterized by the strain $\varepsilon = \Delta l/l_0$. For small deformations, a constitutive equation of a uni-axial extension has been defined as [51],

$$\sigma = E_s \varepsilon \quad (1.2)$$

where E_s is the elastic modulus or **Young modulus** of the sample. Moreover, based on a dimensional analysis of the Young modulus, $E_{s(\text{units})} = N/m^2 = J/m^3$ has to scale as the force/energy under consideration F or U and a length scale a . Analyzing this scaling law, we notice that low Young modulus values have either small force/energy scale or large length scales. Under this criteria, soft matter shall feature small interaction forces. The length scale of interest is the *nanoscale* (see figure 1.9). By considering a molecular length scale of $a_{mol} = 2$ nm and given a typical non-covalent interaction force of $F \approx 50$ pN the resulting Young modulus of the material falls in the few *MPa* range. Moreover, calculating the Young modulus for a supramolecular length, say $a_{smol} = 10$ nm and assuming the latter interaction force we obtain the hundreds of *kPa* range. One of the main characteristics of soft matter relies on its high deformation sensitivity to small forces exerted above them [50]. In concrete, the term soft matter referred in this thesis are soft polymers and biological systems within the Young moduli $10 \text{ MPa} \leq E_s \leq 500 \text{ MPa}$.

As a reference to the main part of this thesis, the typical soft matter samples measured by an AFM have been gathered and depicted with their correspondent scales and typical interactions considered in this study (see figure 1.9).

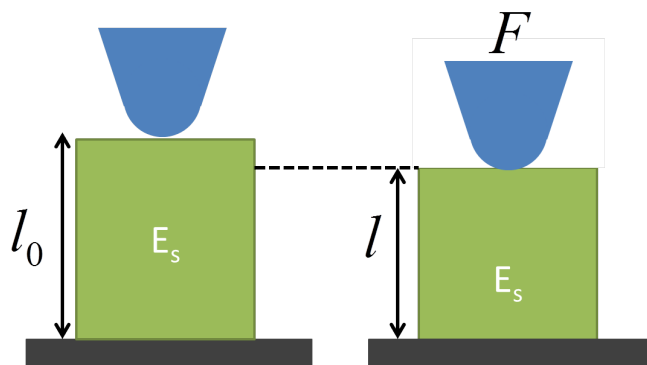


Figure 1.8: Illustrates the basic definition of stress and strain for an elastic body.

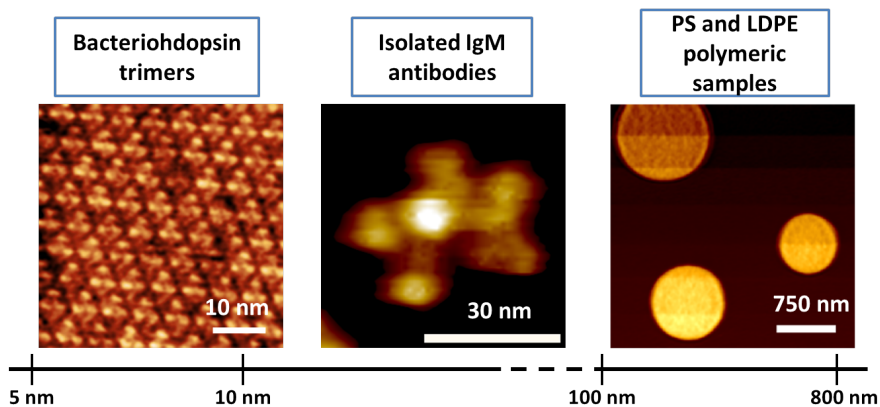


Figure 1.9: Illustrates different scales and estimated materials Young moduli involving the soft matter in dynamic AFM. The experimental images have been taken by Daniel Martin-Jimenez (unpublished results), Alma P. Perrino (unpublished results) and Elena T. Herruzo [46].

1.7 State-of-the-art of high resolution AFM images in liquid

During the last two decades, striking results in high-resolution AFM images have been obtained. Some milestones of such experimental progress are: the lattice structure of calcite (1014) cleavage plane in liquid [52], antibodies structures [53, 54, 44], molecular resolution of polymeric crystals [55], observing biomolecules of integral membranes [9, 56, 57], resolving GRoEl chaperonins in liquid [58] and recently sub-angstrom resolution has been reached to observe the 36 atoms of a pentacene molecule in UHV [59]. There is also an emergent interest of the scientific community to exploit AFM's unique ability to image and probe biological systems within its natural environments. In 2001 Ando *et al.* [60] used high-speed AFM (HS-AFM) to image structural changes of single molecules in real time (100 frames/sec) and in native conditions. Moreover, three dimensional imaging techniques have been developed to image the solid-liquid interfaces on biological systems with 10 piconewton force sensitivity, high-resolution and 40 seconds volumetric acquisition time [61]. In fact, several results indicate that to obtain molecular resolution in these kind of systems requires that the forces exerted by the tip over the surface sample should be below the forces of individual non-covalent bonds (50 – 100 pN) [4, 44, 53, 54]. towards dynamic operation modes. So far, none theoretical framework has been established to adress high-resolution imaging in dynamic AFM of soft matter as defined in section 1.6.

1.8 Motivation

The huge experimental progress on spatial resolution imaging of soft matter let us pose to the following question. Is there a theoretical framework for high-resolution imaging of soft matter in dynamic AFM?. The aim of this thesis is to propose a theoretical framework for modeling the interaction forces required to obtain high-resolution images of soft matter in dynamic AFM. Such framework proposes an a-priori estimation of the peak interaction forces through both an analytical expression and numerical calculations. The peak interaction forces have been chosen because it rapidly enables tracking the degree of invasiveness on the sample (in particular important when it is soft), its deformation and thus its resolution while imaging. To this end we focus on two important and closely related parts, the formulation of the tip-sample interaction models and the non-linear response of the tip motion. Here, the tip-sample interaction models consider both elastic and viscoelastic samples. To model elastic interactions we have used the well-known Hertzian mechanics model and the rarely used Tataro's model. The alternative Tataro's model explicitly considers that the sample is finite and thus the interaction force takes place at both tip-sample and substrate-sample interfaces. As a consequence the vertical and lateral displacements are described while the Hertzian mechanics con-

siders only a vertical deformation. In addition, to model a viscoelastic samples we have used the Kelvin-Voigt's model that describes the creep compliance of the viscous sample and also the Standard Linear Solid model that could be more suitable to describe materials that experiences both creep compliance and stress relaxation simultaneously. We have explored those models by an extensive range of numerical simulations, obtaining the proper imaging conditions of single and bimodal AFM under repulsive interactions in low- Q environment. We have also derived an expression to estimate the peak interaction forces based on Tatara's model whereby the inputs are operational parameters and sample properties. Those developments give access to experimentalists to a quantitative and qualitative understanding of the exerted forces while imaging soft matter in low- Q environments.

Chapter 2

Cantilever tip dynamics

2.1 The dynamics of the harmonic oscillator

The simple harmonic oscillator (SHO) constitutes the simplest model which describes the oscillating behaviour of a point-mass system. In terms of Newton's second law, the SHO becomes,

$$m\ddot{z}(t) = -kz(t) \quad (2.1)$$

where m is the mass of the AFM cantilever-tip assumed to be a point-mass, $z(t)$ is the tip instantaneous position and k is the cantilever tip spring constant. The solution to this linear ordinary differential equation (ODE) gives rise to,

$$z(t) = A \cos(\omega_0 t - \phi) \quad (2.2)$$

where $\omega_0 = \sqrt{k/m}$. By indicating the initial particle position and velocity, $z(0) = z_i$ and $\dot{z}(0) = v_i$ respectively. The amplitude(A) and phase(ϕ) are given by,

$$A = \sqrt{z_i^2 + (v_i/\omega_0)^2} \quad (2.3)$$

$$\phi = \tan^{-1} \left(\frac{v_i/\omega_0}{z_i} \right) \quad (2.4)$$

In terms of energy, the SHO can be written by its potential,

$$U = \frac{1}{2}kz^2 \quad (2.5)$$

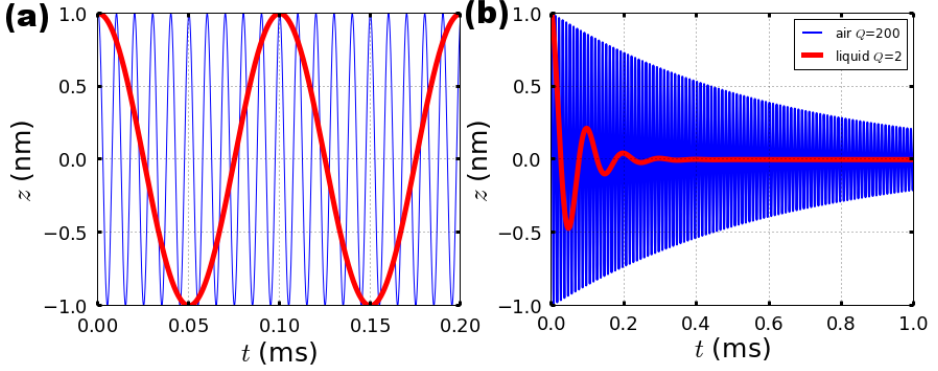


Figure 2.1: Illustrates the behaviour of a simple harmonic oscillator (a) exhibits the oscillating tip in air (blue) and in liquid (red) with $f_0=100$ kHz and $f_0=10$ kHz respectively, and damped harmonic oscillator (b) illustrating the effect of damping while operating in the air ($Q=200$) and in liquid ($Q=2$).

Hence, the conservative character of the SHO equation 2.5 is proved. Nevertheless, oscillating systems commonly experience the effect of dissipation (energy losses) like the cantilever-tip system damping,

$$\gamma = \frac{m\omega_0}{Q} \quad (2.6)$$

where Q is the quality factor of the oscillating system which describes the degree of hydrodynamic damping of the cantilever-tip system as a function of the surrounding environment (see figure 2.1(b)). The equation of motion 2.1 then takes the form,

$$m\ddot{z}(t) = -\gamma\dot{z}(t) - kz(t) \quad (2.7)$$

the solution to equation 2.7 depends on the damping coefficient and can be classified in three cases (overdamped, critically damped and underdamped) [62]. In dynamic AFM, the instantaneous tip motion mainly follows the underdamped solution,

$$z(t) = Ae^{-(\omega_0/2Q)t} \cos(\omega t + \phi) \quad (2.8)$$

where $\omega = \omega_0 \sqrt{1 - 1/(4Q^2)}$. Note the dependence of the new angular frequency value ω and hence a larger frequency shift $\Delta\omega$ for small Q values. In addition, it is worth mentioning that this modeling framework do not include the dependence of Q on the tip-sample distance as studied elsewhere [63].

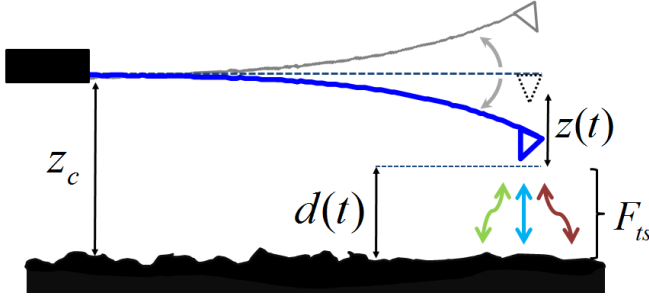


Figure 2.2: The cantilever-tip system distances as referred along the mathematical formulation whereby z_c is the equilibrium tip-sample distance without F_{ts} nor F_{exc} , then the instantaneous tip deflection $z(t)$ which is referenced on z_c and $d(t)$ the tip sample instantaneous distance ($d(t) = z(t) + z_c$).

2.2 The point-mass model in dynamic AFM

In dynamic AFM this rich dynamic behaviour of equation 2.7 is enhanced by considering two additional terms: the cantilever drive force ($F_{exc}(t) = F_0 \cos(\omega_d t)$) and the tip-surface sample interaction forces (F_{ts}). The latter gives rise to the second order non-linear differential equation [64, 16],

$$m\ddot{z}(t) = -kz(t) - \gamma\dot{z}(t) + F_{exc}(t) + F_{ts}[z_c + z(t), \dot{z}(t)] \quad (2.9)$$

where the tip-surface interactions depend on the separation distance $d(t) = z_c + z(t)$ (see figure 2.2) and velocity $\dot{d}(t) = \dot{z}(t)$ whereby forces are either of conservative ($F_c = f(d(t))$) or non-conservative ($F_{nc} = f(\dot{d}(t), \ddot{d}(t), \dots)$) nature. In liquid, as a first approximation equation 2.9 can be combined with an effective cantilever-tip mass (m_{eff}) [65]. For rectangular cantilevers, the effective mass is defined as [66],

$$m_{eff} = 0.249m + 0.144\rho_{env}(W_c L_c)^{3/2} \quad (2.10)$$

where m is the cantilever-tip mass, ρ_{env} is the environment density, L_c is the cantilever length and W_c is the cantilever width. The solution described above is valid for either a magnetic [20, 21, 22] or photothermal [23, 24] excitation schemes. Hence, in what follows these excitation methods have been considered. Equation 2.9 and Euler-Bernoulli based model have been adapted for the acoustic excitation scheme [67, 68, 69]. However, the predictive power of those approximations has not been generalized yet.

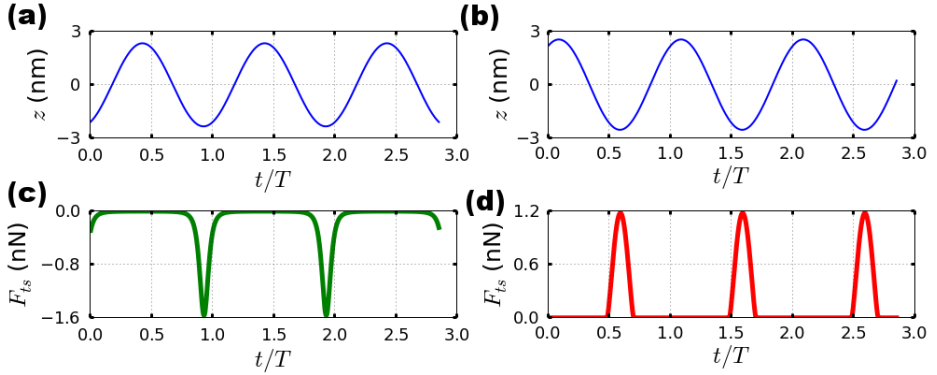


Figure 2.3: Numerical simulations of the tip dynamics. Figures (a) and (c) show the tip instantaneous deflection and instantaneous force subject to attractive van der Waals forces, with $H=3 \times 10^{-20}$ J. Figures (b) and (d) show respectively the tip instantaneous deflection and instantaneous forces subject to elastic interactions only. General simulation inputs are: $k=10$ N/m, $f_0=200$ kHz, $Q=150$, $A_0=5$ nm, $R_t=10$ nm, $A_{sp}=0.55 A_0$ and $E_s=500$ MPa.

2.2.1 Dynamic AFM non-linearities

When the tip is far away from the surface (*i.e.* $F_{ts} = 0$), the cantilever behaves as a damped harmonic oscillator with a driven force F_{exc} . As the tip is brought close to a sample surface, a nonzero tip-surface interaction takes place. Remarkably, the interaction strength is much greater at the closest tip-sample distance (or minimum oscillating position of the tip) as shown in figure 2.3. Hence, tip-surface forces are asymmetric with respect to the equilibrium distance of the cantilever (z_c). In fact, such behaviour makes the non-linear character of the dynamic AFM system from its conception.

Due to the intrinsic system non-linearities, there is no exact analytical solution to equation 2.9. However, under specific assumptions analytical and semi-analytical approaches have been provided [70, 71, 72, 73]. On the other hand, Hu [74], Kowalewski [75] and Rodriguez [76] have also derived analytical scaling laws to determine the interaction force in AM-AFM which are further explained in Chapter 5. Nonetheless, numerical simulations are well established methods to solve equation 2.9. In the framework of this thesis, the 4th-order Runge-Kutta algorithm (RK4) [77] integration method has been used. In practice, numerical simulations have driven the understanding of non-linear phenomena of the tip motion [78, 79, 80, 81]. Numerical simulations have also brought quantitative and/or qualitative meaning to several experimental results [3, 75, 82, 83].

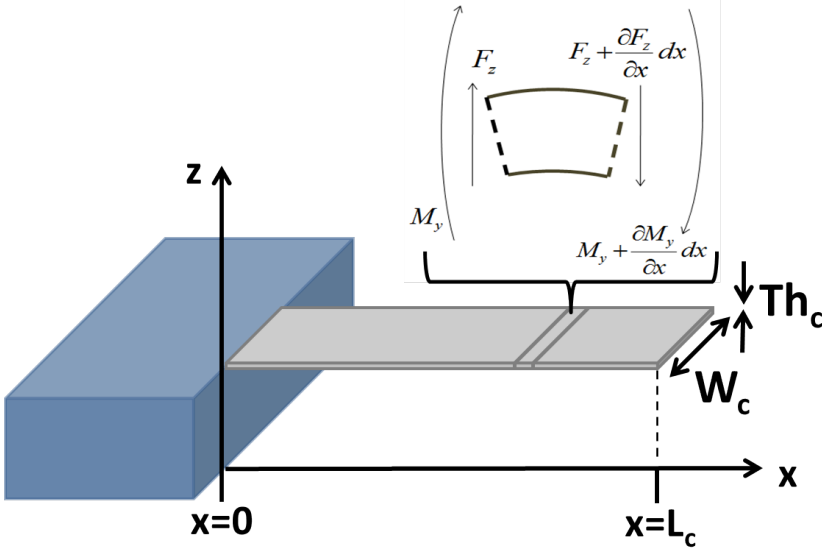


Figure 2.4: The scheme shows the cantilever beam width (W_c), length L_c and thickness Th_c used to model the cantilever tip dynamics. On the right corner an inset shows a longitudinal-section of the beam where Euler-Bernoulli's theory is applied to balance forces and moments in their respective axes.

2.3 Extended Euler-Bernoulli equation

Long time before the development of the AFM, several models to describe a one-dimensional continuum object have been proposed [51, 84, 85]. In particular, the AFM community has adopted the Euler-Bernoulli beam theory. This model describes the deflection $w(x, t)$ of a cantilever beam at position x along a cantilever beam of length L_c and constant cross-section (see figure 2.4) at time t whereby the governing equation is defined as,

$$E_c I \frac{\partial^4 w(x, t)}{\partial x^4} + \mu \frac{\partial^2 w(x, t)}{\partial t^2} = F_{sum}(x, t, w(x, t)) \quad (2.11)$$

where E_c is the Young modulus of the cantilever, I is the area moment of inertia (*i.e.* for a rectangular cantilever beam $I = 1/(12W_c Th_c^3)$), μ is the mass per unit area (*i.e.* for a rectangular cantilever $\rho_c W_c Th_c$, where ρ_c is the density of the cantilever) and the term F_{sum} includes the sum of F_{exc} , F_{ts} and F_{hydro} forces. The latter term is defined in Section 2.3.2.

A general solution of equation 2.11 describing only the vertical displacement ($Z - axis$) can be written as a linear superposition of the eigenmodes through a simple variable separation. Hence,

$$w(x, t) = \sum_{n=1}^{\infty} \varphi_n(x) Y_n(t) \quad (2.12)$$

where $Y_n(t)$ represents the n th eigenmode dynamic behaviour and $\varphi_n(x)$ are the n th eigenmode modal shapes. In addition to the rich dynamic behaviour provided by equation 2.9, the extended Euler-Bernoulli equation 2.11 provides insight into higher oscillation modes of the cantilever beam.

2.3.1 Euler-Bernoulli equation without interaction forces

In what follows, a discretization approach of x is used to solve equation 2.11 which is expressed in terms of the modal shapes $\varphi_n(x)$ in the absence of F_{sum} gives,

$$E_c I \frac{\partial^4 \varphi_n(x)}{\partial x^4} - \alpha_n^4 \varphi_n(x) = 0 \quad (2.13)$$

whith,

$$\alpha_n^4 = \frac{\omega_n^2 \rho_c W_c T h_c L_c^4}{E_c I} \quad (2.14)$$

If the cantilever beam of figure 2.4 is adopted, one can rapidly write its boundary conditions. In the case of its clamped end $x = 0$ as,

$$\varphi(0) = 0 \quad (2.15)$$

$$\varphi'(0) = 0 \quad (2.16)$$

$$(2.17)$$

and at its free end $x = L_c$ as,

$$\varphi''(L_c) = 0 \quad (2.18)$$

$$\varphi'''(L_c) = 0 \quad (2.19)$$

One final condition is needed to solve equation 2.13 which is given by the normalization condition [86],

$$\int_0^{L_c} dx \varphi_n(x) \varphi_m(x) = L_c \delta_{nm} \quad (2.20)$$

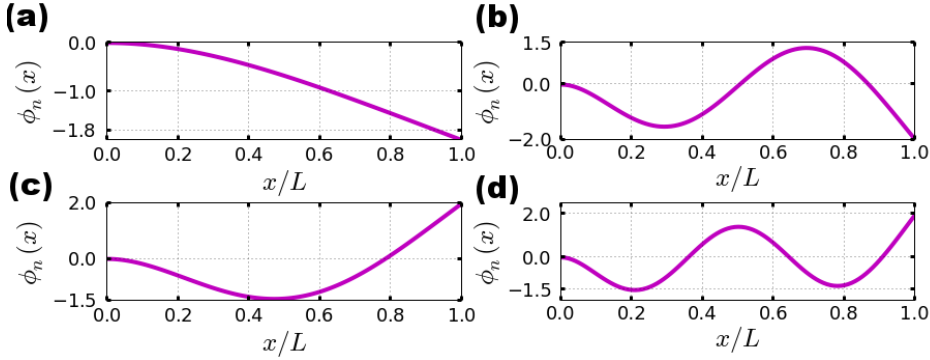


Figure 2.5: Modal shapes for the first four modes of a cantilever beam clamped at the left ($x=0$) and free at the right end. According to $\alpha_{(1,2,3,4)}=(1.875, 4.694, 7.854, 10.996)$ and hence $\omega_{(1,2,3,4)}=(1\omega_0, 6.27\omega_0, 17.55\omega_0, 34.39\omega_0)$

where δ_{nm} is Kronecker's delta. Hence, the solution for the modal shapes $\varphi_n(x)$ can be expressed as,

$$\varphi_n(x) = \cos\left(\alpha_n \frac{x}{L_c}\right) - \cosh\left(\alpha_n \frac{x}{L_c}\right) - \frac{\cos \alpha_n + \cosh \alpha_n}{\sin \alpha_n + \sinh \alpha_n} \left[\sin\left(\alpha_n \frac{x}{L_c}\right) - \sinh\left(\alpha_n \frac{x}{L_c}\right) \right] \quad (2.21)$$

with only positive real roots of α_n ,

$$1 + \cos \alpha_n \cosh \alpha_n = 0 \quad (2.22)$$

Equation 2.22 is known as the characteristic equation [86]. The values of α_n are obtained numerically for the n th eigenmode whereby for the first 4 eigenmodes $\alpha_{(1,2,3,4)}=(1.875, 4.694, 7.854, 10.996)$. Figure 2.5 shows the modal shapes obtained for those *flexural modes*.

Furthermore, based on this method the Euler-Bernoulli equation can be also solved for V-shaped cantilevers by varying its cross-sectional geometry along each δx of the cantilever length [87].

2.3.2 Equivalence to the point-mass model

The dynamics of higher eigenmodes depend on the force term F_{sum} in equation 2.11. The forces F_{exc} and F_{ts} can be described as in the case of the point-mass model (section

2.2) with the exception of F_{hydro} . The hydrodynamic damping term is crucial when considering the whole microcantilever beam immersed in a different medium than vacuum. Here, we have implemented Rayleigh's method [88] to model the internal (within the microcantilever beam) and external (microcantilever surrounding fluid) damping coefficients. Such coefficients can be written as a function of the elastic and inertial term of the Euler-Bernoulli's equation. Hence,

$$F_{hydro}(x, t) = -a_{int}E_cI \frac{\partial^4}{\partial x^4} \frac{\partial w(x, t)}{\partial t} - a_{ext}\rho_c W_c T h_c \frac{\partial w(x, t)}{\partial t} \quad (2.23)$$

where a_{int} is the internal damping coefficient of the cantilever and a_{ext} is the hydrodynamic damping of the cantilever beam due to the fluid surrounding it. Then, using equation 2.12 we can rewrite equation in a modal fashion,

$$F_{hydro}(x, t) = - [a_{int}\omega_n^2 + a_{ext}\rho_c W_c T h_c] \dot{Y}_n(t) \quad (2.24)$$

Clearly, this equation depends on the frequency of n th undertaken eigenmode. Furthermore, by separating variables on equation 2.11, multiplying it by $\varphi_m(x)$ and using the normalization condition (equation 2.20) lead us to the extended Euler-Bernoulli equation 2.25,

$$E_cI \left(\frac{\alpha_n}{L_c} \right)^4 Y_n(t) + \rho_c W_c T h_c \ddot{Y}_n(t) - F_{hydro}(x, t) = \frac{1}{L_c} \int_0^{L_c} dx [F_{exc}(x, t) + F_{ts}(x, t)] \varphi_m(x) \quad (2.25)$$

Note that equation 2.25 has some similarities to the point-mass model (2.9). However, $Y_n(t)$ is defined along the whole cantilever beam and $z_n(t)$ represent only the tip apex section. By applying the normalization condition 2.20 at the point $x = L_c$ on the $\varphi_m(x)$ results in $\varphi_n(L_c) = 2(-1)^n$ [86]. Then the instantaneous tip deflection can be defined as,

$$w(L_c, t) = \sum_{n=1}^{\infty} \varphi_n(L_c) Y_n(t) = \sum_{n=1}^{\infty} 2(-1)^n Y_n(t) \equiv \sum_{n=1}^{\infty} z_n(t) \quad (2.26)$$

by combining equation 2.26 with $m_c \equiv \rho_c W_c T h_c L_c$ and dividing it by $(L_c/4)$, the following differential equations are deduced,

$$\frac{m_c}{4} \ddot{z}_n(t) + \frac{m_c}{4} (a_{int}\omega_n^2 + a_{ext}) \dot{z}_n(t) + \left(\frac{E_cI}{L_c^3} \right) \frac{\alpha_n^4}{4} z_n(t) = F_0 \cos \omega_{exc} t + F_{t-s} \quad (2.27)$$

where,

- The n th effective mass m_n

$$m_n \equiv \frac{m_c}{4} \quad (2.28)$$

where the cantilever beam section is uniform as depicted in figure 2.4, the material is isotropic and homogeneous. For this solution the cantilever tip mass has been neglected (tipless cantilever approximation).

- The n th damping coefficient γ_n

$$\gamma_n \equiv \frac{m_c}{4} (a_{int}\omega_n^2 + a_{ext}) \quad (2.29)$$

- The n th quality factor Q_n

$$Q_n = \frac{\omega_n}{a_{int}\omega_n^2 + a_{ext}} \quad (2.30)$$

- The n th force constant k_n

$$k_n \equiv \frac{E_c I}{L_c^3} \frac{\alpha_n^4}{4} \quad (2.31)$$

where each mode fulfills the dispersion equation $k_n = m_n \omega_n^2$.

By introducing parameters 2.28, 2.29, 2.30 and 2.31 into the point mass model we reach to the n th coupled non-linear equation as,

$$m_n \ddot{z}_n(t) = -k_n z_n(t) - \gamma_n \dot{z}_n(t) + F_{exc}(t) + F_{ts}[z_c + z(t), \dot{z}(t)] \quad (2.32)$$

Similar approaches to find the equivalent point-mass models have been proposed [89, 42], such as Melcher *et al.* that is based on the energy balance principle. On the other hand, the damping term F_{hydro} can be determined by alternative heuristic models [90]. It is worth noting that in liquid the damping term introduced to the whole cantilever beam cannot be neglected because it affects the oscillating system and hence the calculation of the unknown force F_{ts} .

2.4 Introduction to tip-surface interaction forces F_{ts}

The tip-sample interaction force term F_{ts} comprises a sum of different interaction forces. In dynamic AFM operation modes these forces can be separated in two types of interaction regimes: attractive ($\langle F_{ts} \rangle < 0$) and repulsive ($\langle F_{ts} \rangle > 0$) as depicted in figure

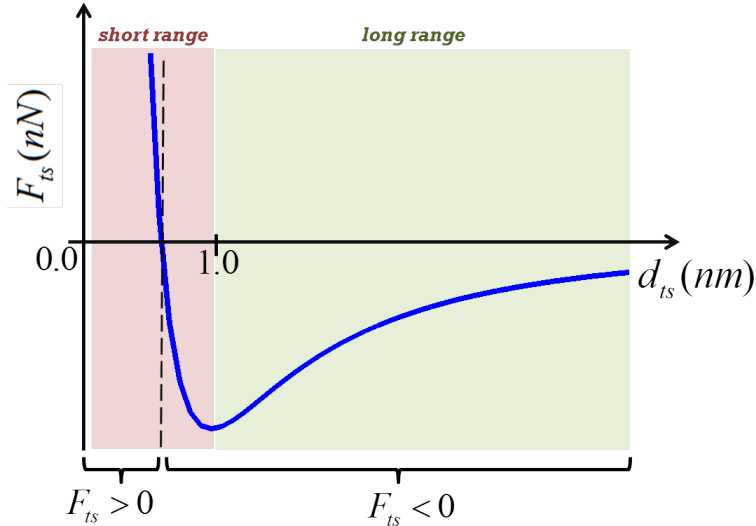


Figure 2.6: Lennard-Jones potential depicting the interaction regimes in dynamic AFM for attractive and repulsive forces, short and long ranges forces classification.

2.6. In regard to the separation distance d_{ts} range, forces are classified into short range forces (SRF: 0.1 nm, 1 nm) and long range forces (LRF: 1 nm, 100 nm). The first ones are: contact mechanics [91, 92, 93, 94, 95], chemical bonds [27, 11], adhesion [96, 97] and viscoelastic [97, 98, 99]. On the other hand, long range forces comprise: electrostatic [100, 101, 102], double layer forces [96, 97], magnetic [103, 104, 105] and van der Waals interactions [106, 107, 108].

In the framework of soft matter interactions in liquid, the following force models have been considered: Hertzian mechanics, van der Waals, electrical double layer forces, Kelvin-Voigt's viscoelasticity, Maxwell's viscoelasticity, the standard linear solid (SLS) and the Tatara contact mechanics.

2.4.1 Hertzian mechanics

In 1881 H. Hertz [94] first solved the problem of pressure distribution between two elastic bodies coming into mechanical contact (see figure 2.8). The assumptions taken by Hertz can be summarized as follows:

- The contacting bodies are solids made of an isotropic and homogeneous material in the liner elastic regime.

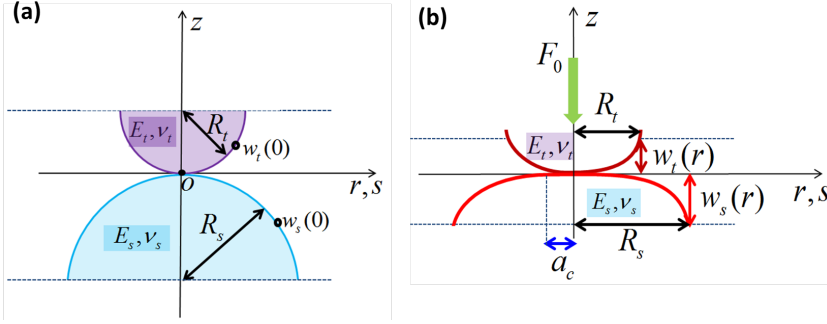


Figure 2.7: (a) Before deformation two elastic spheres touch at point 0 and two adjacent points can be defined as $w_t(0)$ and $w_s(0)$. (b) Applying a concentrated force F_0 , the spheres are brought into mechanical compression whereby the relative penetrations are defined by $w_t(r)$ and $w_s(r)$.

- The size of the contact radius a_c is very small in comparison to the radii of curvature of the undeformed body *i.e.* in AFM $a_c \ll R_t$.
- Each sphere can be considered as an elastic *half-space*, in the case of AFM this applies only to the surface sample.
- Only a normal stress is present in the contact interface whereby no friction takes place.

Boussineq's solution to a perpendicular force concentrated at point $r = 0$ (F_0) of a *half-space* determines a vertical displacement of the surface $w(r)$ which can be expressed as [109],

$$w(r) = \frac{F_0(1 - \nu^2)}{\pi E r} \quad (2.33)$$

where E and ν denote the Young's modulus and Poisson's ratio of the *half-space* respectively, and r is the radial distance from the point where the concentrated force is applied. Based on this solution Hertz proposed the surface displacement of two contacting spheres as,

$$w_i(r) = \frac{(1 - \nu_i^2)}{\pi E_i} \int_0^{a_c} P(s) s ds \int_0^{2\pi} (r^2 + s^2 - 2rs \cos \theta)^{-1/2} d\theta \quad (2.34)$$

where P is the pressure acting over a contact area, s and θ are coordinates parameters defined in figure 2.8. On the other hand, by assuming that the profiles of the spheres are parabolic ($r^2/(2R)$). Hence,

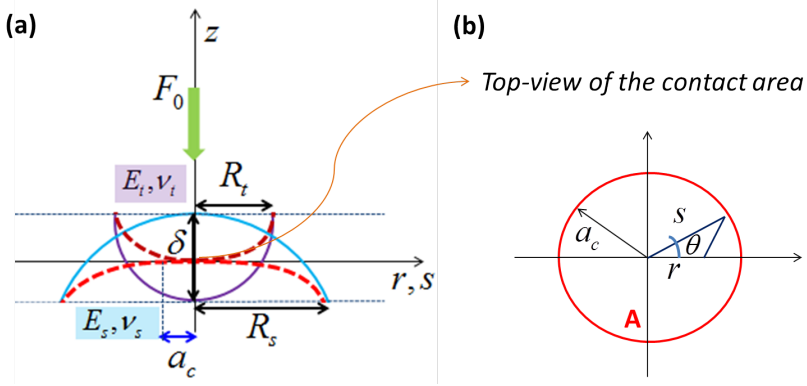


Figure 2.8: (a) Two elastic spheres are brought into mechanical contact by a concentrated force F_0 , resulting in a contact area with radius a_c , relative penetration of each sphere $w(r)$ and the deformation δ . (b) Integration scheme for calculating the force distribution over the contact area as a function of θ and s .

$$w_1 + w_2 = \delta - \frac{r^2}{2R^*}, \quad (r < a_c) \quad (2.35)$$

where $R^* = 1/(1/R_1 + 1/R_2)$ is the reduced radius of the sphere and δ denotes the relative approach of distant points among these two spheres (see figure 2.8). Substituting equation 2.34 into equation 2.35 such that,

$$\frac{1}{\pi E^*} \int_0^{a_c} P(s) s ds \int_0^{2\pi} (r^2 + s^2 - 2rs \cos \theta)^{-1/2} d\theta = \delta - \frac{r^2}{2R^*} \quad (2.36)$$

where the combined or reduced Young modulus of both spheres is $E^* = 1/((1 - \nu_1^2)/E_1 + (1 - \nu_2^2)/E_2)$. By assuming an elliptical distribution of pressures and no lateral displacement of the elastic bodies, Hertz proposed the solution to equation 2.36 as,

$$P(r) = \frac{2a_c E^*}{\pi R^*} \left(1 - \frac{r^2}{a_c^2}\right)^{1/2}, \quad (r < a_c) \quad (2.37)$$

where the penetration $\delta = a_c^2/R^*$. Furthermore, integrating the term $P(r)$ over the contact area A_c yields to the Hertzian force [92]

$$F = \frac{4E^* a_c^3}{3R^*} = \frac{4E^* \sqrt{R_t} \delta^{3/2}}{3} \quad (2.38)$$

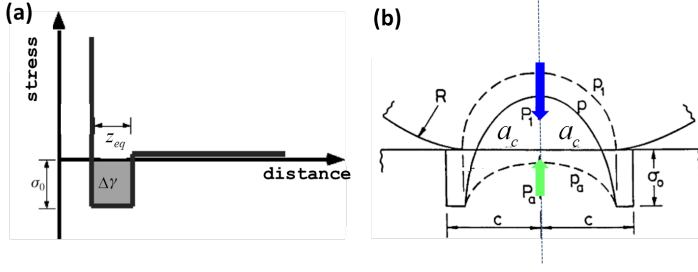


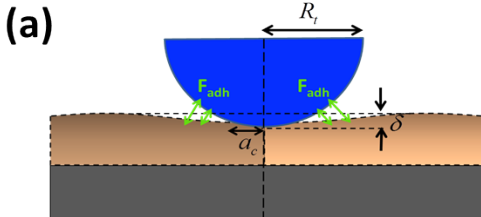
Figure 2.9: (a) Force-distance law according to the Dugdale potential [111]. (b) Scheme of the Maugis-Dugdale distribution of surface traction comprises two terms: hertzian pressure p_1 acting on the contact area (delimited by the radius a_c) and the adhesive tension p_a acting on the cohesive radius c . Figures (a) and (b) have been adapted from [112] and [113], respectively.

where $R^* \rightarrow R_t$. Hertzian mechanics have proven a good description in the macroscopic scale although the intermolecular adhesion between two solid surfaces has not been considered. After Hertz's pioneering work, Johnson, Kendal and Rayleigh (JKR) [91], and Derjaguin, Mueller and Taborov (DMT) [93] introduced adhesion forces to the hertzian force term 2.38 as summarized in figure 2.10. However, DMT and JKR models predicted different values of the adhesive force. In 1976, Tabor [110] introduced the Tabor number (μ_T) which reproduces both JKR and DMT models. This number is given by,

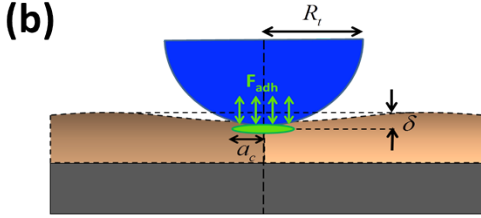
$$\mu_T \equiv \left(\frac{R_t (\Delta\gamma^s)^2}{E^{*2} z_{eq}^3} \right)^{1/3} \quad (2.39)$$

where z_{eq} is the equilibrium interfacial separation of the atomic planes the force term is zero and $\Delta\gamma^s$ is the work of adhesion given by $\Delta\gamma^s = \gamma_t^s + \gamma_s^s - \gamma_{ts}^s$. Tabor pointed out that JKR theory applies for high μ_T values ($\mu_T \gg 1$) while DMT model held for smaller ones μ_T ($\mu_T \ll 1$). In other words, JKR model is convenient for highly adhesive and soft materials while DMT applies to low adhesive and rigid materials. For the intermediate range between JKR and DMT models, an analytical solution was obtained by Maugis [114].

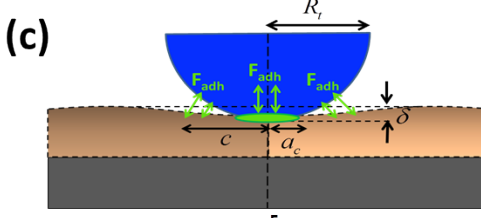
Maugis based his solution on the Dugdale's model[111] (see figure 2.9(a)) to find the applied force in terms of a cohesive parameter c as depicted and expressed in figures 2.9(b) and 2.10(c). The range of application of the different contact mechanics models is illustrated in figure 2.11. Nonetheless, these analytical framework relies on several assumptions, namely: the deformations are small ($a_c \ll R_t$), no viscosity is considered and the material belongs to the linear elastic behaviour, no lateral deformations are induced and the contact geometry is axisymmetric. In this context, continuum mechan-

(a) 

$$F_{DMT} = \frac{4}{3} E^* \sqrt{R_t} \delta^{3/2} - 4\pi\gamma^s R_t$$

(b) 

$$F_{JKR} = \frac{4}{3} E^* \sqrt{R_t} \delta^{3/2} - \sqrt{8\pi\Delta\gamma^s E^* a_c^3}$$

(c) 

$$F_{MD} = \frac{4}{3} E^* \sqrt{R_t} \delta^{3/2} - 2\sigma_{th} a_c \left[a_c \sqrt{c^2 - a_c^2} + c^2 \sec^{-1}(c/a_c) \right]$$

Figure 2.10: (a) Scheme and equation of the DMT model that comprises the Hertzian term plus a maximum adhesion force given by $F_{adh} = -4\pi\gamma^s R_t$, (b) scheme and equation of the JKR model that comprises the Hertzian term plus a maximum adhesion force given by $F_{adh} = -3\pi\gamma^s R_t$ and (c) scheme and equation of the M-D model that comprises the Hertzian term plus the adhesion force given by $F_{adh} \in [-3\pi\gamma^s R_t, -4\pi\gamma^s R_t]$. Where γ^s is defined as the surface energy, R_t the AFM tip radius, a_c is the contact radius, c is the outer radius of the cohesive region and σ_{th} is the Dugdale potential energy.

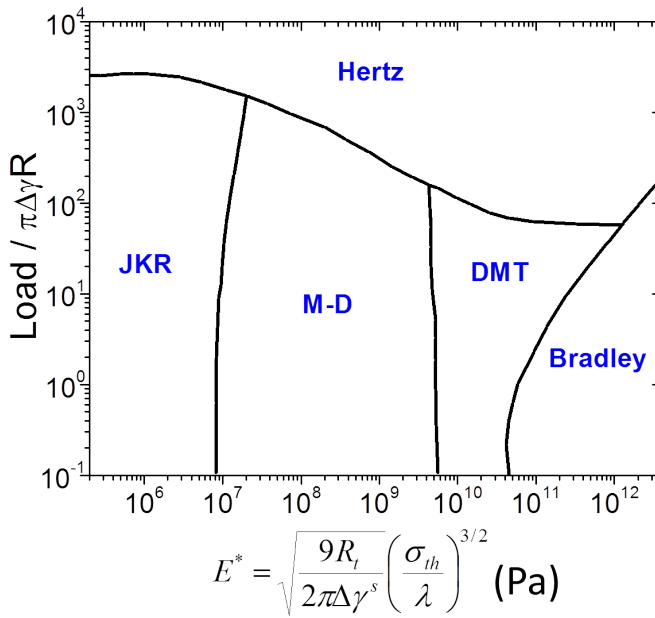


Figure 2.11: Johnson and Greenwood continuum mechanics map as a function of the reduced Young moduli E^* . The curves corresponding parameters are: $R_t = 5$ nm, $\gamma^s = 2$ mJ/m² and $\sigma_{th} = 2\gamma^s/z_{eq}$. Adapted from [119].

ics framework has provided good descriptions of experimental results at the nanoscale [115, 116, 117]. Nonetheless, their application could present some restrictions as explored through atomistic simulations [118].

In liquids, the aforementioned adhesion forces are generally screened [106, 120] and hence the interaction forces sensed at the tip are determined by the electrical double layer force, viscoelastic and solvation forces. Nevertheless, under high-resolution imaging conditions the latter forces are commonly neglected [61, 81, 121].

2.4.2 Electrostatic interactions (DLVO)

Molecular interactions are typically the subject of study while interpreting AFM data. In this section, the theory that comprises the electrostatic interactions between tip and sample is described. The study of colloidal stability proposed by Derjaguin-Landau-

Verwey-Overbeek (DLVO) force model [106, 122]. Such model assumes that the interaction forces can be approximated by a superposition of van der Waals attractive forces and electrical double-layer repulsive contributions.

2.4.2.1 van der Waals forces

van der Waals forces reflect various interactions, such as interactions between ions and dipoles with polarized molecules. Typically, they include contributions from fixed dipoles (*Keesom forces* [123]), dispersive interactions (*London forces* [123]) and dipole-induced interactions (*Debye forces* [123]). The force term for a sphere to *half-space* interaction is given by,

$$F_{vdW} = -\frac{HR_t}{6d^2} \quad (2.40)$$

where H is the Hamaker constant [124], R_t the tip radius and d is the tip-surface distance. Note that when $d < 0$, d is assumed to be the intermolecular distance $a_0 = 0.165$ nm [16].

2.4.2.2 Electrical double layer forces

The electrical double layer force originates from the overlap of the counterions distributions near each surface. The surface potential is related to the surface charge density (χ_t and χ_s), the temperature (T) and the co-ions/counterions valency (according to the Grahame equation [106]). For low potentials (i.e. $\lesssim 25$ mV), the counterions are modeled by a simple exponential decay in relation to the tip-surface separation d . This forces can be calculated such that,

$$F_{edl} = \frac{4\pi R}{\epsilon\epsilon_0} \chi_t \chi_s \lambda_D e^{-d/\lambda_D} \quad (2.41)$$

where χ_t , χ_s , ϵ , ϵ_0 and λ_D , are respectively, the surface charge density of the tip, the surface charge density of the sample, relative dielectric constant of the medium, dielectric constant of the medium and the Debye length. The latter has been defined by Debye-Hückel as,

$$\lambda_D = \left(\frac{\epsilon\epsilon_0 k_B T}{\sum_i \rho_i e^2 \vartheta_i^2} \right) \quad (2.42)$$

where ρ_i is the density of the electrolyte i in the bulk solution, ϑ_i its valency and e is the electron charge. Whereby for monovalent ions in aqueous solution at 25 °C the Debye length is given by $\approx 0.304/\sqrt{C_i}$ with C_i the concentration of ions [125].

2.4.3 Viscoelastic forces

As mentioned before, the force term F_{ts} reflects both the conservative and non conservative interactions underneath the tip-sample ensemble. In fact, most of materials in their *real-environments* manifest time-dependent phenomena. Based on Hooke's law, O. Meyer[126] proposed the constitutive equation of a viscoelastic material, which is given by,

$$\sigma = E\varepsilon + \eta\dot{\varepsilon} \quad (2.43)$$

where E is the Young modulus of the material, η its viscous coefficient, ε is the strain and σ the stress applied to the viscoelastic material. The first term of equation 2.43 has been described in section 1.6 while its second term is the viscous force [16],

$$F_{vis} = -\eta a_c \dot{\delta} \quad (2.44)$$

where $a_c = \sqrt{R_t \delta}$ is the contact radius of hertzian mechanics. The viscous force has a linear dependency on the deformation rate ($\dot{\delta}$) which follows $\dot{\delta}(t) = -\dot{z}(t)$. Such simple viscoelastic models have been used to describe materials creep and stress relaxation [126, 127]. By using viscoelastic circuit diagrams, three viscoelastic models are described in the following sections.

2.4.3.1 Creep

Creep is the tendency of a viscoelastic material to move slowly like the retarded elastic response depicted in figure 2.12 under the influence of a known stress σ_0 . This behaviour has been modeled through equation 2.43 as,

$$\varepsilon(t) = \sigma_0/E \left(1 - e^{-t/\tau}\right) \quad (2.45)$$

where τ is the restitution/relaxation time given by $\tau = \eta/E$ and t is the observation time (time of measurement). Kelvin-Voigt's model considers that the final strain in both the spring and the dashpot are the same and the total stress is the sum of both contributions (using Boltzmann superposition principle).

2.4.3.2 Stress relaxation

Stress relaxation describes how a viscoelastic material relieves stress under a prescribed applied strain. The Maxwell model can be used to predict this behaviour. This model relates the strain and stress rates of an elastic spring in series with a viscous dashpot as,

$$\dot{\varepsilon} = \frac{\sigma}{\eta} + \frac{1}{E}\dot{\sigma} \quad (2.46)$$

for a constant value of ε , equation 2.46 becomes,

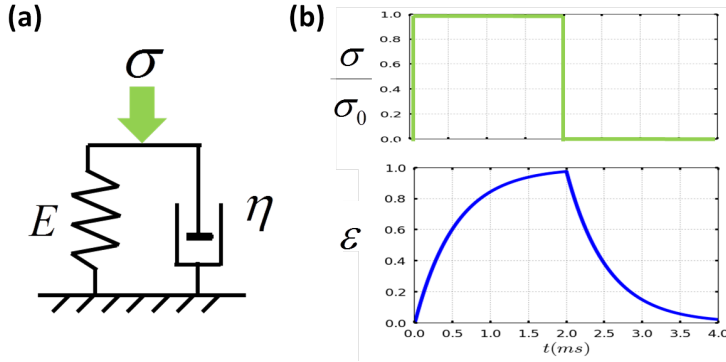


Figure 2.12: (a) Kelvin-Voigt circuit diagram, (b) creep relaxation in response to a constant applied stress σ .

$$\sigma = \sigma_0 e^{-t/\tau} \quad (2.47)$$

where σ_0 is the maximum stress in response to an applied strain, τ is the relaxation time given by $\tau = \eta/E$ and t is the observation time (time of measurement). Maxwell's model considers that stress is unique and the total strain comprises both the spring and the dashpot (as illustrated in figure 2.13). This model has been compared to stress relaxation experiments in polymers whereby qualitative trends have been verified [126].

2.4.4 Interaction forces between tip and soft samples

One aim of this thesis is to identify the interaction forces comprised by $F_{t,s}$ that properly describe soft-matter. To this end, two models are studied. The first addresses the effect of the viscosity to the interaction force while the second focuses on the elastic behaviour of a finite sample.

2.4.4.1 Standard linear solid model

The standard linear solid (SLS) viscoelastic model describes the sample material with three elements as depicted in figure 2.14. It presents two mechanically equivalent forms, one based on Kelvin-Voigt's and the second one on Maxwell's model. Here, the governing equation of Kelvin-Voigt's variant is presented,

$$\dot{\varepsilon} = \frac{\dot{\sigma}}{E_0} + \frac{\sigma - E_\infty(\varepsilon - \sigma/E_0)}{\eta_\infty} \quad (2.48)$$

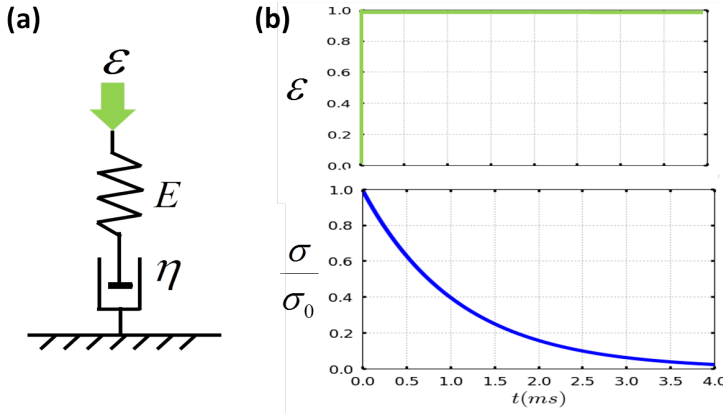


Figure 2.13: (a) Maxwell circuit diagram, (b) stress relaxation in response to a instantaneous applied strain ϵ .

where E_0 is the sample instantaneous modulus, E_∞ is the infinite modulus and η_∞ is the viscous coefficient of the material. In this context, it is worth noting that E_0 represents the elastic modulus of the material at very fast loading rates and hence E_∞ is the elastic modulus of the material at slower loading rates (>1 order of magnitude). Furthermore, by reordering terms in equation 2.48 and multiplying the resulting viscous stress by the contact radius (a_c) we derived,

$$F_{sls} = \frac{E_0}{E_0 + E_\infty} \eta_\infty \left(a_c \dot{\delta} - \frac{\dot{F}}{E_0} \right) \quad (2.49)$$

where $a_c = \sqrt{R_t \delta}$ is the contact radius obtained by Hertz and \dot{F} is the first derivative of the applied force in function of time. The creep compliance of a linear viscoelastic solid $J(t)$ can be represented by the time-dependent modulus variation $J \sim 1/E$ as illustrated in figure 2.14(b) and is governed by,

$$J(t) = \frac{1 - \nu^2}{E_\infty} \left(1 - (1 - E_\infty/E_0) e^{-t/\tau} \right) \quad (2.50)$$

where t represents the time-scale and τ_{sls} is the characteristic time of the material found in the transition between the rubbery and glassy phases ($\tau_{sls} = \frac{E_0 - E_\infty}{E_\infty E_0} \eta_\infty$). This transition regime is also known as viscoelastic regime. By looking at Figure 2.14(b), the idea behind this model can be visualized. First, the sample instantaneous modulus (E_0) respond to an abrupt load (F_0) whereby if the interaction remains present; a second spring (E_∞) starts sharing this load throughout the retarded loading stage time τ_{sls} (as depicted in figure 2.14(a)). At $t \gg \tau_{sls}$ the SLS system overpasses the viscoelastic

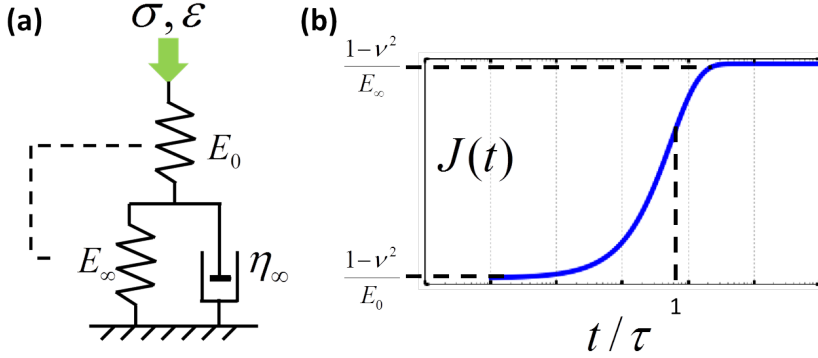


Figure 2.14: (a) SLS circuit diagram, (b) creep relaxation and stress relaxation in response to both stress σ and strain ϵ .

regime of interaction and the material's Young modulus is given by the resulting Young modulus $E_{sls} = E_0 E_\infty / (E_0 + E_\infty)$ where generally $E_0 \gg E_\infty$ and hence $E_{sls} \approx E_\infty$ (as depicted in figure 2.14(b)). After the loading stage time the surface is released and hence it relaxes to the equilibrium position (position at time $t = 0$ when the loading stage begins) over the restitution/relaxation time τ_{sls} . It is important to note that the standard linear solid model does not consider the concept of material load/unload history or memory to the elastic properties of the material by means of E_0 and E_∞ while describing simultaneously the stress relaxation and the creep compliance of a viscoelastic sample [126, 128, 98]. Such viscoelastic behaviours have been reported experimentally for soft polymeric and biological samples [128, 129, 130, 131, 99].

2.4.4.2 The Tatara model

In 1989, Tatara proposed a model to describe both vertical and lateral displacements during a soft body compression [95]. This soft body fulfills the incompressibility criteria of Boussinesq and hence the same theoretical framework can be used. Thus, Hertz integral equation 2.34 becomes,

$$w_i(z, r) = \frac{(1 - \nu_i^2)}{\pi E_i} \int \int P(s) ds d\theta \quad (2.51)$$

and its lateral displacement $U_s(z, r)$ for the linear case of E_s is such that,

$$U_s(z, r) = \frac{(1 - 2\nu_s)(1 + \nu_s)}{2\pi E_s} \int \int P(s) s ds d\theta \quad (2.52)$$

where the subscript s of E_s and ν_s denotes the mechanical properties of the sample. On the other hand, the variables presented in equation 2.51 are analogous to Hertz's case. Note that $w_i(z, r)$ and $U_s(z, r)$ are functions of two coordinates, z is the vertical variable displacement and r the radial within a cylindrical system of reference. Based on Timoshenko and Goodier method [84] the vertical displacement due to an applied load F is given by,

$$w_i(z, r) = \frac{F}{\pi E_i} \left(\frac{(1 + \nu_i)z^2}{(r^2 + z^2)^{3/2}} + \frac{2(1 - \nu_i^2)}{(r^2 + z^2)^{1/2}} \right) \quad (2.53)$$

where E_i and ν_i denote the Young moduli and the Poisson ratio respectively. Timoshenko and Goodier theory implies that the vertical displacement for $w_i(0, r)$ replicates Boussineq equation *i.e.* $w_i(0, r) = (1 - \nu^2)/(\pi Er)$ 2.33. On the other hand, the integration of the total lateral displacement becomes,

$$U_s(z, r) = \int \int \frac{P(s)s}{2\pi E_s} \left(\frac{(1 - \nu_s)(2R_s)^2}{(s^2 + 4R_s^2)^{3/2}} + \frac{2(1 - \nu_s)}{(s^2 + 4R_s^2)^{1/2}} \right) dsd\theta \quad (2.54)$$

In the above equation, $P(s)$ is the pressure distribution along s , E_s is the sample Young modulus, ν_s is the Poisson's ratio of the sample, R_s is the sample Radius, s and θ are the coordinates of the area of contact as shown in figure 2.8. However, the exact solution to this equation yields to another integral equation which makes it very difficult to tackle. Therefore, Tatara defined two asymptotic cases of $w_i(z, r)$. Case I is defined by substituting $z = 2R_i$ and $r = 0$ into equation 2.53 yielding,

$$w_i(2R_i, 0) = \frac{(1 + \nu_i)(3 - 2\nu_i)}{4\pi E_i R_i} F \quad (2.55)$$

On the other hand, case II is defined by substituting $z = 2R_i$ and $r = a_c$ into equation 2.53. Hence,

$$w_i(2R_i, a_c) = \frac{F}{2\pi E_i} \left(\frac{(1 + \nu_i)4R^2}{(a_c^2 + 4R^2)^{3/2}} + \frac{2(1 + \nu_i^2)4R^2}{(a_c^2 + 4R^2)^{1/2}} \right) \quad (2.56)$$

whit the series expansion of a_c applied to the denominators of both terms, equation 2.56 is rewritten as follows,

$$w_i(2R_i, a_c) = F a_c^2 \frac{L_i}{2R_i} - F K_i \quad (2.57)$$

where $L_i = (1 + \nu_i)(5 - 2\nu_i)/(8\pi E_i R_i)$ and $K_i = (1 + \nu_i)(3 - 2\nu_i)/(4\pi E_i R_i)$, R_i comprises both the tip and sample radius and F is the applied normal force as illustrated in figure 2.15(b). It is worth noting that Case II reflects the difference of an approximated lateral displacement at $w_i(2R_i, a_c)$ and the reference point (case I). Inserting this result

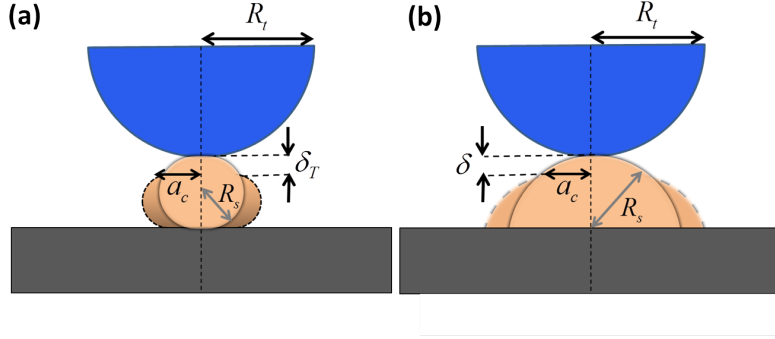


Figure 2.15: (a) Illustrates the Tataro contact mechanics when a force is applied to a finite sample but experiences a two contact deformation (tip-samples and sample-substrate). (b) Illustrates the force for a one point of contact *i.e.* a sample is considered as a half-space ($R_s > R_t$).

to the hertzian deformation results into the total indentation due to vertical and lateral displacements of the sample,

$$\delta_T = F^{2/3}/n^{2/3} - Fa_c^2 \frac{L_i}{2R_i} + FK_i \quad (2.58)$$

where $n = (4/3)E^* \sqrt{R^*}$. The total indentation of equation 2.58 reflects the first half of the sample as depicted in figure 2.15(b). However, it is assumed that the study is not focused on a half space sample but on a finite sample based on the method of Johnson for cylindrical bodies (page 129-134) [92] combined with a series expansion applied to equation 2.58. The exerted force can be written as the sum of power laws, given by,

$$F_{Tataro} = \frac{n}{2^{3/2}} \delta_T^{3/2} + \frac{3n^2}{8n_c} \delta_T^2 + \frac{15n^3}{2^{11/2}n_c^2} \delta_T^{5/2} \quad (2.59)$$

where,

$$\frac{1}{E_{eff}} = \frac{1 - \nu_t^2}{E_t} + \frac{1 - \nu_s^2}{E_s} \quad (2.60)$$

$$n = \frac{4}{3} \sqrt{R_{eff} E_{eff}} \quad (2.61)$$

$$n_c = \frac{4\pi E_t R_t E_s R_s}{6 + \nu_t - 2\nu_t^2 + \nu_s - 2\nu_s^2} \quad (2.62)$$

$$\frac{1}{R_{eff}} = \frac{1}{R_t} + \frac{1}{R_s} \quad (2.63)$$

The subindexes t and s stand, respectively, for tip and sample. In the above equations, δ is the indentation, ν_t and ν_s the Poisson coefficients and E the Young modulus. Figure 2.15(a) depicts the tip-finite sample ensemble. The forces mentioned above could be applied to a general type of surface or a specific one. So far, a wide spread assumption is to model those forces with a surface sample characterized by a *half-space*. However, we put into consideration new alternative models devoted to soft materials with emphasis on their elastic (Tatara's model) and viscoelastic behavior (the standard linear solid model).

2.5 Force microscopy simulator: dForce

The modeling framework introduced along this chapter describes the elements required to interpret a wide diversity of tip-sample situations while operating the force microscope in amplitude modulation (Single and Multi-frequency). Another key element is the computer code that allow us solving the equations described in Sections 2.2 and 2.3 through numerical integration methods [132, 133]. On top of such numerical integration kernel we have developed a new simulations code that enhances the modularization of the cantilever tip dynamics and the tip-surface interaction models. This new computer simulation framework (dForce) relies on the dynamically typed, interpreted, versatile and open source programming language Python [134]. Python offers the flexibility of an interpreted language combined with a complete suite of compiled scientific libraries (Numpy/Scipy). Numpy is based on compiled numerical simulations libraries from Fortran, C and C++ [135, 136]. Those features make Python a very efficient programming language (from the developer point of view) [137] and also numerically efficient as it has been previously compared [138, 139]. On the other hand, Scipy is a well-established computer scientist community that uses python to develop new tools in the fields of numerical simulations, scientific analysis, visualization and recently scientific reproducibility [135]. Furthermore, Python is well documented, easy to learn and hence it allows new students to maintain and contribute quickly to the simulation framework [140].

dForce is a simulations framework that creates an interactive [141] software platform (see figure 2.16) devoted to the visualization [142], analysis and data storage of dynamic AFM simulations. Since 2010, dForce has experienced over 237 versions. The current version allows the single and/or multifrequency simulations, choosing over 10 interaction force models and visualizing time, position and frequency domains. Furthermore software development description, some selected features and outlook of the simulator have been gathered in Appendix A.

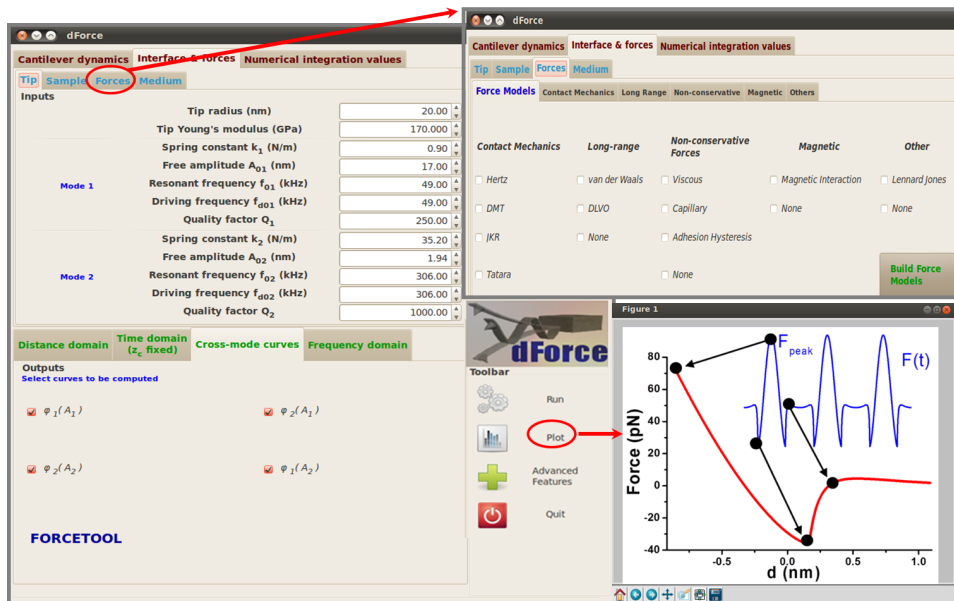


Figure 2.16: dForce creates an interactive virtual environment for the different types of force microscope situations. This code breaks up the tip-surface ensemble into easy recognizable sub-systems such as the cantilever model, medium properties, tip and sample features, and interaction forces.

Chapter 3

Unmasking time-dependent viscoelastic forces

3.1 Introduction to time-dependent viscoelastic forces

Most polymeric and biological materials measured with dynamic AFM techniques include a viscoelastic behaviour [97, 143, 144, 99]. One question that frequently arises is the proper representation of energy dissipation in AM-AFM. Tamayo and Garcia found a relationship for the phase shift ϕ given by the instrument to the dissipated energy per oscillation cycle by means of a sinusoidal magnitude [145]. Moreover, Garcia and co-workers have also separated such dissipated energy into adhesion hysteresis and viscoelastic contributions [97]. Furthermore, Proksch and Yablon have calculated the loss tangent of the imaged sample which provides qualitative compositional information of it by means of two experimental observables phase shifts and oscillation amplitudes [146, 130]. Recently, Raman and Cartagena have experimentally verified that viscoelastic properties of cells can be measured at oscillation frequencies of ~ 10 kHz with AM-AFM [129, 131]. In general, these articles underscore the importance of including viscoelasticity to the overall mechanical response of the oscillating tip in interaction with a soft sample.

Throughout this chapter, we propose a method to estimate the peak forces exerted over a viscoelastic material by knowing the oscillation amplitude, phase shift, driven frequency and the contact time between tip and sample. This method considers a sinusoidal piecewise material response to the driven oscillating tip in AM-AFM during the contact time within an oscillation cycle. The material response for a permanent sinusoidal contact of the instrument and material has been previously studied and it has a close dependence on both the deformation δ (conservative forces) and the deformation rate $\dot{\delta}$ (dissipative forces) of the sample [126, 147, 127]. Likewise, the sinusoidal piecewise material re-

sponse described in this chapter follows such dependence (δ and $\dot{\delta}$). In AFM, the deformation rate and the tip's velocity build a relationship between the mechanical response of the sample (material response) and the instrumental AFM parameters whereby the oscillation amplitude, driven frequency, contact time and phase shift are considered. For a prescribed maximum deformation (permanent maximum deformation) and a contact time of the order of the relaxation time of the sample we estimate the peak viscoelastic forces in the time-domain. Numerical simulations of AM-AFM allowed us to disentangle the viscoelastic response in terms of two frequency-dependent phenomena: dynamic AFM non-linear behaviour (conservative contribution) and the mechanical viscoelastic material piecewise response (dissipative contribution). Furthermore, an expression to estimate the contact time is derived based on the ratio of energy dissipated to energy stored in one oscillation cycle and a previous obtained loss tangent expression for AM-AFM [146]. Finally, we have numerically implemented the Standard Linear Solid (SLS) model which combines Kelvin-Voigt and Maxwell [126] and hence captures fundamental viscoelastic behaviors, namely, the stress relaxation and creep compliance.

3.1.1 Frequency dependent oscillation amplitude in AM-AFM

The dependencies of the amplitude A and phase shift ϕ on the driven frequency ω_d for equation 2.9 far from the sample ($F_{ts}=0$) are described by the Lorentzian equations for amplitude and phase,

$$A(\omega_d) = \frac{F_0}{\sqrt{(k_{eff} - m\omega_d^2)^2 + (\gamma\omega_d)^2}} \quad (3.1)$$

and,

$$\phi(\omega_d) = \arctan \frac{\gamma\omega_d}{(k_{eff} - m\omega_d^2)} \quad (3.2)$$

where k_{eff} is defined in equation 3.3, γ is the damping coefficient, ϕ is the phase lag between the driven $F_{exc} = F_0 \cos(\omega_d t)$ and its response signal whereby F_0 is the force given at the free oscillating amplitude A_0 . Such behaviour is illustrated by three values of k_{eff} in figure 3.1.

Based on the weakly perturbed harmonic oscillator approach [149], the presence of a force gradient $\frac{dF_{ts}}{dz}$ determines a variation in the force constant and resonant frequency given by,

$$k_{eff} = k - \frac{dF_{ts}}{dz} \quad (3.3)$$

and,

$$\omega_{eff} = \sqrt{k_{eff}/m} \quad (3.4)$$

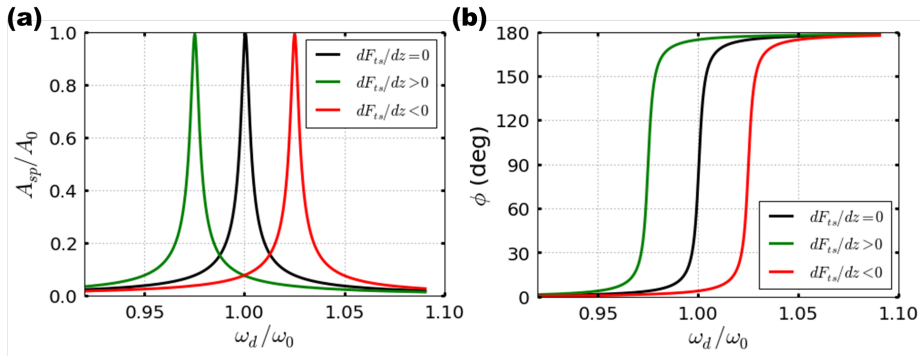


Figure 3.1: Lorentzian amplitude (a) and phase shift (b) as functions of the resonance frequencies and in dependence of the interacting force regimes. For $\frac{dF_{ts}}{dz} < 0$ a positive frequency shift takes place (red curves correspond to the value $\frac{dF_{ts}}{dz} = 0.05k$). In addition for $\frac{dF_{ts}}{dz} > 0$ a negative frequency shift appears (green curves correspond to the value $\frac{dF_{ts}}{dz} = -0.05k$). The calculated values correspond to $k_{eff} = 1$ N/m (black curves), $Q = 100$, $k_{eff}^l = 1.05$ N/m (green curves) and $k_{eff}^r = 0.95$ N/m (red curves). Adapted from [148].

By analyzing $\frac{dF_{ts}}{dz}$ in equation 3.4 two types of frequency shifts are identified. For $\frac{dF_{ts}}{dz} < 0$ the force decrease with the instantaneous distance and the effective frequency increases $\omega_{eff} > \omega_0$, while for $\frac{dF_{ts}}{dz} > 0$ the force increases with the instantaneous distance and the effective frequency decreases $\omega_{eff} < \omega_0$ (see figure 3.1).

Equations 3.3 and 3.4 let us explore a backbone concept of AM-AFM. The oscillating amplitude is affected by the gradient of the interaction forces F_{ts} whereby non-linear interactions can be better calculated through numerical simulations as shown in figure 3.2(b) [16, 78, 150]. Recently, Kiracofe and Raman [151] have performed similar calculations and experiments for liquid environment showing how the oscillation amplitude varies for a frequency shift in the range of 5-50 kHz (see figure 3.2).

3.1.2 Frequency dependent viscoelastic samples: energy dissipation of polymeric samples

Most polymeric and biological systems present a viscoelastic behaviour [152, 147, 153, 131]. Here we describe an example of a polymeric viscoelastic sample to illustrate its frequency dependent behaviour.

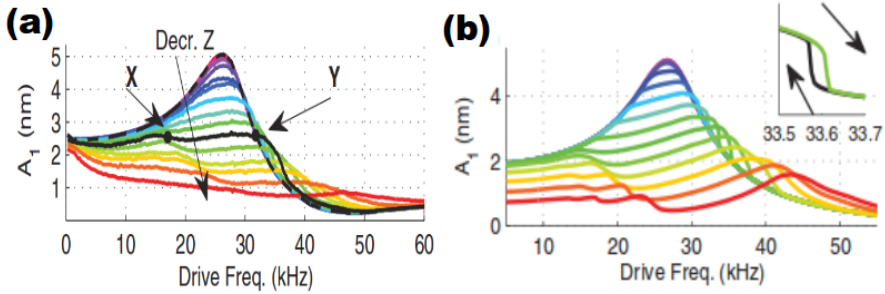


Figure 3.2: Amplitude as a function of the driving frequency for repulsive interactions in liquid: (a) experimental frequency sweeps for a commercial cantilever MAC-II ($f_0=27.4$ kHz, $k=2$ N/m and $Q=3$) in 500-mM KCl solution on mica, (b) numerical simulations frequency shift for the same cantilever and a 2 GPa sample. The inset in (b) compares a frequency sweep up and down at a fixed z_c . Colored curves correspond to the approach to the sample (decrease of z_c). The figure has been adapted from [151].

Polymeric viscoelastic sample

Polymers can form amorphous or semi-crystalline solids when cooled below their melting temperature (T_m). In order to describe these two different solidification processes, specific volume ($v^* = \rho^{-1} = V/m$) versus temperature plots are used. There are different cooling mechanisms of these materials [152, 147]. Common polymers are ruled by one of these cooling mechanisms, namely, the amorphous solid formation which takes place at the glass transition temperature (T_g). This transition reflects a change in the expansion coefficient of a material. Moreover, it is well accepted that the glass transition is not a thermodynamic phase transition, given the fact that T_g depends on the cooling rate. Furthermore, the glass transition consists in the amorphous solidification of a melted substance. This solidification process is accompanied by a drastic increase of about three orders of magnitude in the mechanical stiffness (see figure 3.6(a)). On the other hand, the viscosity suffers more abrupt changes in the range of four to six orders of magnitude, as depicted in figure 3.6(b).

Recently, Tsukruk and co-workers have experimentally probed the universal modulus-time-temperature relationship of poly (n-butyl) methacrylate PnBMA by applying Williams-Landel-Ferry (WLF) equation [154] to their force spectroscopy measurements (see figure 3.4) [99]). From figure 3.4 we can infer different states of the polymeric material. The glassy state occurs below 25 °C, where the Young modulus of the polymer correspond to E_0 , the glass transition temperature between 25-60 °C and the rubbery state above 60 °C.

In dynamic AFM, the contact time t_c is generally less than the oscillating period and hence the actual interaction contact frequency is higher than the resonance system frequency. A polymer with low glass transition temperature ($T_g < T_{room}$) can be suitable

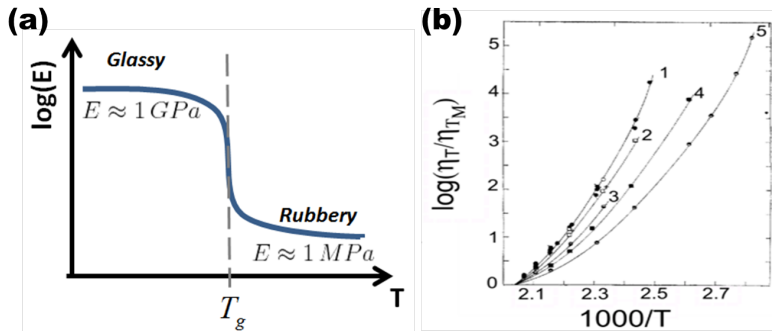


Figure 3.3: (a) Polymer melt at different temperatures $T > T_g$ rubbery material ($E_\infty \approx 1 \text{ MPa}$) and when cooled to $T < T_g$ the material turns into its amorphous or glassy state ($E_0 \approx 1 \text{ GPa}$). (b) Relative change of viscosity for a polystyrene normalized by its viscosity at $T_M = 490 \text{ K}$ against $1/T$ for different molecular weights, namely, 134000-25000 g/mol (curve 1), 13500-11000 g/mol (curve 2), 7400 g/mol (curve 3), 5100 g/mol (curve 4) and 4900 g/mol (curve 5). Adapted from [147] (figure (a)) and [152] (figure (b)).

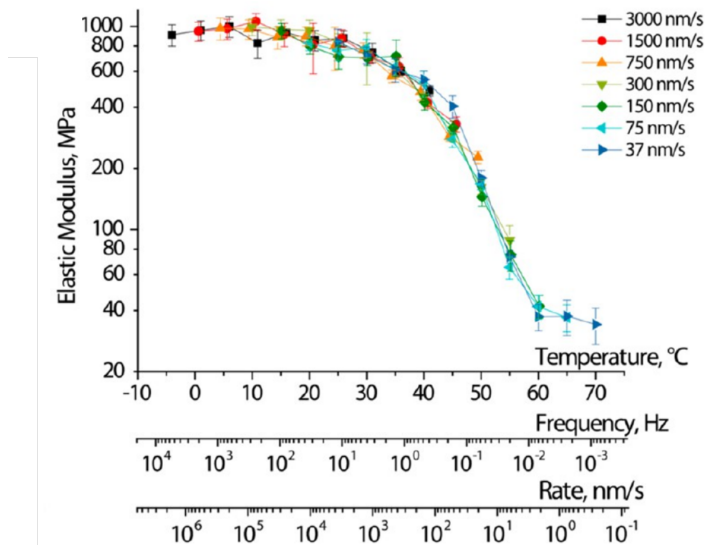


Figure 3.4: Master curve constructed with the elastic Sneddens model through the WLF equation with the reference frequency at 1 Hz. Adapted from [99].

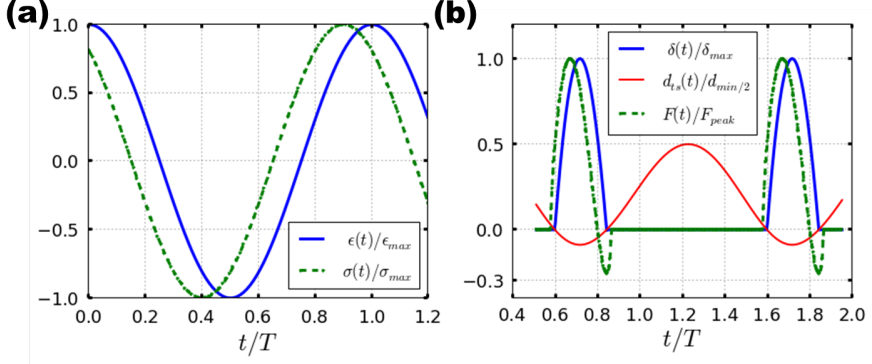


Figure 3.5: (a) Stress response ($\sigma(t)$) of a viscoelastic material to an applied strain ($\varepsilon(t)$). This figure has been adapted from [126]. (b) Simulation of the normalized viscoelastic force ($F(t)/F_{peak}$), the deformation over time ($\delta(t)/\delta_{max}$) and the tip-sample distance ($\frac{1}{2}d_{ts}(t)/d_{min}$) for the Kelvin-Voigt model. The simulation inputs are $E_s=50$ MPa, $\eta_s=300$ Pa.s and the AM-AFM operational parameters by $A_0=2$ nm, $A_{sp}=0.65 A_0$, $k=0.2$ N/m, $Q=4$, $R_t=5$ nm.

for viscoelastic properties mapping. In addition, the frequencies values need also to be found in the transition zone between E_0 and E_∞ (see figure 3.3(a)).

3.1.3 Viscoelastic material in response to a sinusoidal excitation

A sinusoidal strain excitation $\varepsilon(t)$ is applied to a viscoelastic sample. As a consequence, a resulting stress $\sigma(t)$ arises which is not synchronous to the strain $\varepsilon(t)$ and vice-versa [126, 152, 147]. Hence, a phase lag α between the stress and the strain signals (see figure 3.5(a)).

This leads naturally to a dynamic in-phase sample strain $\varepsilon(t)$ defined as,

$$\varepsilon(t) = \varepsilon_{max} \cos(\omega t) \quad (3.5)$$

where ε_{max} is the maximum strain and ω is the resonance angular frequency. The viscoelastic force response out-of-phase $\sigma(t)$ is given by,

$$\sigma(t) = \sigma_{max}(\omega) \cos(\omega t - \alpha(\omega)) \quad (3.6)$$

by expanding the cosine differences term of equation 3.6, letting,

$$\sigma(t) = \sigma_{max}(\omega) \cos(\omega t) \cos(\alpha(\omega)) + \sigma_{max}(\omega) \sin(\omega t) \sin(\alpha(\omega)) \quad (3.7)$$

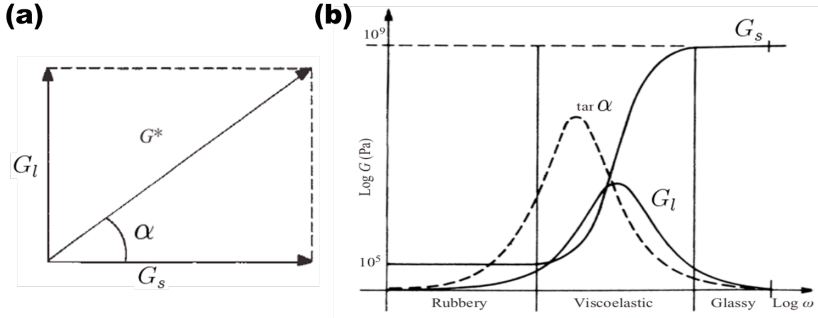


Figure 3.6: (a) The phasor diagram showing vector G_l (loss modulus), vector G_s (storage modulus) and the resulting complex modulus $G^* = G_s + G_l$. (b) The loss G_l , storage G_s moduli and the loss tangent ($\tan \alpha$) for a solid polymer as a function of the angular frequency ω . The glass transition states are shown, namely, the rubbery, the viscoelastic transition region where the higher loss modulus and hence loss tangent are observed, and at higher angular frequencies the glassy state. Adapted from [147].

In equation 3.7 we observe that the stress $\sigma(t)$ comprises two components: the first in phase with the strain given by $\sigma_{max}(\omega) \cos(\alpha(\omega))$ and the second one is 90° out of phase with the strain *i.e.* $\sigma_{max}(\omega) \sin(\alpha(\omega))$. These stress-strain relationship can be defined as two magnitudes of stress in and out of phase [147],

$$G_s(\omega) = \frac{\sigma_{max}(\omega)}{\varepsilon_{max}} \cos(\alpha(\omega)) \quad (3.8)$$

and,

$$G_l(\omega) = \frac{\sigma_{max}(\omega)}{\varepsilon_{max}} \sin(\alpha(\omega)) \quad (3.9)$$

The corresponding phasor diagram is illustrated (see figure 3.6(a)). Whereby, a complex modulus is defined in terms of the loss and the storage modulus $G^* = G_s + G_l$ and the phase lag α ,

$$\alpha(\omega) = \arctan \left(\frac{G_l(\omega)}{G_s(\omega)} \right) \quad (3.10)$$

where G_l is the loss modulus (viscous dissipation) and G_s is the storage modulus (elastic energy) [126, 147, 155]. Furthermore, α can be written in terms of the ratio of dissipated and stored energy $\tan(\alpha) = \omega(\eta_s/E_s)$ (for the Kelvin-Voigt's model [155, 146]). The loss tangent, loss and storage moduli are depicted as a frequency dependent functions in figure 3.6(b).

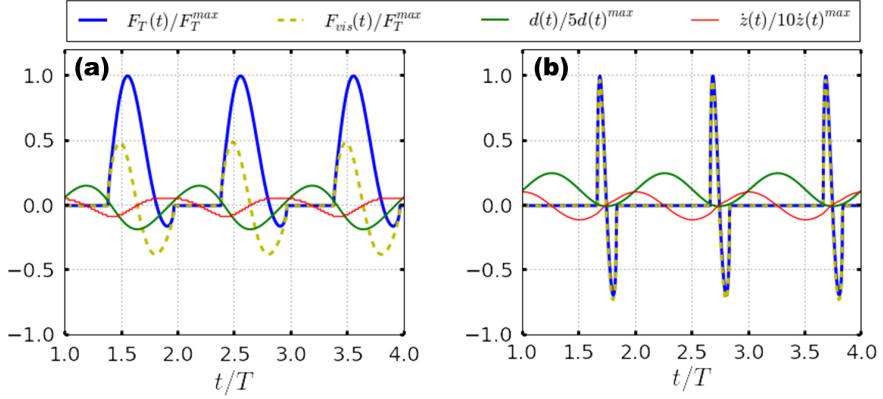


Figure 3.7: Simulations showing the instantaneous displacement, velocity and force of a cantilever tip impacting onto a soft sample for (a) low driven frequency $f_0=10$ kHz and (b) high driven frequencies $f_0=50$ kHz. The sample is modeled with $E_s=30$ MPa, $\eta_s=800$ Pa.s and the operational parameters by $A_0=2$ nm, $A_{sp}=0.65 A_0$, $k=0.2$ N/m, $Q=4$, $R_t=5$ nm. For visualization and comparison purposes the total force and viscoelastic ones have been normalized to F_T^{max} , the distance is normalized to $5x d_{max}$ and the velocity is normalized to $10x \dot{z}_{max}$.

3.1.4 Contact time of a viscoelastic material in response to the dynamic AFM tip motion

In time domain, the presence of mechanical contact between tip and sample is quantified by means of the contact time $t_c = t_c^a + t_c^r$ (see figure 3.7). Whereby, t_c^a is the approach time, when the approach velocity of the tip is negative ($\dot{z}(t) < 0$) and t_c^r is the retraction time with positive velocity $\dot{z}(t) > 0$. The mechanical properties of the sample and the operational AFM parameters determine those quantities. In AM-AFM, generally the in-contact approach time and the material's compression time are equivalent. However, the in-contact retraction time and the material's restitution/relaxation depend on the material viscoelastic properties and the interaction between tip and sample could be shorter than the time the material needs to recover from the deformed stage to its initial stage (considering only one cycle of oscillation and no viscous load/unload history of the interaction).

3.2 Quantification of the viscoelastic interaction force from a piecewise material excitation

Based on equations 3.5 and 3.6, the deformation and the interaction force produced by the oscillating AFM tip while in contact with a viscoelastic sample in time domain are presented hereunder (see figure 3.5(b)). First the deformation can be written as a piecewise function by,

$$\delta(t) = \delta_{max} \cos(\omega_c t), \quad d(t) < 0, \quad t \in [0, T_d] \quad (3.11)$$

where δ_{max} is the maximum prescribed deformation and ω_c is the contact angular frequency ($f_c = 1/(2t_c)$) as depicted in figure 3.5(b)). The value of the tip-sample distance ($d(t) < 0$) denotes the piecewise definition of a time-dependent function of a period given by $T_d = 1/f_d$. Then from equation 3.6, the force term $F(t)$ is given by,

$$F(t) = F_{peak}(\omega_c) \cos(\omega_c t - \alpha(\omega_c)), \quad d(t) < 0 \quad (3.12)$$

by expanding the cosine term (analogous to the procedure followed in [147]),

$$F(t) = F_{sto}(\omega_c) \cos(\omega_c t) + F_{loss}(\omega_c) \sin(\omega_c t), \quad d(t) < 0 \quad (3.13)$$

where $F_{sto}(\omega_c) = F_{peak}(\omega_c) \cos(\alpha(\omega_c))$ is the instantaneous force in phase to the deformation and $F_{loss}(\omega_c) = -F_{peak}(\omega_c) \sin(\alpha(\omega_c))$ is the instantaneous force 90° out of phase with the deformation. Then, following the definitions described in section 3.1.3 and since the deformation function defined in equation 3.11 is a cosine and considering that the conservative forces depend on the deformation $\delta(t)$ and the model for the dissipative force depends on the deformation rate $\dot{\delta}(t)$. On the other hand, the maximum force magnitudes can be modeled by the Hertz and Kelvin-Voigt's models. Hence,

$$F_{sto} = \frac{4}{3} E_s \sqrt{R_t} \delta_{max}^{3/2}, \quad d(t) < 0 \quad (3.14)$$

and,

$$F_{loss} = -\eta \sqrt{R_t} \dot{\delta}_{max}, \quad d(t) < 0 \quad (3.15)$$

where equations 3.14 and 3.15 have been previously described (see section 2.4). In addition, the deformation rate $\dot{\delta}(t)$ can be obtained from 3.11 as,

$$\dot{\delta}(t) = -\omega_c \delta_{max} \sin(\omega_c t), \quad d(t) < 0 \quad (3.16)$$

According to the harmonic approximation used to solve the point-mass model (equation 2.9), $z(t)$ is,

$$z(t) = z_0 + A_{sp} \cos(\omega_d t - \phi) \quad (3.17)$$

letting its first derivative,

$$\dot{z}(t) = -\omega_d A_{sp} \sin(\omega_d t - \phi) \quad (3.18)$$

where A_{sp} is the amplitude of work (A_{sp} =Amplitude Ratio x A_0), ω_d is the driven frequency and ϕ is the phase shift between the excited and response oscillating signals of the microscope. As described previously in chapter 2, the deformation δ is defined as $\delta(t) = a_0 - z_c - z(t)$ and thus $\dot{\delta}(t) = -\dot{z}(t)$. Hence,

$$\dot{\delta}(t) = \omega_d A_{sp} \sin(\omega_d t - \phi), \quad d(t) < 0 \quad (3.19)$$

Combining equations 3.11, 3.14, 3.15 and 3.19 we obtain,

$$F_{sto}(t) = \frac{4}{3} E_s \sqrt{R_t} \sqrt{\delta_{max} \cos(\omega_c t)} (\delta_{max} \cos(\omega_c t)), \quad d(t) < 0 \quad (3.20)$$

and,

$$F_{loss}(t) = -\eta_s \sqrt{R_t} \sqrt{\delta_{max} \cos(\omega_c t)} (\omega_d A_{sp} \sin(\omega_d t - \phi)), \quad d(t) < 0 \quad (3.21)$$

The variables relating both material and instrumental parameters can be identified and denoted as *key variables* ($\delta_{max}, \omega_c, \phi$). In addition to the key variables, there are two input ones, A_{sp} and ω_d . To gain a better insight into the effect of those variables we have calculated the peak viscoelastic forces for a sample with $E_s=30$ MPa and $\eta_s=800$ Pa.s which are the values used in previous articles [97, 99]. The simulations explore three typical set-point amplitudes values $A_{sp} = [0.9A_0, 0.65A_0, 0.4A_0]$ over a driven resonance frequency sweep in the range of 5-50 kHz (typical values used in liquid [68, 151]). By using the material relaxation time τ we can define a reference material frequency as $f_{mat} = 1/\tau$ (with $\tau = \eta_s/E_s$). In what follows the low or high reference within this section are referenced to f_{mat} . Figure 3.8 shows the difference between the instantaneous viscoelastic forces for low ($f_d=5$ kHz) and high ($f_d=50$ kHz) driven frequencies and their corresponding set-point amplitudes. In addition, the case without viscosity is shown (see figure 3.8(a)) whereby the peak force increases with the lower A_{sp} values. According to our results depicted in figure 3.8(b) at lower frequencies the effect of an amplitude reduction (lower set-points) to the viscoelastic force goes along with the elastic case (figure 3.8(a)). On the contrary, at higher frequencies (figure 3.8(c)) the effect of reducing the oscillation amplitude (lower set-points) does not necessarily imply higher peak forces, in fact the elastic component is reduced and the interaction force is mostly driven by the deformation rate (figure 3.8(c)).

The calculated *key variables* allowed us to verify our modeling by replacing them into the conservative force contribution (equation 3.20) and the dissipative one (equation

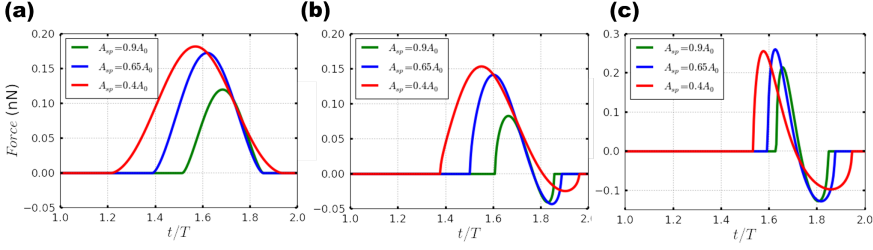


Figure 3.8: Comparison between simulations of the elastic (a) $f_d=5$ kHz with $A_{sp}=0.9A_0$ (red curve), $A_{sp}=0.65A_0$ (blue curve) and $A_{sp}=0.4A_0$ (green curve), and viscoelastic response for low and high frequencies (b) $f_d=5$ kHz with $A_{sp}=0.9A_0$ (red curve), $A_{sp}=0.65A_0$ (blue curve) and $A_{sp}=0.4A_0$ (green curve), and (c) $f_d=50$ kHz with $A_{sp}=0.9A_0$ (red curve), $A_{sp}=0.65A_0$ (blue curve) and $A_{sp}=0.4A_0$ (green curve). Simulation data, $k=0.2$ N/m, $E_s=50$ MPa, $\eta_s=800$ Pa.s (except in (a) where $\eta_s=0$ Pa.s), $Q=2$, $A_0=2$ nm, $A_{sp}=0.9 A_0$ and $R_t=5$ nm. Kelvin-Voigt's model has been used to describe the sample.

3.21). The sum of both contributions is defined here as the reconstructed peak viscoelastic force. Figure 3.9(a) shows the comparison of the reconstructed viscoelastic peak force and the simulated one for low excitation frequencies ($f_d=10$ kHz) and low set-point amplitudes ($A_{sp}=0.4A_0$). The Kelvin-Voigt model describe a sample characteristic relaxation/restitution time given by $\tau = \eta_s/E_s \sim 26 \mu\text{s}$. Moreover, Kelvin-Voigt's model (equation 2.44) is proportional to the deformation rate which depends on the deformation and contact frequency ω_c . For a constant maximum deformation, the viscous force in dynamic AFM is a function of the contact frequency ω_c which increases monotonically with the driven frequency ω_d . This analysis lead us to the conclusion that higher peak viscoelastic forces are expected for higher driven frequencies. In figure 3.9(b) we observe an acceptable agreement of the simulated and reconstructed peak viscoelastic forces for low set-point amplitudes ($A_{sp}=0.4A_0$) with an error within 15 % of the simulated values. Nonetheless, for higher set-point amplitudes the deviation increases to error values near 40 % between the reconstructed peak viscoelastic force and the simulated one. Whereby the highest percentile errors are in general placed at the highest frequencies. This deviation can be understood by two complementary reasons. First, the reconstructed method assumption on the tip's velocity and the deformation rate $\dot{\delta}(t) = -\dot{z}(t)$ which implies that any wave effect on the sample [156] is neglected during the contact time (equation 3.19). On the other hand, this behaviour could also be subject to the surface relaxation during each oscillating cycle that has not been considered in the reconstruction method (viscous material load/unload memory or history). In fact, the sample height recovery for a linear viscoelastic model is a function of the restitution/relaxation time and takes place only when $t_c > \tau$ [126, 147]. With this re-

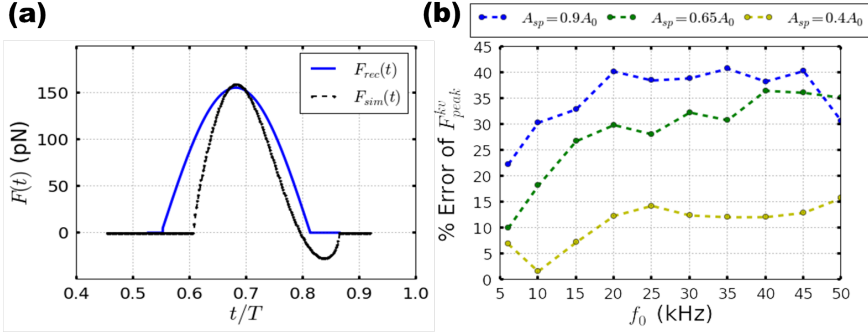


Figure 3.9: Comparison between simulation and the semi-analytical approach to estimate viscoelastic forces (a) shows the recovered peak interaction force (blue curve) and the simulated value for $A_{sp}=0.4A_0$ and $f_0=10\text{kHz}$ (b) summarizes the discrepancies between the recovered and simulated peak viscoelastic force values as a function of A_{sp} and f_0 . Simulation data, $k=0.2\text{ N/m}$, $E_s=30\text{ MPa}$, $\eta_s=800\text{ Pa.s}$, $Q=2$, $A_0=2\text{ nm}$ and $R_t=5\text{ nm}$. A combination of the Kelvin-Voigt's and Hertz models has been used to describe the viscoelastic interaction.

gard, better results of the reconstructed viscoelastic force should be obtained for longer t_c and hence lower ω_d which are the conditions given at $A_{sp}=0.4A_0$. Furthermore, other viscoelastic phenomena may be oversimplified in the Kelvin-Voigt's model, such as the stress relaxation [127]. Then, we have repeated the calculations with an alternative linear viscoelastic model: the Standard Linear Solid (SLS) that is the simple model that describe two viscoelastic behaviors, namely, creep compliance and stress relaxation. The SLS model has been also implemented to our modeling framework and simulations (see section 2.4 for an additional description).

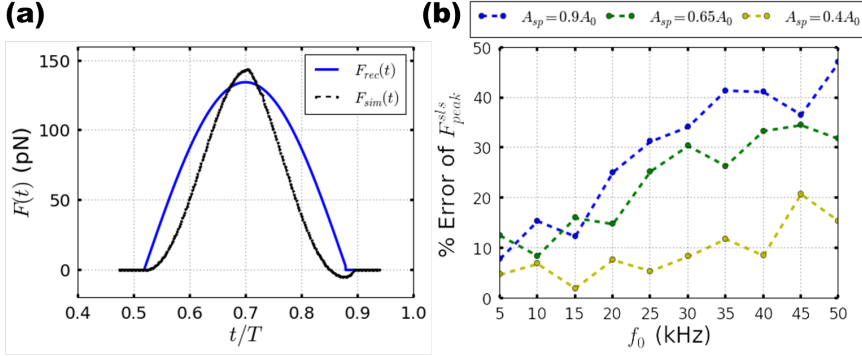


Figure 3.10: Comparison between simulation and the semi-analytical approach to estimate viscoelastic forces (a) shows the recovered peak interaction force (blue curve) and the simulated value for $A_{sp}=0.4A_0$ and $f_0=10\text{kHz}$ (b) summarizes the discrepancies between the recovered and simulated peak viscoelastic force values as a function of A_{sp} and f_0 . Simulation data, $k=0.2\text{ N/m}$, $E_s=30\text{ MPa}$, $\eta_s=800\text{ Pa}\cdot\text{s}$, $Q=2$, $A_0=2\text{ nm}$ and $R_t=5\text{ nm}$. A combination of the SLS and Hertz models has been used to describe the viscoelastic interaction.

From the SLS model of equation 2.48 the dissipative force term of equation 3.22 is given by,

$$F_{loss}(t) = \frac{E_0\eta_s}{E_0 + E_\infty} \left[\sqrt{R_t} \sqrt{\delta_{max} \cos(\omega_c t)} (\omega_d A_{sp} \sin(\omega_d t - \phi)) - \dot{F}(t)/E_0 \right] \quad (3.22)$$

where $\dot{F}(t)$ denotes the first derivative of equation 3.13, $\tau = \frac{E_0 - E_\infty}{E_\infty E_0} \eta_s$ is the characteristic material relaxation/restitution time and E_0 is assumed to be the instantaneous sample Young modulus (the value assumed here is $E_0=1\text{ GPa}$, which reflects a near two order of magnitude greater than $E_\infty=30\text{ MPa}$).

Figure 3.10(a) shows the results of the reconstructed viscoelastic peak force and the simulated one for the SLS model. Starting from the lowest set-point amplitude ($A_{sp}=0.4A_0$) the error is slightly increased to 20 % while for the Kelvin-Voigt's case reached at most 15 %. On the other hand for higher set-point amplitudes the error between the reconstructed and simulated force rise to circa 50 %. Whereby the highest percentile errors are in general placed at the highest frequencies. As previously described for Kelvin-Voigt's model the same explanations apply, however the SLS model has another complexity which is the estimation of the force derivative which in our implementation it is obtained from the simulated $F(t)$ which can be a very sensitive value at high frequencies as depicted in figure 3.7.

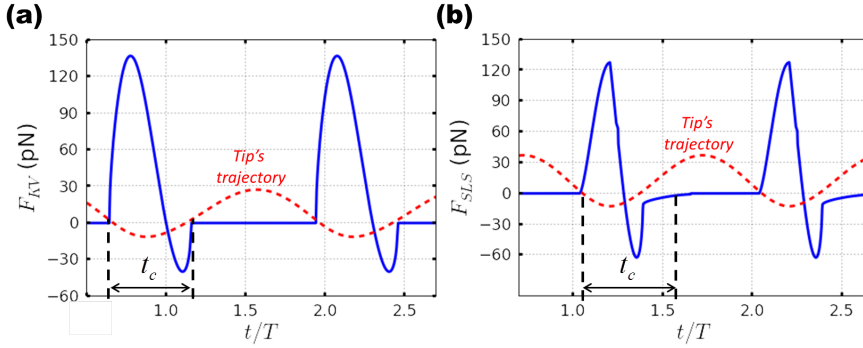


Figure 3.11: Show the difference in contact time for both (a) Kelvin-Voigt's and (b) the SLS models. Simulation data, $k=0.2$ N/m, $E_s=30$ MPa, $\eta_s=800$ Pa.s, $Q=2$, $A_0=2$ nm, $A_{sp}=0.65A_0$ and $R_t=5$ nm.

Figure 3.11, describes the force experienced by the sample for both Kelvin-Voigt's and SLS models. Whereby the latter shows a longer relaxation time τ_{sls} and its forces depicts also a sharper shape while the sample finishes the compression time t_c^a and starts its relaxation period because of the added stress relaxation term.

Interestingly, both the deformation rate (equation 3.16) and the deformation (equation 3.11) are represented in terms of sine $[\dot{\delta}(t)]$ and cosine $[\delta(t)]$, respectively. Hence, if the deformation value grows, the deformation rate decreases and vice-versa. In addition, the results obtained for both models (figures 3.9 and 3.10) show better agreement whenever the contact time is increased i.e. the higher the deformation and thus higher contact time. This can be understood only by considering a reversible deformation regime (linear viscoelasticity) [126, 147, 155]. It is also important to note that for higher driven frequencies the viscoelastic regime of some polymeric-like samples may be abruptly reduced which means that viscosity is not any longer being mapped (see figure 3.6).

3.3 Observables of the time-dependent viscoelastic force reconstruction

As identified earlier, the three key variables (observables) needed to reconstruct viscoelastic forces are: ϕ , δ_{max} and t_c . In this section, an interpretation of these key parameters is further provided.

3.3.1 AM-AFM phase shift ϕ

The phase shift ϕ has been represented by two analytical relationships [145, 157]. Here, we adopt the one based on the dissipated energy [145],

$$\sin(\phi) = \frac{\omega_d}{\omega_0} \frac{A_{sp}(\omega_d)}{A_0} + \frac{QE_{dis}}{\pi k A_{sp}(\omega_d) A_0} \quad (3.23)$$

with,

$$E_{dis} = - \int_0^{T_d} F_{ts}(t) \dot{z}(t) dt \quad (3.24)$$

Note that the first term of equation 3.23 describes a purely elastic material whereby a linear dependence of $\sin(\phi)$ with A_{sp}/A_0 takes place. However, for viscoelastic materials an additional term is introduced as a function of E_{dis} , which can be approximated as: $E_{dis} = E_{ext} - E_{med}$. Where $E_{ext} = \pi F_0 A_{sp}(\omega_d) \sin(\phi)$, determines the system excitation energy and $E_{med} = \pi k \omega_e A_{sp}^2(\omega_d) / (Q \omega_0)$, the energy dissipated due to the microcantilever damping in the operating media. Equation 3.23 has also helped to consolidate the phase shift as a well-established AM-AFM observable [158, 145, 157, 159]. In what follows, we assume ϕ to be constant for each tip-sample average distance (z_c). To address our calculation the phase shift values can be obtained experimentally.

3.3.2 Maximum deformation δ_{max}

The maximum deformation is theoretically determined by $\delta_{max} = a_0 - z_c - z(t)$ whereby a_0 is the intermolecular distance (a typically adopted value is 0.165 nm), $z(t)$ is the instantaneous tip deflection and z_c is the tip-sample average distance (fixed along the steady-state oscillating cycles). The value of z_c cannot be determined in advance because it will also depend on the material mechanical properties of the sample (in our case E_s and η_s). Based on the Hertzian mechanics hypothesis for a parabolic indenter, the maximum deformation may be determined by $\delta_{max} \ll R_t$ [155, 160]. An alternative approach is to estimate a prescribed deformation through control mechanisms such as using constant amplitude FM-AFM [127, 161, 162]. However, for an AM-AFM experiment the maximum indentation can be experimentally estimated in the repulsive regime under a force-curve basis. To this end, we can redefine $\delta_{max} = A_{sp} + z_0 - z_p$ where δ_{max} depends only on experimental observables: A_{sp} is the negative work amplitude value, z_0 is the cantilever deflection and z_p the piezo distance. Note that under such conditions the tip approach to the sample at a value $z_p = z_{int}$ (with z_{int} is the point where the amplitude and phase present changes in a AM-AFM approach curve) denotes the beginning of the repulsive interaction, *i.e.* the point where the tip will start indenting the sample.

3.3.3 Contact time t_c

When the dissipative force follows Kelvin-Voigt's and/or SLS models and we sought to work in a reversible penetration regime, the contact time (t_c) shall be at least close to the retardation/restitution time (τ). Remarkably, for much smaller contact times the material deformation rates should not be relevant, or in other words viscoelasticity is not being mapped. This can be further understood by explaining the mechanical properties of a well-characterized glassy polymer of section 3.1. Nevertheless, t_c is not an experimental observable.

3.3.3.1 Estimation of the contact time t_c by means of the loss tangent for the Kelvin-Voigt model

The characteristic sample time according to Kelvin-Voigt's model is $\tau = \frac{\eta_s}{E_s}$. We assume that τ is fixed under certain ambient conditions. According to the formulation described in section 3.2 the loss tangent can be written by means of F_{sto} and F_{loss} ,

$$\tan(\alpha) = \frac{F_{loss}}{F_{sto}} \quad (3.25)$$

by combining 3.14 and 3.15,

$$\tan(\alpha) = \frac{3\eta_s\omega_d A_{sp} \sin(\omega_d t - \phi)}{4E_s\delta_{max} \cos(\omega_c t)} \quad (3.26)$$

where the variables have been already defined in this chapter. Equation 3.26 is based on the loss and storage forces while tip and sample established mechanical contact which can be turned into mechanical work by multiplying F_{loss} and F_{sto} times the mechanical displacement during the interaction with the sample which in this case is assumed to be the same for both F_{loss} and F_{sto} . Note that the values of the loss tangent for a viscoelastic sample shall be comprised in the $0 < \alpha < \pi/2$, where 0 determines that the sample is elastic and $\pi/2$ liquid. Then equation 3.26 is obtained from the mechanical properties of the sample and AM-AFM observables. Previously, a loss tangent expression has been derived by means of only instrumental observables as [146],

$$\tan(\alpha)_{exp} = \frac{\sin(\phi_1) - \sum n^2 \frac{A_n^2}{A_0 A_1}}{\cos(\phi_1) + Q \sum n^2 \frac{A_n^2}{A_0 A_1 (n^2 - 1)}} \quad (3.27)$$

where n is the order of the harmonic and A_n the amplitude at the n th harmonic (ranging from the fundamental at $n=1$ up to N), A_0 is the free oscillation amplitude, ϕ_1 is the phase shift of the first harmonic and Q is the quality factor. Proksch and Yablon have further implemented equation 3.27 to provide an additional material compositional channel (loss tangent imaging) to experiments on soft materials.

Combining equations 3.27 truncated in to the first harmonic and 3.26 lead us to,

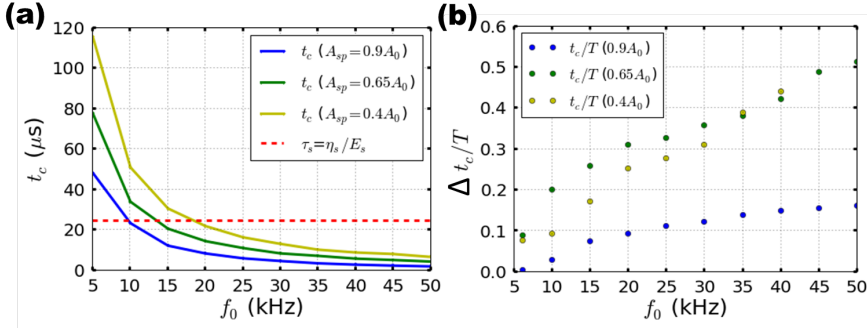


Figure 3.12: (a) Simulated values of the contact time as a function of a range of driven frequencies (5 - 50 KHz) for three different set-point amplitudes $A_{sp} = 0.9A_0$, $A_{sp} = 0.65A_0$ and $A_{sp} = 0.4A_0$. The dashed red line represents the material retardation/restitution time τ_s . (b) Normalized discrepancies between the reconstructed contact time (using equation 3.29) and the simulated values. Color codes for the different set-point amplitudes $A_{sp} = 0.9A_0$ (blue), $A_{sp} = 0.65A_0$ (green) and $A_{sp} = 0.4A_0$ (yellow). Simulation data, $k=0.2$ N/m, $E_s=30$ MPa, $\eta_s=800$ Pa.s, $Q=4$, $A_0=2$ nm and $R_t=5$ nm. Kelvin-Voigt's model has been used to describe the viscoelastic interaction.

$$\tan(\alpha)_{exp} = \frac{3\eta_s\omega_d A_{sp} \sin(\omega_d t - \phi)}{4E_s\delta_{max} \cos(\omega_c t)} \quad (3.28)$$

and hence for $t = t_c$,

$$\frac{t_c}{T} = \frac{\arcsin\left(\frac{4\delta_{max}}{3A_{sp}\tau\omega_d} \tan(\alpha)_{exp}\right) + \phi}{\pi} \quad (3.29)$$

where t_c/T is the normalized contact time, $\tan(\alpha)_{exp}$ can be calculated by means of equation 3.27, among the previously defined variables. To validate the derived expression for the mechanical contact time we have compared the analytical solution and simulations values for a range of driven frequencies (5 - 50 KHz) and three different set-point amplitudes $A_{sp} = [0.9A_0, 0.65A_0, 0.4A_0]$ (see figure 3.12(b)).

Figure 3.12(a), shows the simulations result for the contact time along a range of driven frequencies (5-50 kHz) and A_{sp} . The material retardation/restitution time τ_s is also represented with a dashed red line (according to Kelvin-Voigt's model). In figure 3.12(b), the difference between the calculated (using equation 3.29) and simulated values is shown. The $Y - axis$ has been normalized to the nominal value of the period T for each driven frequency. Moreover, at very low frequencies, say below 10 kHz, a relative good agreement is observed. Elsewhere the values calculated with equation 3.29 diverge over a 10 % of the nominal period T .

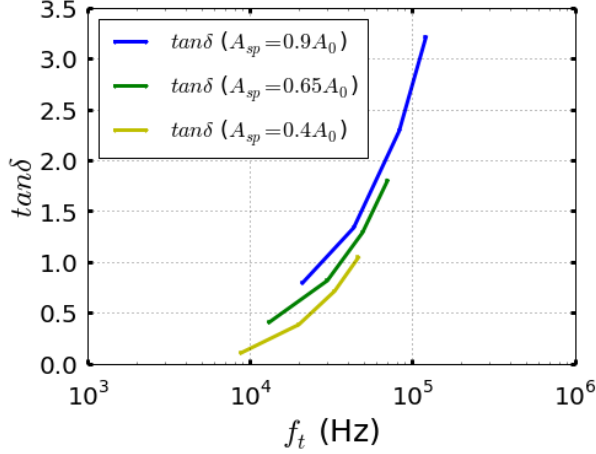


Figure 3.13: Loss tangent as a function of the excitation frequency for 3 different set-point amplitude. The loss tangents of the $A_{sp} = 0.9A_0$ and $A_{sp} = 0.65A_0$ have been shifted in the Y-axis 0.1 and 0.3 upwards, otherwise they will superpose to each other.

The equation for recovering the contact time presented along this section (equation 3.29) serves as a baseline case to show how sensitive the AM-AFM observables are to the viscoelastic behaviour. In particular, when different driven frequencies are analyzed. By using equation 3.27 and the AM-AFM experimental values of A and ϕ the loss tangent has been calculated for very soft materials (cells) whereby the loss tangent values observed can be higher than the unity [163, 131] (as the ones shown in figure 3.13 calculated from the simulated values for Kelvin-Voigt's model). Such results remark that at certain driven frequency the energy dissipated is higher than the conservative one while tip and sample are in mechanical contact. Likewise, this results suggest that a sample irreversible material deformation may occur because of the high sampling frequency applied to the sample. Nonetheless, more complex viscoelastic phenomena are envisioned when the time-domain response of the force, deformation and deformation rate are included.

3.4 Conclusions

We have developed a method to recover the peak viscoelastic forces. This method is based on three key variables: the set-point amplitude (A_{sp}), the phase shift (ϕ) and the contact time t_c within an AM-AFM experiment. The results presented here compare the reconstructed viscoelastic peak forces values to the simulated ones using two different

viscoelastic models, namely, the Kelvin-Voigt's and Standard Linear Solid ones. For both models the results show that the method is valid over a combined range of low driving frequencies ($\tau \sim t_c$) and/or low set-point amplitudes ($A_{sp} \sim 0.4 A_0$). However, one can envision that this range could be extended according to the timescales of the sample relaxation τ and the resulting contact time t_c in AM-AFM. Moreover, this results also suggest that for capturing the viscoelastic behaviour of a material (using dynamic AFM), a range of different instrumental timescales shall be included. In addition, our method provides a rapid estimation of the peak viscoelastic force by adding conservative and dissipative force terms which show a strong dependency on the deformation ($\delta(t)$) and deformation rate ($\dot{\delta}(t)$). The latter reveals a growing peak viscoelastic force value for higher driven frequency where the sample material may not reach its relaxation time. We have also proposed an analytical expression based on the loss tangent approximation provided by Proksch [146], to estimate the contact time from experimental observables A , ϕ and the operational parameters used. This expression has been compared to the simulated contact time for the Kelvin-Voigt's model. The results show that to circumvent an error above 10 % of the total oscillation period the chosen driven frequencies shall be in accordance with $\tau \sim t_c$, in other words driving the frequency below the material relaxation frequency and hence increasing the interaction/contact time t_c . Remarkably, this study also show that at high frequencies viscous interactions ($f(\dot{\delta})$) could be dominant over elastic interactions ($f(\delta)$) whereby AM-AFM experimental observables are required to provide an accurate value for $\dot{\delta}$ which to our knowledge has not been provided under a time-resolved signal. Note also that this study has been carried out within the frequencies of the *viscoelastic transition* regime, where the viscoelastic behaviour are defined by the creep compliance and stress relaxation of the sample material.

Chapter 4

Peak Forces in Amplitude Modulation AFM in Liquid

4.1 Peak forces and high-resolution imaging of soft-matter in liquid

The maximum force exerted by the tip of a force microscope on the sample surface is a critical factor that determines the spatial resolution and the degree of invasiveness of the measurement, in particular on soft materials. Here, we determine the conditions needed to image soft matter in the 30-500 MPa range while applying very small forces. Imaging at sub-50 pN in the elastic regime can only be achieved under strict conditions in terms of force constant values (below 0.2 N/m) and free amplitudes (below 2 nm) [81, 121]. The peak force depends on the operational parameters, probe properties, the elastic and/or viscoelastic response of the sample and on the contact mechanics model. Images of heterogeneous samples are never taken at a constant peak force. Under the same operational conditions, smaller forces are obtained on more compliant materials. We also find that the viscoelastic response reduces the peak force with respect to the purely elastic regions. Our findings are summarized in three-dimensional maps that contain the operational conditions for imaging at low forces. Furthermore, those operational conditions have been tested through molecular resolution images of IgM antibodies.

4.1.1 Peak forces modeling for Hertz and Tatara contact mechanics models

A detailed description of the equation of motion, the numerical simulations and the modeling of the tip-surface forces are found in Chapter 2. Here, the tip-surface force includes

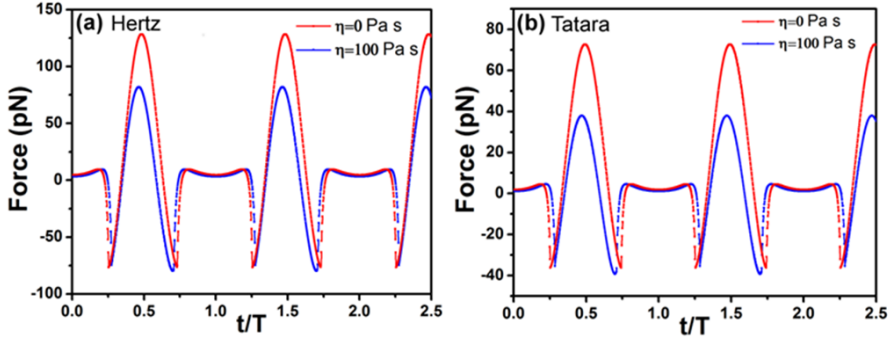


Figure 4.1: Time-varying force for $E_s=50$ MPa with and without viscous response. The simulations include DLVO forces. For each curve, the maximum value in the force curve is the peak force. Two full oscillations are shown. (a) Hertz. (b) Tatara.

contributions from repulsive contact mechanics forces (as given by Hertz or Tatara), Derjaguin-Landau-Verwey-Overbeek (DLVO) electrostatic forces [122] and viscoelastic forces deduced from linear approximations, then

$$F_{ts} = F_{Hertz(Tatara)} + F_{DLVO} + F_v \quad (4.1)$$

Figure 4.1 illustrates the definition of the peak force in time-varying force plots. The curves show a repulsive tail followed by a short attractive region (both coming from DLVO forces¹) which ends once the tips establishes mechanical contact with the surface. There are two additional observations. First, under the same operational conditions, Hertz contact mechanics gives larger forces than Tatara. Second, the peak force is reduced by considering a viscoelastic response as previously explained in Chapter 3.

The behavior of the peak force as a function of the sample's Young modulus in the range of 30 to 500 MPa is plotted in figure 4.2. This figure shows that the force given by Hertz increases with E_s from 100 pN ($E_s=40$ MPa) to 230 pN at 500 MPa (elastic case). The estimated peak force is reduced significantly by using Tatara. For the same range of E_s the force goes from 55 pN to 155 pN. This trend is preserved when the material has a viscoelastic response, although the values of the peak forces are smaller. Increasing E_s reduces the role of the viscous force because the indentation is smaller (see insets in figure 4.2), the contact time t_c decreases and hence the contribution of viscous interaction.

¹In this Chapter unless explicitly mentioned all simulations include DLVO interactions. The simulation data are $\chi_t=0.032$ C/m² ([125]), $\chi_s=0.05$ C/m² ([125]), $\epsilon=79$, $\epsilon_0=8.85 \times 10^{-12}$ C²N⁻¹m⁻², $\lambda_D=0.48$ nm and $H=0.5 \times 10^{-20}$ J.

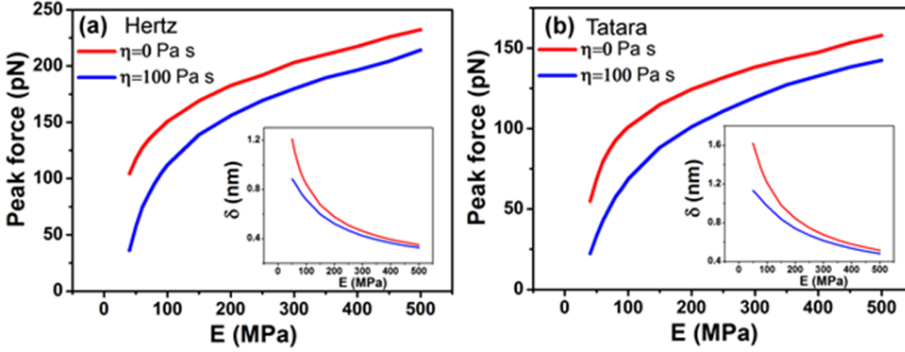


Figure 4.2: (a) Dependence of the peak force on the sample's Young modulus for elastic (Hertz) and viscoelastic responses. (b) Dependence of the peak force as a function of the sample's Young modulus by using Tataro. Simulation data, $k=0.2$ N/m, $f_0=25$ kHz, $Q=2$, $A_0=1$ nm, $A_{sp}=0.9 A_0$, $R_t=5$ nm and $R_s=4$ nm.

The dependence of the peak force on the material might be surprising because the simulations have been performed for the same operational parameters ($A_0=1$ nm, $A_{sp}=0.9$ nm) and tip's parameters ($k=0.2$ N/m, $R_t=5$ nm, $Q=2$ and $f_0=25$ kHz). The above dependence shows that the transformation of the kinetic energy of tip into the sample's potential energy is mediated by other factors such as the contact time (t_c) and the deformation (δ). Under the same operational conditions, the stiffer the material the higher the peak force and the shorter the contact time. This result implies that imaging of heterogeneous surfaces is never accomplished at a constant peak force value for a given A_{sp} . Tataro contact mechanics releases the vertical load into both vertical and lateral deformations which, in turns, reduces the peak force with respect to Hertz. It also considers the object with a finite size. However, the qualitative behavior of the curves is independent of the contact mechanics model ². For the above reasons, Tataro model (with the addition of DLVO and viscoelastic forces) has been used to generate the data shown in what follows within this Chapter.

4.2 Peak forces dependence on the set-point amplitude A_{sp}

Figure 4.3 shows the dependence of the peak force with A_{sp} . For $E_s=50$ MPa the peak force shows a small increase with decreasing A_{sp} from A_0 to $0.75A_0$. For lower A_{sp} values the graph shows a sudden increase (from ~ 50 pN ($A_{sp}=0.95A_0$) to ~ 1.2 nN

²This section has been adapted from the Author's publication [81].

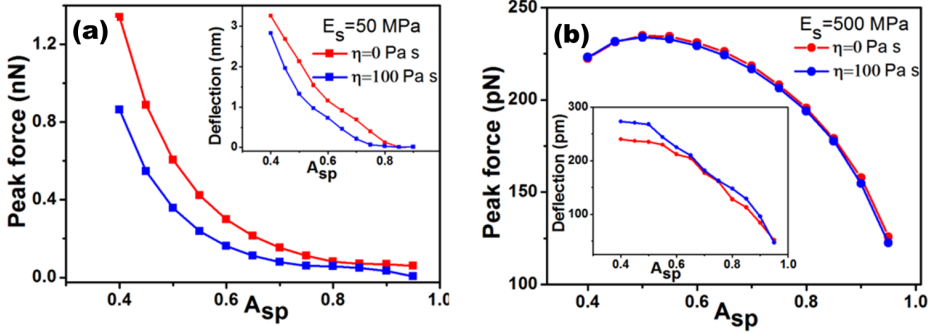


Figure 4.3: Dependence of the peak force with set-point amplitude.(a) $E_s=50$ MPa and $\eta_s=0$ and 100 Pa.s and (b) $E_s=500$ MPa and $\eta_s=0$ and 100 Pa.s. The insets show the dependence of the deflection z_0 with respect to A_{sp} . Contact mechanics are given by Tataru. Simulation data, $k=0.2$ N/m, $f_0=25$ kHz, $Q=2$, $A_0=1$ nm, $A_{sp}=0.9 A_0$, $R_t=5$ nm and $R_s=4$ nm. Contact mechanics by Tataru.

when A_{sp} is decreased to $0.4A_0$). This behavior is not present in stiffer materials ($E_s=500$ MPa see figure 4.3(b)). For viscoelastic materials, the sudden increase of the peak force is still present for $E_s=50$ MPa (Figure 4.3(a)). For stiff materials the curves show a maximum with A_{sp} .

The above results underline the different response between soft and stiff materials to the tip interactions. They also show the existence of two different mechanisms for the generation of peak force values. In the absence of dissipation, the reduction of the amplitude is caused by the detuning of the resonance curve [150]. For high Young modulus materials, the peak force follows the trend of the minimum tip-surface distance with A_{sp} which has a minimum [97]. However, for soft materials and small A_{sp} values, the amplitude can only be reduced by introducing a significant tip's deflection. A positive tip's deflection is achieved by the feedback mechanism that moves the z position of the sample with respect to the tip until the A_{sp} is reached. This interpretation is confirmed by observing the correlation between the peak forces and the cantilever deflection (insets in figure 4.3). In soft matter, the presence of high values of the cantilever deflection (relative the oscillation amplitude) implies that the tip is in contact with the sample during the whole oscillation cycle.

4.3 Permanent contact and the degree of invasiveness

4.3.1 Sample deformation in terms of E_s , A_0 and R_t

The deformation (indentation) exerted by the tip can be considered as an indicator of the degree of invasiveness of the technique. The dependence of the indentation on the Young modulus for Hertz and Tataru models is shown in figure 4.4. The indentation values are computed and normalized by the free amplitude for two values, respectively, 1 and 10 nm and two tip radii, 5 and 10 nm. The two-color coded curve separates operational parameters where the deformation is smaller than the set-point amplitude from those where the deformation is larger. As expected, the indentation increases by decreasing the Young modulus of the sample. Remarkably, for very soft materials (say those with $E_s < 100$ MPa) the indentation values are close to or even larger than the set-point amplitude. This means that the tip and the sample are in permanent contact during the tip's oscillation. This result was observed experimentally by Raman and Cartagena [129, 131] while imaging cells. Notice that decreasing the set-point amplitude on soft samples with sharper probes turns into higher deformations and hence the possible operation on a permanent contact oscillatory regime. Hertz contact mechanics gives smaller indentations than Tataru because Tataru's model considers two contact points, namely, the tip-sample one and the sample-substrate (Section 2.4.4.2 provides a mathematical description of this model). In addition, this results underlines that the relevance of the contribution from the static deflection cannot be neglected in liquid while imaging soft materials [81, 121]. However, the above effect decreases for the same A_{sp}/A_0 ratio by increasing the free amplitude as shown in figure 4.4.

4.4 Peak forces dependence on the force constant k

The dependence of the peak force with the cantilever force constant is shown in figure 4.5 for two different values, 50 and 500 MPa ($A_{sp} = 0.9A_0$, $A_0 = 1$ nm). In both cases without viscosity the dependence of F_{peak} with k is almost linear although some minor deviations are observed for low force constants. Likewise, for the 500 MPa material with viscosity the linear trend is also observed. However, in the case of 50 MPa with viscosity the linear behaviour of the peak force have some deviation. Such deviation is tracked back from the fact that the peak forces soft and viscous materials depend on both the tip's position and velocity. Moreover, the peak force follows the trend of Hooke's law whenever the peak force value is mostly dependent on the tip's position.

For stiffer materials the effect of viscosity does not vary the slope of the peak force as a function of k . However, softer materials present non neglectable differences of slope from the viscous to the non-viscous cases when representing $F_{peak}(k)$.

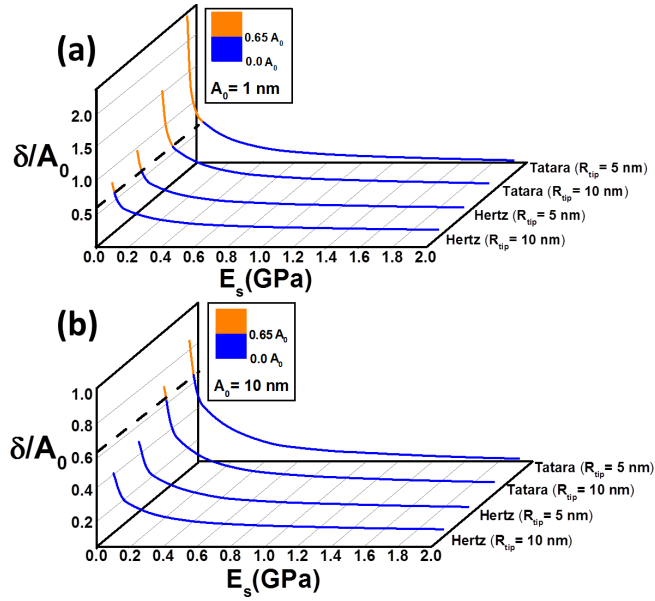


Figure 4.4: Normalized indentation as a function of the sample's Young moduli for Hertz and Tatara's models. The indentation was normalized to the set-point amplitude: (a) $A_0=1$ nm and (b) $A_0=10$ nm. Data above the dashed line indicates that the whole oscillation is performed in contact to the material. Simulation inputs: $k=0.1$ N/m, $f_0=25$ kHz, $Q=2$, $A_{sp}=0.65A_0$, $R_s=4$ nm and two different tip radii 5 and 10 nm. In this simulations no DLVO interactions have been considered.

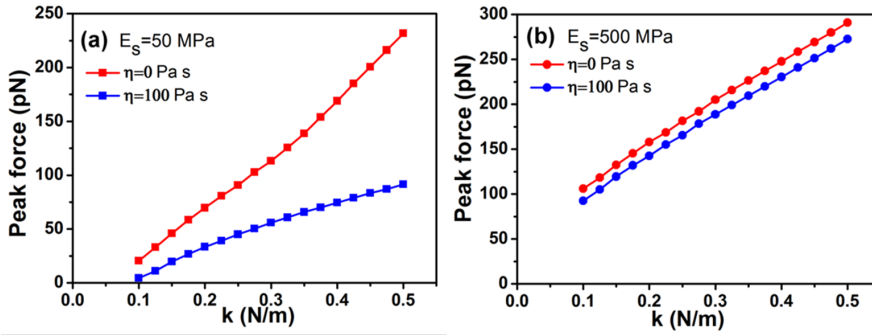


Figure 4.5: Dependence of the peak force with the force constant. Contact mechanics by Tataru.(a) $E_s=50$ MPa and $\eta_s=0$ and 100 Pa.s and (b) $E_s=500$ MPa and $\eta_s=0$ and 100 Pa.s. Contact mechanics are given by Tataru. Simulation data, $k=0.2$ N/m, $f_0=25$ kHz, $Q=2$, $A_0=1$ nm, $A_{sp}=0.9 A_0$, $R_t=5$ nm and $R_s=4$ nm.

4.5 Interplay between operational conditions, the peak forces and soft matter mechanical properties

Three dimensional plots of the dependence of the peak force with both the force constant and the free amplitude provide a summary of the operational conditions required to acquire images at a given peak force (see figure 4.6). They could also provide guidelines to achieve low forces in an experiment. The plots illustrate the requirement of using small amplitudes to reduce the force. Specifically, a peak force of 75 pN requires the use of a free amplitude below 2 nm. It is interesting to note that the introduction of viscoelasticity slightly enlarges the operational space (represented by the surface) in all the axes of figure 4.6(b). For example, the free amplitude goes from 1.8 nm (elastic) to 2.9 nm ($\eta_s=100$ Pa.s) ($A_{sp}=0.95A_0$). However, the peak force reduction due to a viscoelastic response maybe misleading because the viscous force could also introduce some irreversible deformations.

In the presence of a viscoelastic response, the average energy supplied by the external excitation to the cantilever E_{ext} must be equal to the energy dissipated in the water by hydrodynamic forces E_{med} and in the sample [145] E_{dis} ,

$$E_{ext} = E_{med} + E_{dis} \quad (4.2)$$

the mechanical energy transferred from the tip to the sample is divided between the elastic deformation (peak force) and the dissipation associated with the viscous force. For example, for $k=0.1$ N/m, $A_0=2.5$ nm, $A_{sp}=0.9 A_0$, $Q=2$ and $\eta_s=100$ Pa.s we obtain $E_{med}=4.96$ eV, $E_{ext}=5.49$ eV while the energy dissipated in sample is 0.51

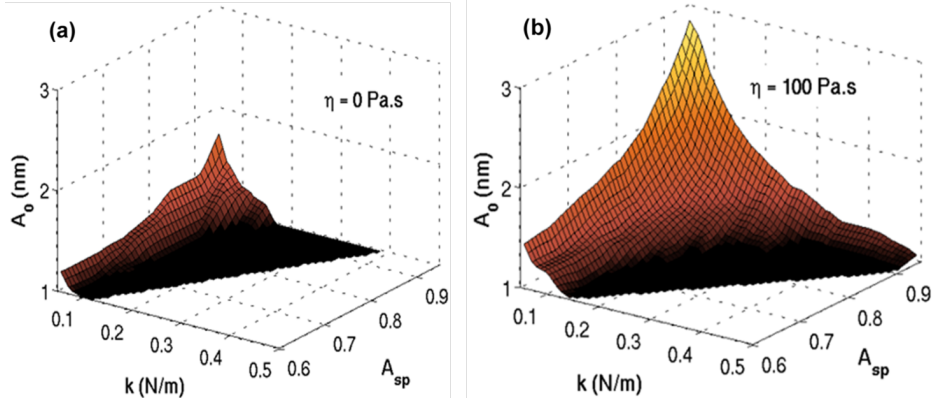


Figure 4.6: Three-dimensional maps of the dynamic AFM operational parameters that establish a given peak force (here 75 pN) for a material with a Young modulus of $E_s=50$ MPa. (a) Elastic. (b) $\eta_s=100$ Pa.s. Simulation data, $f_0=25$ kHz, $Q=2$, $R_t=5$ nm and $R_s=4$ nm. Contact mechanics by Tataru.

eV. The value of E_{dis} is smaller than the maximum potential energy stored in the tip ($E_p = 0.5kA_{sp}^2=1.58$ eV), however, it could imply some damage in molecular resolution measurements.

4.6 High-resolution imaging of molecular process and antibodies

4.6.1 Force estimation of molecular process imaging

High resolution imaging of biomolecular process at high speed represents one of the more recent and exciting developments of force microscopy [164, 165, 15]. Ideally those measurements should be performed at very low forces to minimize sample damage and to avoid external perturbations. In those experiments the forces were estimated by using an expression derived from Hooke's law,

$$F_{peak} = \frac{k(A_0 - A_{sp})}{Q} \quad (4.3)$$

The above expression is not appropriate for two reasons. First it does not include any dependence on the material properties. Second, it underestimates the values of the peak forces by at least a factor 3. For example it gives a value of 20 pN ($k=0.1$ N/m, $A_0=2$ nm, $A_{sp}=0.9 A_0$, $Q=1$) while the simulations give 87 pN and 141 pN, respectively,

E_s (MPa)	F_{peak} (pN)			
	$A_0=1$ nm		$A_0=2$ nm	
	$Q=1$	$Q=2$	$Q=1$	$Q=2$
50	24	7	87	43
75	42	18	119	67
100	55	27	141	85
200	89	59	197	127
300	108	75	231	150
400	122	85	256	168
500	132	92	278	184

Table 4.1: Peak force as a function of E_s , A_0 and Q ($k=0.1$ N/m, $f_0=25$ kHz, $A_{sp}=0.9A_0$, $R_t=5$ nm and $R_s=4$ nm).

for $E_s=50$ and 100 MPa. The Young moduli of small to medium size proteins falls in the 10-100 MPa range. Table 4.1 summarizes the peak forces for some selected Young modulus and operational parameters³.

4.6.2 Molecular resolution images of IgM antibodies in liquid

The framework developed for high resolution imaging conditions studied throughout this Chapter is experimentally illustrated by comparing two topography images of IgM antibodies taken at different free amplitudes with AM-AFM in liquid. Figure 4.7 shows one image of an immunoglobulin M (IgM) pentamer on a mica surface. The molecular resolution image show the five subunits surrounding the central structure (J-chain) as the model extracted from [166](see figure 4.7(b)) whereby IgM pentamers fall within the soft sample regime *i.e.* in the order of tens of *megapascals* [54, 4].

The experimental results shown in figures 4.8 and 4.9 have been acquired under different oscillation amplitude A_0 , set-point amplitude A_{sp} while sharing further operational parameters constant. The shared operational parameters of figures 4.8 and 4.9 are: SNL-Long probe characterized by the thermal noise method with $k \approx 0.09$ N/m, $f_d=32.07$ kHz, $Q=2.92$ and a phosphate buffered saline (PBS) solution prepared as described in [4]. Figure 4.9(a) shows a topography image of IgM pentamers with $A_0=1.92$ (nm) and a $A_{sp}=0.87A_0$ with its corresponding height distribution (see figure 4.9(b)).

In figure 4.9 the same IgM pentamers imaged previously in figure 4.8(a) have been rescanned by changing the $A_0=3.92$ (nm) and the $A_{sp}=0.93A_0$. The height distribution depicted in figures 4.8(b) and 4.9(b) can be compared with reference to the IgM nominal height of 6 nm [166]. As inferred from the theoretical framework described in this

³This section has been adapted from the Author's publication [81].

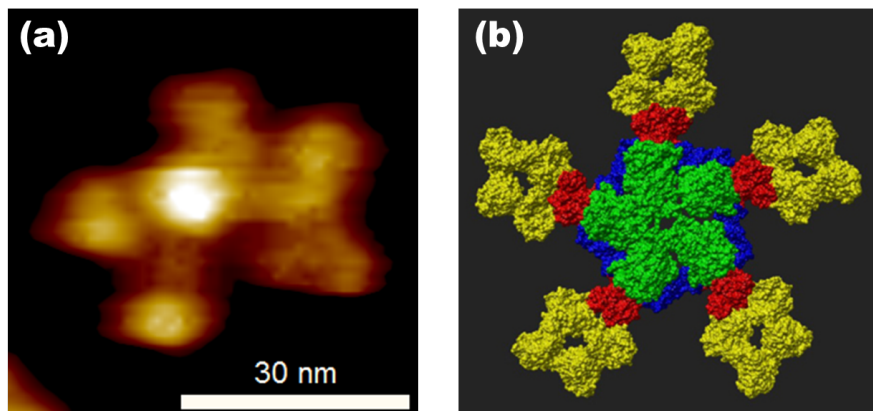


Figure 4.7: (a) Topography image of the IgM pentamer taken in AM-AFM in liquid. (b) Pentamer structure of the IgM antibody [166]. The image was taken in a collaboration with Alma P. Perrino (unpublished results). Experiments by A. P. Perrino and R. Garcia (unpublished results).

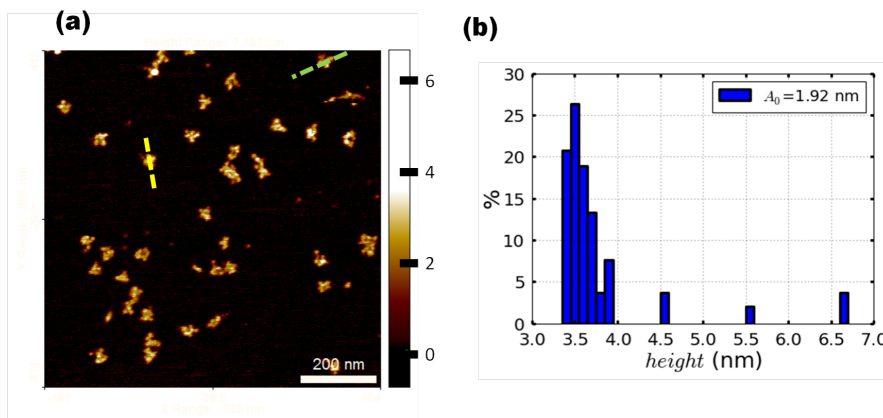


Figure 4.8: (a) Image of several antibody complexes taken in water at $A_0=1.92$ (nm) and $A_{sp}=0.87A_0$ over a muscovite mica surface. (b) Heights distribution of the AM-AFM topography image (the height analysis has been performed using the SPIP software suite [167]). Experiments by A. P. Perrino and R. Garcia (unpublished results).

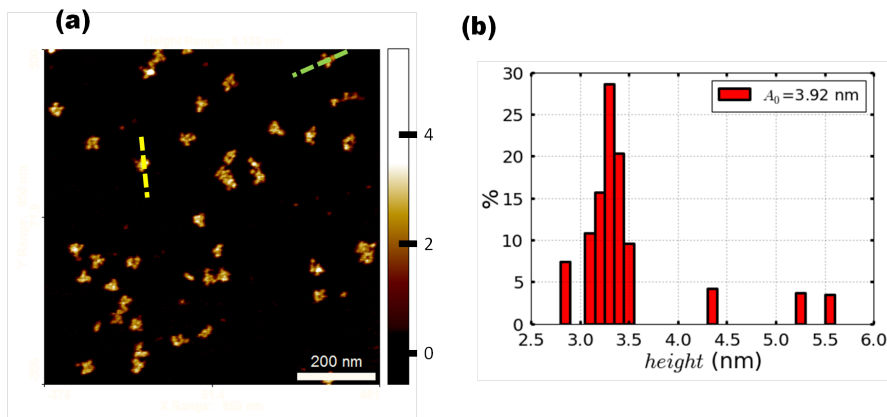


Figure 4.9: (a) Image of several antibody complexes taken in water at $A_0=3.92$ (nm) and $A_{sp}=0.93A_0$ over a muscovite mica surface. (b) Height distribution of the AM-AFM topography image (the height analysis has been performed using the SPIP software suite [167]). Experiments by A. P. Perrino and R. Garcia (unpublished results).

Chapter the height distribution for smaller set-point amplitudes are closer to the sample nominal values.

Furthermore, the height profiles of two isolated IgM pentamers confirm this experimental observation (see figure 4.10).

4.6.3 Conclusions

We have calculated the peak force during the AFM imaging of soft matter in liquid as a function of both sample properties and instrumental parameters. Specifically, we have focused our study on soft materials with Young modulus ranging between 30 and 500 MPa. The mechanical response of the sample has been simulated by using both the standard Hertz contact mechanics and the Tataro model which considers the finite size of the sample. We have calculated three dimensional maps that show the interplay between different operational parameters to image soft matter at small peak forces. Those forces are the ones required to image non-invasively most proteins. The results show marked qualitative and quantitative differences between soft and stiff materials. We summarize main findings: (a) Under the same operational and probe conditions, the peak force depends on the elastic properties of the material. The stiffer the material the larger the peak force. As a consequence images of heterogeneous samples cannot be taken at a constant peak force. (b) A viscoelastic response enables the reduction of the peak force. (c) The amplitude reduction in stiff materials is dominated by the detuning effect. In soft matter, in

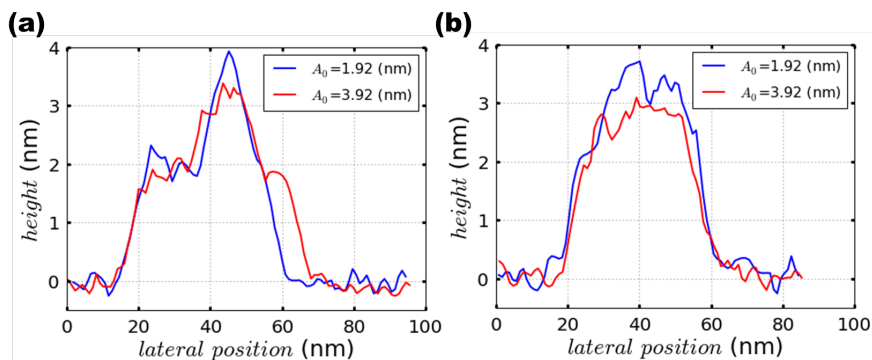


Figure 4.10: Cross sections of two isolated IgM pentamers. (a) Cross section along the green line in the topography images 4.8(blue) and 4.8(red). (b) Cross section along the yellow line in the topography images 4.8(blue) and 4.8(red). The height analysis has been performed using the SPIP software suite [167]. Experiments by A. P. Perrino and R. Garcia (unpublished results).

addition to the above factor the presence of a positive cantilever deflection is a factor that contributes to the amplitude reduction and then to the peak force. (d) Imaging soft matter ($E_s=50$ MPa) at peak forces below 75 pN requires the use of free amplitudes below 2 nm (elastic regime). (e) The contact mechanics model has a significant influence on the estimated force. For soft materials, Tataru model gives peak forces that are a factor two smaller than the forces given by Hertz contact mechanics. Finally, we have compared two topography images of IgM pentamers taken with AM-AFM in liquid at different oscillation amplitudes. It has been observed that the antibodies height recovery could be enhanced by a factor of 11% of the nominal IgM height (6 nm) for smaller oscillation amplitudes. Such observations confirm the interplay between operational imaging conditions and the peak forces of soft materials described along this Chapter.

Chapter 5

Scaling laws to estimate peak forces for soft-matter in liquid

5.1 Introduction to the estimation of the peak forces for soft matter in liquid

The analytical estimation of the peak interaction force between an oscillating microcantilever's tip and soft samples has been a major ambition in AM-AFM. The peak forces of soft and relatively rigid samples have been modeled by performing numerical simulations of the tip motion in liquid. The forces are obtained by using two contact mechanics models: Hertz [94] and Tataru [95]. Here, we derived a closed form parametrized expression to describe the maximum tip-sample interaction forces as a function of the operational conditions of the microscope and the Young moduli of the sample. Such parametrized expression has been obtained by considering a low-Q medium and a repulsive interaction force given by Tataru's contact mechanics model. We also present a comparison between the numerical simulations and four analytical scaling laws for a wide variety of probe and operational parameters, and samples Young moduli. In general, the forces derived from analytical expressions are not in good agreement with the simulations when the Young modulus and the set-point amplitude are varied. The only exceptions are the parametrized approximations that match respectively the numerical results given by Hertz and Tataru's contact mechanics for soft materials, high set-point amplitudes and small free amplitudes.

5.2 Numerical simulations and scaling laws in dynamic AFM

Numerical simulations have supported the development of AM-AFM by predicting several phenomena of the tip motion [79, 38]. Those simulations provide the standards against which new experimental or analytical methods should be compared [168]. In this section the equations of motion of the microcantilever-tip are presented for two models: the point-mass, and a modified Euler-Bernoulli microcantilever beam. Furthermore, three scaling laws used in amplitude modulation AFM are presented as a reference starting point for estimating the peak interaction forces from the operational parameters and the mechanical properties of the sample. In what follows, two different types of oscillation amplitudes are denoted as *small* ($A_0 < 1.5$ nm) and correspondingly *higher oscillation amplitudes* ($1.5 \text{ nm} \leq A_0 \leq 10 \text{ nm}$)¹.

5.2.1 Solving the microcantilever-tip equations of motion

In AM-AFM the equation of motion for the microcantilever-tip system is described as a first approximation by the point-mass model [79],

$$m\ddot{z}(t) = -kz(t) - \gamma\dot{z}(t) + F_{exc}(t) + F_{ts}[z_c + z(t), \dot{z}(t)] \quad (5.1)$$

where m is the effective cantilever mass that includes the added mass of the fluid, ω_0 , Q , k and F_{ts} are respectively, the angular resonant frequency, quality factor, spring constant and tip-sample interaction forces (as previously described in Chapter 2). The point-mass model is suitable if the contribution of higher modes to the cantilever motion is negligible [169, 170]. This could be the case in liquids for small free amplitudes, say below 1.5 nm where the anharmonicity effect is meant to be negligible (see figure 5.1) [171]. Whereby anharmonicity is defined as: $H_n = \sum_{i>1} \frac{A(\omega=i\omega_0)}{A_{sp}}$ with $A(\omega = i\omega_0)$ the oscillation amplitudes of the i th higher harmonics [171]. At higher amplitudes, the tip-surface force generates higher harmonic components, which could lead to the momentary excitation of higher eigenmodes, in particular the second eigenmode [172]. To account for those effects we also describe the microcantilever-tip system by using an extended Euler-Bernoulli equation [43] (as previously described in Chapter 2). This model considers the cantilever as a continuous and uniform rectangular beam under the action of external forces,

¹This section has been adapted from the Author's publication [121].

$$\begin{aligned}
 EI \frac{\partial^4}{\partial x^4} \left[w(x, t) + a_1 \frac{\partial w(x, t)}{\partial t} \right] + \rho_c W h \frac{\partial^2 w(x, t)}{\partial t^2} = \\
 -a_0 \frac{\partial w(x, t)}{\partial t} + \delta(x - L) \left[F_{exc}(w(x, t), x, t) + F_{ts}(d, \dot{d}) \right] \quad (5.2)
 \end{aligned}$$

where E is the Young modulus of the cantilever, I the area moment of inertia, a_1 the internal damping coefficient, ρ the mass density; W , h and L are, respectively, the width, height and length of the cantilever; a_0 is the hydrodynamic damping; $w(x, t)$ is the time dependent vertical displacement of the differential element of the beam placed at the x position, and F_{ts} tip-sample interaction force.

Equations 5.1 and 5.2 are numerically solved by the methods described in Chapter 2. One should note that the use of equations 5.1 and 5.2 in low Q environments are valid for directly excited cantilevers, such as magnetic [20, 21, 22] or photothermal excitations [23, 173].

5.2.2 Preliminary comparison of simulated and analytical peak force values: Dependence on the Young modulus and the set-point amplitude

The simulated contact mechanics models considered for a peak forces comparison are Hertz [94] and Tataru [95]. Figure 5.2 shows a period of the tip oscillation and the corresponding force. The peak force is defined as the maximum force point in the dashed line curves. The curves show a purely repulsive interaction which starts as soon as the mechanical contact is established. The tip-sample interface according to Tataru (5.2(a)) or Hertz (5.2(b)) is also shown. Both contact mechanics models have been applied to describe the response of soft (50 MPa) and relatively rigid (2 GPa) surfaces. Appendix 2, shows the instantaneous force for a variable set-point amplitude.

On the other hand, Hu and Raman [74], Kowalewski and Legleiter [75], and Rodriguez and Garcia [76] have derived some analytical scaling laws to determine the interaction forces in AM-AFM. Hu and Raman parametrized the peak repulsive force by using a nonlinear asymptotic theory [174] and Hertzian mechanics,

$$F_{par} = 2^{1/8} \left(\frac{\pi^3}{3} \right)^{1/4} \left[\frac{k^3}{Q^3} E_{eff} \sqrt{R_t} \right]^{1/4} (A_{sp} A_0^2 - A_{sp}^3)^{3/8} \quad (5.3)$$

Equation 5.3 has been originally derived for high Q environments ($Q > 100$) [74]. Recently, the authors have extended its application to estimate the peak forces exerted over viral capsids in liquid [175]. Rodriguez and Garcia, by using the virial-dissipation method [70, 42, 43], deduced the following expression for the mean value of the force during an oscillation,

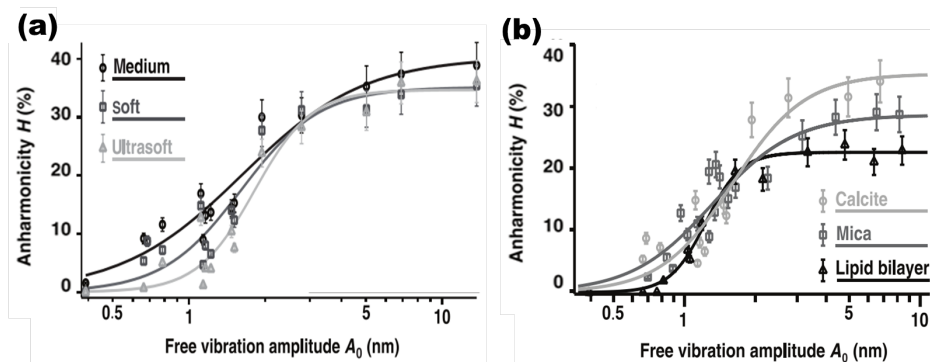


Figure 5.1: The anharmonicity effect measured with AM-AFM. (a) For calcite measurements, the free amplitudes are in the 1-10 nm range and three set-point amplitudes can be distinguished as: ultrasoft $A_{sp}=0.95A_0$ (light gray curve), soft $A_{sp}=0.85A_0$ (gray curve) and medium $A_{sp}=0.75A_0$ (black curve). An abrupt increase in anharmonicity is visible for $A_0 > 1.5$ nm regardless of the imaging conditions used, although lower set-point amplitudes tend to yield higher anharmonicity. The differences between imaging conditions are less marked for larger A_0 . This is due to the large anharmonicities making it difficult to fully control the amplitude at the fundamental frequency. (b) Evolution of anharmonicity as a function of A_0 for all three solids under soft-imaging conditions ($A_{sp}=0.85A_0$). In this case the color scales denote the three different materials, namely: Calcite (light gray curve), Mica (gray curve) and Lipid Bilayer (black curve). The image has been adapted from [171].

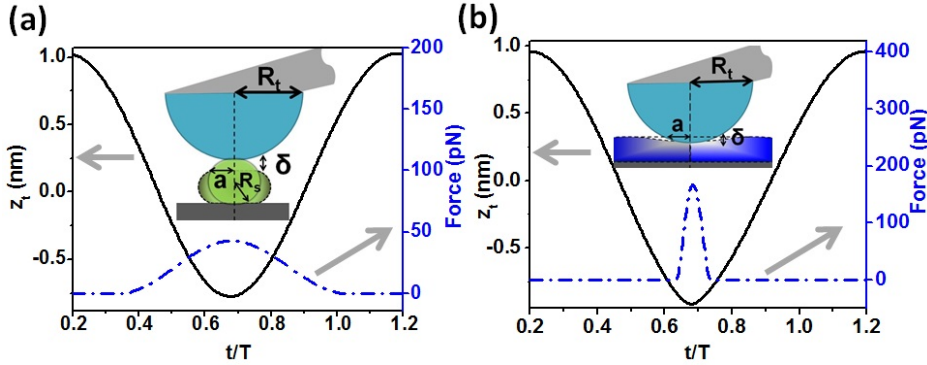


Figure 5.2: Peak forces, tip motion and contact time for two materials. (a) Soft sample ($E_s=50$ MPa) simulated with Tataru's interaction force (see equation 2.59). (b) Rigid sample ($E_s=2$ GPa) simulated with the Hertzian interaction force (see equation 2.38). Simulation inputs: $k=0.1$ N/m, $f_0=25$ kHz, $Q=2$, $A_0=1$ nm, $R_t=5$ nm, $R_s=4$ nm and $A_{sp}=0.9 A_0$.

$$F_{average} = \frac{kA_0}{2Q} \left[1 - \left(\frac{A_{sp}}{A_0} \right)^2 \right]^{1/2} \quad (5.4)$$

In the absence of long-range attractive forces this expression can provide an estimation of the peak force.

Kowalewski and Legleiter proposed an extension of the Hooke law to determine the force in AM-AFM [75]. In this expression, the force depends linearly on the amplitude reduction,

$$F_{linear} = \frac{k(A_0 - A_{sp})}{2Q} \quad (5.5)$$

Figure 5.3 shows a comparison between the analytical expressions 5.3, 5.4, 5.5 and the numerical results for the Hertz model. The comparison covers a Young moduli range between 30 and 2000 MPa. Hu and Raman parametrized force matches the numerical results derived from Hertz in some conditions. The parametrized model estimates the peak forces within a 10% of error for small amplitudes and $A_{sp}=0.9 A_0$. On the other hand, for higher oscillation amplitudes the force is underestimated with a maximum deviation of 16%. The linear and average expressions fail to capture the trend of the numerical simulations because those expressions have exclusively been deduced from the dynamic properties of the tip motion that do not consider any dependence on the material properties of the sample.

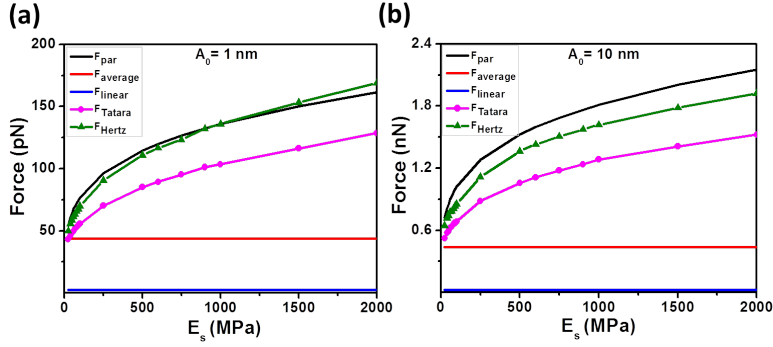


Figure 5.3: Peak force dependence on the sample's Young modulus for different numerical simulations (Hertz and Tatara) and force approximations (parametrized, average and linear). (a) $A_0 = 1$ nm, $R_t = 5$ nm and (b) $A_0 = 10$ nm, $R_t = 5$ nm. Additional simulation inputs are: $k = 0.1$ N/m, $f_0 = 25$ kHz, $Q = 2$, $R_s = 4$ nm and $A_{sp} = 0.9 A_0$.

In figure 5.4, the reduction of A_{sp} in the range between $0.95A_0$ and $0.65A_0$ produces an increase of the peak force. This trend is reported by all the approximations and simulations. However, the linear approximation gives values that are smaller by a factor between 5 and 100 compared with the numerical simulations. As a consequence, the linear approximation should not be used to estimate the peak force in AM-AFM. The average model provides a good qualitative agreement to the Hertz model for soft materials (30-50 MPa) and closer values to the Tatara numerical simulations. However, it fails to reproduce the data for stiffer surfaces. The average model gives the mean value of the forces, attractive and repulsive, acting on the tip during an oscillation period. Consequently, whenever the forces change significantly with the distance (stiff materials) this approximation fails to give a good estimation of the peak force. The parametrized model gives a good numerical description of the peak forces derived from the Hertz model for soft materials and small free amplitudes.

As described previously in Chapter 4, the numerical simulations performed with Tatara model give smaller peak force values than those obtained with Hertzian mechanics [176, 81].

5.3 Free amplitudes and lateral resolution at small peak forces

Imaging at high-spatial resolution demands a compromise between probe, operational parameters and sample properties. Figure 5.5 shows the lateral resolution as given by

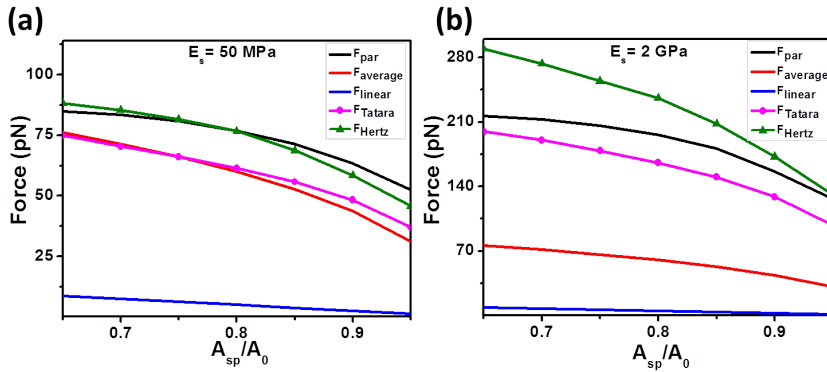


Figure 5.4: Dependence of the peak force on the set-point amplitude for different numerical simulations (Hertz and Tatara) and force approximations (parametrized, average and linear). (a) $A_0 = 1$ nm and $E_s = 50$ MPa. (b) $A_0 = 1$ nm and $E_s = 2$ GPa. Additional simulation inputs are: $k = 0.1$ N/m, $f_0 = 25$ kHz, $Q = 2$, $R_t = 5$ nm and $R_s = 4$ nm.

Hertz and Tatara models for two materials, respectively, $E_s = 50$ MPa and 2 GPa. The lateral resolution is defined as the contact diameter between tip and sample (see figure 5.5). In figure 5.5 we visualize the interplay between the free oscillation and set-point amplitudes with the lateral resolution and peak forces. For a fixed A_{sp}/A_0 ratio the contact diameter increases with A_0 which reduces the lateral resolution. Lowering the A_{sp}/A_0 ratio in the 0.65-0.95 range also reduces the lateral resolution. In any situation the Tatara model renders better lateral resolution than the Hertz model. This result can be traced back to the observation that for the same operational conditions and probe values, Tatara model gives lower peak forces than Hertz model. The lateral resolution also depends on the elastic response of the sample. As a general rule, the stiffer the sample the better the lateral resolution. Sub-nanometric resolution can be achieved by using small A_0 and maintaining a relatively high A_{sp}/A_0 ratio for soft and rigid materials. In some special situations, low A_{sp}/A_0 ratios also provide high resolution. As it has been reported experimentally in [177, 168]. We note that for soft materials ($E_s = 50$ MPa) and in the best case scenario (Tatara model) a lateral resolution below 1 nm could only be reached by using a free amplitude below 0.6 nm. We have separated the plots into regions, for soft materials (5.5a) a sub-100 pN gentle force value is adopted; while for rigid materials (5.5b) a sub-1 nN reference value is considered².

²This section has been adapted from the Author's publication [121].

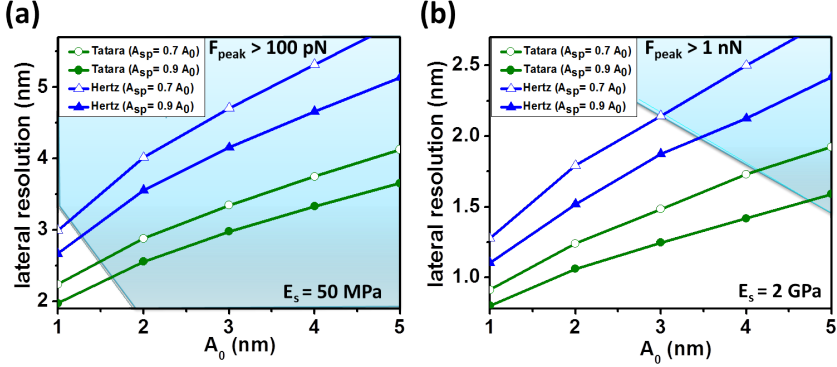


Figure 5.5: Lateral resolution maps for Hertz and Tataro contact mechanics. (a) $E_s = 50$ MPa. (b) $E_s = 2$ GPa. Filled symbols for $A_{sp} = 0.9 A_0$; empty symbols for $A_{sp} = 0.7 A_0$. Circles for Tataro and triangles for Hertz. Simulation inputs: $k = 0.1$ N/m, $f_0 = 25$ kHz, $Q = 2$, $R_t = 5$ nm, $R_s = 4$ nm, and two different A_{sp} , 0.9 and 0.7 A_0 respectively.

5.4 Parametrized expressions to estimate peak forces for soft matter in liquid

In the framework of this thesis, it is of particular interest to provide scaling laws based on both Hertz and Tataro contact mechanical models. These scaling laws could reproduce the salient phenomena of AM-AFM experiments in liquid and its impact on the peak interaction force [76, 178, 75, 74, 179, 81, 121]. To this end, we use the Hertz parametrized expression of Hu and Raman (equation 5.3 [74]) and a new parametrized expression based on Tataro's contact mechanics model. The latter has been explicitly deduced to approximate the peak interaction forces of soft materials characterized by low- Q environments. The new parametrized expression is based on the asymptotic approximation of a 6th-order regression analysis [133, 149] applied to six AFM variables (A_{sp} , A_0 , k , Q , R_{eff} and E_{eff}). These variables turn into a closed form function that is equal to the interaction peak force, *i.e.* $F_{peak} = f(E_{eff}(R_{eff}(Q(k(A_0(A_{sp}))))))$. The solving of this 6th-order function with the regression algorithms of the *scipy optimize curve fit* [180] leads to a parametrized expression given by,

$$F_{Tataro}^{par} = A_0 \left[\left(\frac{24k}{11Q} \right)^{3/4} E_{eff}^{1/4} R_{eff}^{1/4} - \left(\frac{E_{eff} R_{eff}}{2^{11/2}} \right) \right] \left[1 - \left(\frac{A_{sp}}{A_0} \right)^2 \right]^{2/5} \quad (5.6)$$

where A_{sp} is the set-point amplitude of oscillation, A_0 the free amplitude of oscillation, k is the microcantilever spring constant, Q is the quality factor, and E_{eff} , R_{eff}

Case	E_s (MPa)	A_{sp}/A_0	A_0 (nm)	k (N/m)
I	30-300	0.95	1	0.1
II	30-300	0.95	2	0.2
III	30-300	0.95	3	0.3
IV	30-300	0.95	4	0.4
V	60	0.7-0.95	1	0.1
VI	90	0.7-0.95	2	0.2
VII	120	0.7-0.95	3	0.3
VIII	150	0.7-0.95	4	0.4

Table 5.1: Simulations cases to study the accuracy of Hertz and Tatara’s parametrized expressions. For all the cases above the quality factor is 2.

are $1/E_{eff} = (1 - \nu_t^2)/E_t + (1 - \nu_s^2)/E_s$ and $1/R_{eff} = 1/R_t + 1/R_s$. The algorithms used to derive equation 5.6 and the cumulative coefficient of determination of the six variables are further explained in Appendix B. The influence to the peak forces calculated by equation 5.6 are listed in order of relevance: the free oscillation amplitude A_0 and its set-point value A_{sp} , the microcantilever spring constant k and quality factor Q , and the effective tip-sample parameters E_{eff} and R_{eff} . Moreover, this order of importance coincides with the one of equation 5.3 [74]. Note that in equation 5.6 the asymptotic approximations tackle only low-Q environment ($1 \leq Q \leq 5$) and soft samples defined within the range ($30 \text{ MPa} \leq E_s \leq 300 \text{ MPa}$). The upper threshold of E_s has its origin in the second term $E_{eff}R_{eff}/2^{11/2}$ of equation 5.6. Whereby, the first term $\left(\frac{24k}{11Q}\right)^{3/4} E_{eff}^{1/4} R_{eff}^{1/4}$ weight in equation 5.6 must remain higher than the second term.

5.4.1 Probing the accuracy of scaling laws for soft materials in liquid

The scaling laws of equations 5.3 and 5.6 can be used as a tool for experimentalists interested in a quantitative understanding of imaging forces applied to the sample in dynamic AFM operation in liquid. However, a previous step is to determine its accuracy by comparing them with numerical simulations of different operational parameter and sample’s properties. Throughout this section the dependence of the scaling laws on the set-point amplitude and sample’s Young modulus are provided by studying several tip-sample ensembles (summarized in table 5.1).

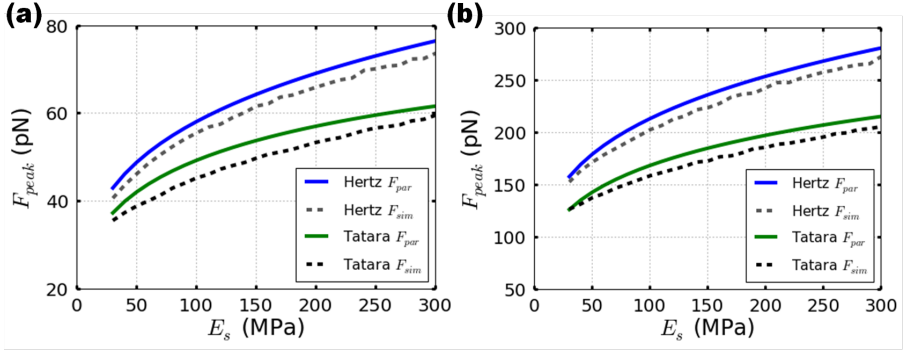


Figure 5.6: Peak forces dependence on the sample Young modulus for the parametrized expressions in equations 5.3 and 5.6 (full line plots) and the corresponding numerical simulations for Hertz and Tatar contact mechanics models (dashed line plots). (a) $A_0=1$ nm and $k=0.1$ N/m, (b) $A_0=2$ nm and $k=0.2$ N/m. Common simulations and calculated parameters are: $E_t=170$ GPa, $E_s=30$ -300 MPa, $A_{sp}=0.95 A_0$, $f_0=25$ kHz, $Q=2$, $R_t=5$ nm and $R_s=4$ nm (Tatar only).

5.4.2 Peak forces dependence on the sample Young modulus

Figures 5.6 and 5.7 show comparisons between the parametrized expressions of equations 5.3 and 5.6 with their corresponding numerical simulations for the Hertz and Tatar's models. The comparison covers a range from 30 to 300 MPa, and a fixed set-point amplitude $A_{sp}=0.95A_0$. In addition, the free oscillation amplitudes of oscillation and spring constants adopt the corresponding values of cases I - IV (see table 5.1). For cases I - IV, the peak forces increase monotonically with the sample's Young modulus. Figure 5.6 represents cases I and II of table 5.1, in both cases the parametrized expressions are in good quantitative agreement with the numerical simulations. The accuracy of both parametrized expressions is within the 10% margin. However, case-II (figure 5.6(b)) presents a better agreement than case-I (figure 5.6(a)). The source of such error can be attributed to the fact that case-I represents the lower boundary conditions of the asymptotic approximation, *i.e.* $A_0=1$ nm and $k=0.1$ N/m of the regression analysis [180].

Figures 5.7(a) and 5.7(b), show the comparisons between the aforementioned equations and the corresponding numerical simulations for Hertz and Tatar corresponding to cases III - IV, respectively. Both figures show a better quantitative agreement for Tatar's parametrized equation than the Hertz' one. Nonetheless, Hertz' and Tatar's comparisons remain within a 10% margin of error.

Furthermore, in cases V - VIII the material Young moduli are fixed and the peak forces are subject to the reduction of A_{sp} (from $0.95A_0$ to $0.7A_0$). In general for soft

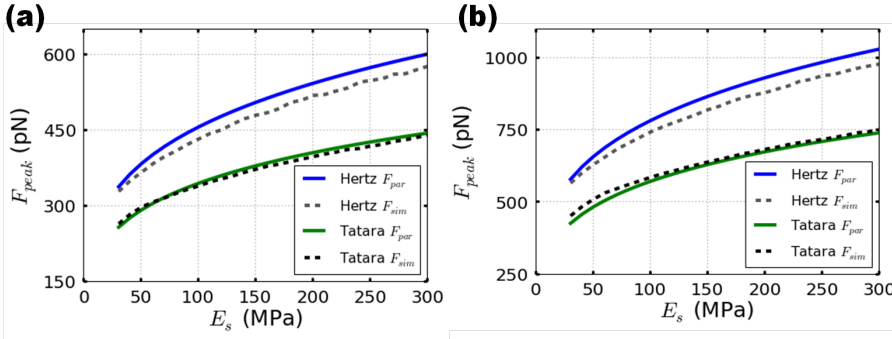


Figure 5.7: Peak forces dependence on the sample Young modulus for the parametrized expressions in equations 5.3 and 5.6 (full line plots) and the corresponding numerical simulations for Hertz and Tatara contact mechanics models (dashed line plots). (a) $A_0=3$ nm and $k=0.3$ N/m, (b) $A_0=4$ nm and $k=0.4$ N/m. Common simulations and calculated parameters are: $E_t=170$ GPa, $E_s=30-300$ MPa, $A_{sp}=0.95 A_0$, $f_0=25$ kHz, $Q=2$, $R_t=5$ nm and $R_s=4$ nm (Tatara only).

material in liquid we have observed (see Chapter 4) that the reduction of A_{sp} produces an increase in the peak force (see figures Figure 5.8 and 5.9). Figure 5.8, reflects cases V - VI where both parametrized expressions enhance their agreement to numerical simulations whenever A_{sp} is increased.

On the other hand, figure 5.9 shows cases VII - VIII where the parametrized model based on Hertzian mechanics has a similar trend to the one explained for figure 5.8. However, Tatara's based parametrized expression for cases VII - VIII minimizes the error with respect to numerical simulations as shown in both figures 5.9(a) and 5.9(b).

The cases described in table 5.1 represent typical imaging conditions of soft samples. However, the new parametrized expression has been further verified for stiffer microcantilever's $k \sim 0.5-5$ N/m (see Appendix 2). It is important to notice that the reduction of A_{sp} has been halted at the value $A_{sp}=0.7 A_0$ since it represents the value where very soft materials start the permanent contact regime of oscillation (as previously shown in Chapter 4).

5.5 Conclusions

Numerical simulations of the tip motion in amplitude modulation AFM enable a comprehensive description of the factors that control the peak force in liquid. We have simulated the peak force for two contact mechanics models, Tatara/Hertz, and we have calculated three analytical approximations, linear, average and parametrized. The linear

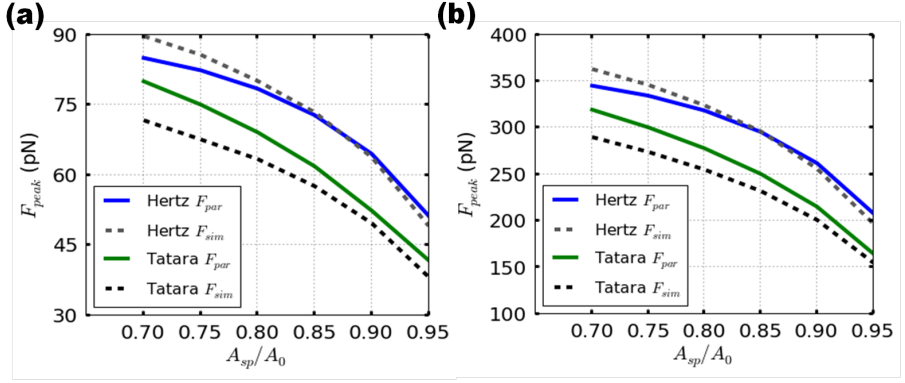


Figure 5.8: Peak forces dependence on the set-point amplitude for the parametrized expressions in equations 5.3 and 5.6 (full line plots) and the corresponding numerical simulations for Hertz and Tatara contact mechanics models (dashed line plots). (a) $A_0=1$ nm, $k=0.1$ N/m and $E_s=60$ MPa (b) $A_0=2$ nm and $k=0.2$ N/m and $E_s=90$ MPa. Common simulation and calculated parameters are: $E_t=170$ GPa, $A_{sp}=0.7 A_0-0.95 A_0$, $f_0=25$ kHz, $Q=2$, $R_t=5$ nm and $R_s=4$ nm (Tatara only).

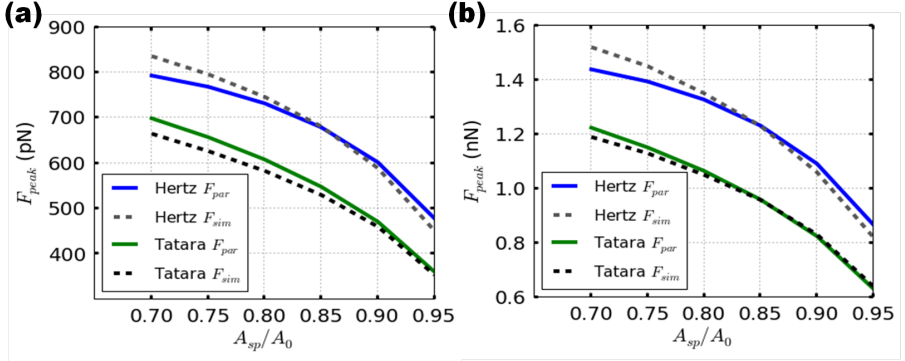


Figure 5.9: Peak forces dependence on the set-point amplitude for the parametrized expressions in equations 5.3 and 5.6 (full line plots) and the corresponding numerical simulations for Hertz and Tatara contact mechanics models (dashed line plots). (a) $A_0=3$ nm, $k=0.3$ N/m and $E_s=120$ MPa (b) $A_0=4$ nm and $k=0.4$ N/m and $E_s=150$ MPa. Common simulation and calculated parameters are: $E_t=170$ GPa, $A_{sp}=0.7 A_0-0.95 A_0$, $f_0=25$ kHz, $Q=2$, $R_t=5$ nm and $R_s=4$ nm (Tatara only).

approximation fails to describe qualitatively and quantitatively the peak forces. The average model captures the peak force behaviour with the operational parameters but the quantitative agreement is poor.

Furthermore, we have derived an analytical expression that reproduces the peak forces of Tataro's contact mechanics for low- Q environments and soft materials. The accuracy of two parametrized models (Hertz and Tataro) has been tested for typical soft materials imaging conditions. Remarkably, both approximations resemble the simulated results given by Hertz and Tataro for soft materials, free amplitudes in the range 1-10 nm, and high set-point amplitudes but its quantitative accuracy decreases by reducing the set-point amplitude. The new parametrized expression for Tataro's contact mechanics provides the experimentalist with a quantitative understanding of the exerted forces while imaging soft matter in dynamic AFM for low- Q environments. In contrast to the previous Hertz' based parametrized expression, the Tataro's one considers a finite sample, consequently adding a degree of freedom to better estimate the peak interaction forces of samples containing small features with finite radii.

The spatial resolution depends on the operational parameters, the elastic response of the sample, the peak force, and the contact mechanics model. The conditions to achieve a high spatial resolution become more demanding for lower Young moduli of the samples. High spatial resolution in liquid requires the use of rather small oscillation amplitudes. Sub-1 nm lateral resolutions for a soft material of a Young modulus of 50 MPa will require the use of free amplitudes of 0.5 nm or less. Lowering the free amplitude of the oscillation improves the lateral resolution in liquid. The resolution increases in line with the Young modulus of the sample, while keeping the operational parameters constant.

The results presented here provide a good estimation of the peak force values experienced by the samples observed with an AFM in liquid. However, the simulations have been performed without considering hydration layers or viscoelastic effects that arise either from the sample or the hydration layer. Those effects could modify the peak force values reported here, although we do not expect significant changes for the data acquired under the conditions for a high spatial resolution (sub-5 nm). Note also that equation 5.6 is an asymptotic approximation which is valid for low- Q environment ($1 \leq Q \leq 5$) and soft samples defined within the range ($30 \text{ MPa} \leq E_s \leq 300 \text{ MPa}$).

Chapter 6

Peak forces in Bimodal AFM

6.1 Introduction

Throughout this chapter, we explore the response of a microcantilever when driven simultaneously at its two first resonance frequencies using the original Bimodal AM technique. The first mode is typically used to obtain the topography image like in AM-AFM. Simultaneously the output of the second eigenmode is driven in an open-loop, namely, the amplitude and the phase shift can be used to map changes in the mechanical, magnetic or electrical properties of the surface (as previously introduced in Chapter 1) [38, 25]. Here, the microcantilever, measurement medium and operational parameters have been chosen such that the tip-sample interactions remain repulsive. In addition to the operational parameters of AM-AFM described earlier (see Chapter 4). Moreover, we focus on the variation of the second mode driven amplitude A_{02} and hence the ratio between the free amplitudes of the first and second eigenmodes A_{01}/A_{02} while A_{sp1} has been set to reach the repulsive interaction regime. The ratio A_{01}/A_{02} has been previously defined for describing Bimodal AM imaging conditions and/or enhancing compositional mapping [44, 181, 182, 37, 183, 177]. Recently, the effect of modulating A_{02} while working in the repulsive regime has been used to reveal subsurface nanoparticles immersed in polymeric films [161]. However, the detected second eigenmode amplitude A_2 carries out different deformations that are not tracked by any feedback mechanism and hence interaction forces which depend on the material properties of the sample, imaging conditions and the coupling between eigenmodes [37, 184]. We study the effect of varying A_{02} (where A_{01} remains constant) to the peak forces by means of numerical simulations based on the contribution of the output amplitudes A_1 and A_2 to the total deformation δ . The results and discussion referenced within this chapter are applicable to soft materials (Young moduli: 30-300 MPa) with relatively small A_{01} and A_{02} (within 10 nm each). Furthermore, the imaging conditions A_{sp1} , E_s , k_1 are varied whereby the

second mode parameters are the ones for a rectangular microcantilever [37]. Despite the embedded complexities and nonlinearities of the technique under low-Q environments [185], we have performed an extensive analysis of numerical simulations of soft materials with different imaging conditions. We show that the peak force in Bimodal AM can be gently modulated by A_{02} rather than using A_{sp1} . These common trends of the peak forces reveal a new mechanism to achieve the imaging with gentle forces. Furthermore, an immediate application of this result is to prevent the abrupt increase of the peak forces which is a consequence of a permanent contact regime while working with soft materials and small amplitudes (see Chapter 4).

6.2 Modeling bimodal force microscopy in liquid

The bimodal driven force (using magnetic or photothermal excitation as explained earlier in Chapter 2) at the free end of the microcantilever ($x = L$) is given by,

$$F_{exc}(x, t) = (F_{01} \cos \omega_{d1}t + F_{02} \cos \omega_{d2}t) \quad (6.1)$$

where $F_{01,02}$ is the magnitude of the force at the excitation frequency $\omega_{d1,d2}$ for the first two eigenmodes of oscillation. The bimodal driven force of equation 6.1 is applied to the modified Euler-Bernoulli equation 2.11 (see Chapter 2). In what follows, we consider a rectangular microcantilever whereby the second eigenmode frequency matches $\omega_{d2}=6.27\omega_{d1}$. The numerical solution of equation 2.11 requires the discretization of the first two eigenmodes of oscillation [42, 43], yielding to the following equations system,

$$m_1 \ddot{z}_1(t) = -\gamma_1 \dot{z}_1(t) - k_1 z_1(t) + F_{01} \cos \omega_{d1}t + F_{02} \cos \omega_{d2}t + F_{ts}(d, \dot{d}) \quad (6.2)$$

$$m_2 \ddot{z}_2(t) = -\gamma_2 \dot{z}_2(t) - k_2 z_2(t) + F_{01} \cos \omega_{d1}t + F_{02} \cos \omega_{d2}t + F_{ts}(d, \dot{d}) \quad (6.3)$$

where $z_{1,2}(t)$ are the instantaneous modal deflections, $m_{1,2}$ the modal masses, $\gamma_{1,2}$ the hydrodynamic damping coefficients and $k_{1,2}$ spring constants of the first and second microcantilevers eigenmodes, respectively. By considering a rectangular cantilever as the one described in Chapter 2, the second eigenmode parameters follows: $k_2=40k_1$ and $Q_2=6.27Q_1$. Assuming that the contributions to the microcantilever from higher eigenmodes (> 2) are not detected, as well as, the higher harmonics contribution, we can solve equations 6.2 and 6.3 by the sum of the first two eigenmodes,

$$w(L, t) \approx A_1 \cos(\omega_1 t - \phi_1) + A_2 \cos(\omega_2 t - \phi_2) \quad (6.4)$$

where $A_{1,2}$ and $\phi_{1,2}$ are the oscillation amplitudes phase shifts of the first two modes of the angular frequencies $\omega_{1,2}$. The bimodal signal temporal dependence in absence of force ($F_{ts}=0$) is shown in figure 6.1(a). Moreover, the presence of a repulsive interaction

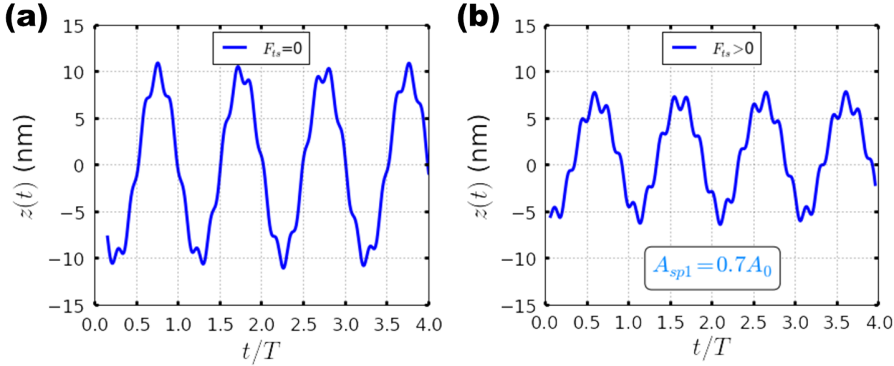


Figure 6.1: (a) Temporal dependency of the microcantilever motion $w(L, t)$ for bimodal AFM in absence of interaction $F_{ts} = 0$. (b) Temporal dependency of the microcantilever motion $w(L, t)$ for bimodal AFM under a repulsive interaction given by Hertzian contact mechanics. Simulation data: $E_s=100$ MPa, $k_1=0.5$ N/m, $k_2=20.0$ N/m, $f_{01}=10.0$ kHz, $f_{02}=62.7$ kHz, $Q_1=4$, $Q_2=25.08$, $A_{01}=10$ nm, $A_{02}=1$ nm, $A_{sp1}=0.7 A_0$ (figure (b) only) and $R_t=5$ nm.

($F_{ts} > 0$) decreases the free oscillating amplitude of the signal from figure 6.1(a) to the one chosen for figure 6.1(b) ($A_{sp1}=0.7 A_{01}$).

The two eigenmodes response described in equation 6.4 ($z_1(t) = A_1 \cos(\omega_1 t - \phi_1)$ and $z_2(t) = A_2 \cos(\omega_2 t - \phi_2)$) are illustrated in figures 6.2(a) and (c). Moreover, the superposition of both $w(L, t)$ determine the total deformation δ applied to the material and hence its time-dependent forces $F_{ts}(t)$ (see figures 6.2(b) and (d)). The instantaneous values of the Bimodal AM force during the contact time of each whole cycle show different patterns which is not the case in AM-AFM (single mode). Notoriously, not even the peak force values of each Bimodal AM steady-state cycle coincide (see figures 6.2(b) and (d)). This phenomena has different origins, on one hand the momentary excitation and relaxation between higher eigenmodes [170, 172, 185]. On the other hand, the non-harmonic behaviour of the two superposed signals $z_1(t)$ and $z_2(t)$ which oscillate at two different frequencies f_{d1} and f_{d2} where the relationship $f_{d2}=6.27 f_{d1}$ assumed is not given by an integer value. In particular, for the simulations parameters of figure 6.2 the oscillation frequencies are $f_{d1}=10$ kHz and $f_{d2}=62.7$ kHz and hence the least common multiple (LCM) is 627. This means that every 627 cycles at f_{d2} the same time-dependent force pattern (in regard to the harmonics superposition) will be repeated for such bimodal signal. By knowing the LCM between the two driven frequencies, we have established the number of cycles to be analyzed to obtain the highest sample deformation produced by the bimodal wave and hence its peak repulsive force over this time

interval. Such value is proposed to be the reference value of the peak Bimodal AM force referred within this Chapter. In addition to the non-harmonic behavior of the Bimodal AM driven signal another phenomena can influence the peak forces such as the momentary excitation of non-driven higher eigenmodes [172], influence of higher harmonics [171, 186] and additional complexities described elsewhere [185].

Figure 6.2 illustrates also the dependence of the interaction force on A_{01} and A_{01}/A_{02} for a fixed A_{02} . The simulated values for figure 6.2 correspond to $A_{01}=10$ nm, $A_{01}/A_{02}=10$ (6.2(a) and (b)) and $A_{01}=5$ nm, $A_{01}/A_{02}=5$ (6.2(c) and (d)).

6.3 Backbone aspects of Bimodal AM force microscopy in liquid

The ratio of free amplitudes has been previously investigated to further understand the relationship with the phase and amplitude contrast of the Bimodal AFM technique [44, 181, 182, 187, 37, 185]. Recently, Ebeling and Solares have systematically performed experiments to study the imaging conditions required for enhancing resolution over mica surfaces [177]. Moreover, Gigler *et al.* [183] investigated bimodal imaging of polymers in the repulsive mode suggesting that the free amplitudes ratio deviates from the originally proposed for enhancing the phase contrast in the air [37]. This section also provides an introduction to the input/output amplitude ratios definition in Bimodal AFM.

6.3.1 Experimental Bimodal AM in liquid

Solares and Ebeling presented a systematic study of high-resolution imaging capabilities of Bimodal AM in liquid [177]. To this end they quantified the height and phase corrugation of mica surfaces from a batch of 64 images using different free amplitudes (A_{01} and A_{02}) and set-point amplitudes (see figure 6.3). They also concluded that better images of stiff samples are achieved by decreasing the second eigenmode amplitude A_{02} (as permitted instrumentally) and keeping the amplitudes ratio $A_{01}/A_{02} > 1$.

On the other hand, Gigler *et al.* [183] suggested that for bimodal imaging on polymers the amplitudes ratio shall remain $A_{01}/A_{02} \leq 10$. From both articles [183, 177], we have extracted the amplitudes ratios used along this Chapter ($1 \leq A_{01}/A_{02} \leq 10$) whereby we focus on soft materials ($30 \text{ MPa} \leq E_s \leq 300 \text{ MPa}$) in liquid environment ($Q_1=4$).

6.3.2 Peak forces in Bimodal AM force microscopy

The input amplitudes ratio in Bimodal AM (bimodal amplitudes ratio) is defined as,

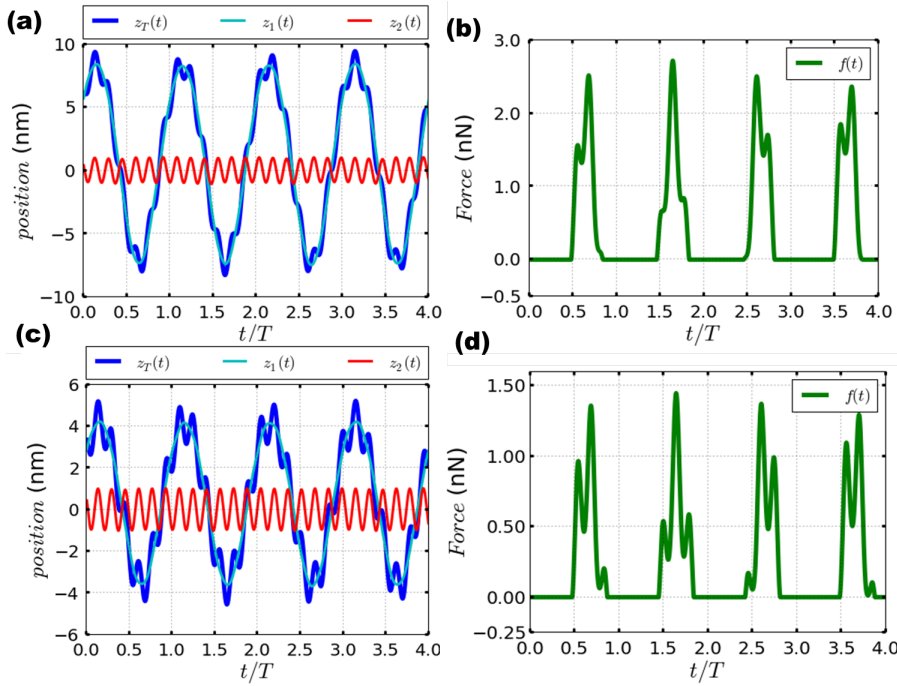


Figure 6.2: Temporal dependency of the microcantilever motion $w(L, t)$ ($z_T(t)$) for bimodal AM. Separating the superposed signals of: $z_1(t)$ and $z_2(t)$. (a) The free amplitude of the first mode correspond to $A_{01}=10$ nm and the free amplitude of the second mode $A_{02}=1$ nm resulting in $A_{01}/A_{02}=10$. (b) The time dependent forces for the bimodal signal are calculated by the Hertzian contact mechanics. (c) The free amplitude of the first mode correspond to $A_{01}=5$ nm and the free amplitude of the second mode $A_{02}=1$ nm resulting in $A_{01}/A_{02}=5$. (d) The time dependent forces from the bimodal signal shown in (c) are calculated by the Hertzian contact mechanics. Common simulation data: $E_s=100$ MPa, $k_1=0.5$ N/m, $k_2=20.0$ N/m, $f_{01}=10.0$ kHz, $f_{02}=62.7$ kHz, $Q_1=4$, $Q_2=25.08$, $A_{sp}=0.9 A_0$ and $R_t=5$ nm.

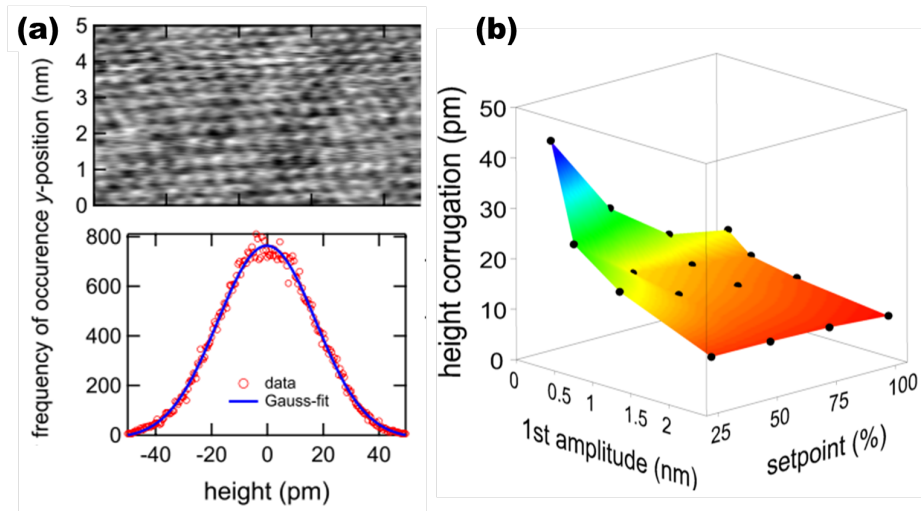


Figure 6.3: (a) Illustration of the analysis steps performed to quantify the height corrugation. Top row: FFT filtered mica bimodal images for a $A_{01}/A_{02}=2$. Bottom row: histograms of the corresponding images with Gaussian fits. (b) Surface map of the height corrugation dependence on both A_{01} and A_{sp1} whereby $A_2=0.3$ (nm) (plotted from experimental results). Adapted from [177].

$$A_{ratio}^i = \frac{A_{01}}{A_{02}} \quad (6.5)$$

where A_{01} is the free amplitude of the first mode and A_{02} the second one. The input amplitudes ratio is not conserved at the output since it depends on the mechanical properties of the sample. Hence we define,

$$A_{ratio}^o = \frac{A_{sp1}}{A_2} \quad (6.6)$$

where A_{sp1} is the set-point amplitude value, A_2 is the maximum output oscillation amplitude of the second eigenmode. Note that the value of A_2 referred within this Chapter is the maximum output oscillation since A_2 can be subject to relaxation between successive tip-sample impacts [185]. Then, the minimum distance between tip and sample can be defined as,

$$d_{min} = z_c - A_{sp1} - A_2 \quad (6.7)$$

where z_c is the average tip-sample distance. Note that the minimum distance will correspond to the maximum deformation ($\delta = a_0 - d_{min}$) whenever the tip-sample interactions are conservative (in this case elastic). Non-conservative tip-sample interactions ($F_{nc} = f(\dot{d}(t), \ddot{d}(t), \dots)$) do not follow the bidirectional relationship between F_{peak} and d_{min} . As described earlier in Chapter 3 and 4, the peak force let us determine the degree of invasiveness on the sample and hence its image resolution [81, 121]. In figure 6.4 a comparison of peak repulsive interactions in Bimodal AM and AM-AFM (single mode) as a function of the set-point amplitude is provided. To address this comparison we have assumed the following condition $A_0 = A_{01}$ for the calculation of the peak forces in single and Bimodal AM. In the latter, the signal superposes the first and second eigenmodes oscillation 6.1 where the total amplitude increases and hence the peak force does (see figure 6.4). It is important to remark that in an alternative assumption for comparing these forces is to consider $A_0 = A_{01} + A_{02}$ whereby this peak forces in Bimodal AM are not necessarily higher than the single modal ones. Most importantly, figure 6.4(a,c) and figures 6.4(b,d) show how the peak force modulation in bimodal AM takes place by means of A_{02} and A_{sp1} simultaneously.

Furthermore, figure 6.5 shows the single and bimodal amplitudes as a function of the tip-sample average distance z_c . Clearly, the tip-sample interaction in Bimodal AM AFM depends on the prescribed ratio A_{01}/A_{02} . Hence, the first eigenmode amplitude interaction begins before the common AM-AFM case. The biggest the ratio the smaller the difference between the single (figure 6.5(a)) and bimodal (figure 6.5(b)) cases.

Note that figure 6.5(b) shows also that a given set-point amplitude in Bimodal AM will be reached at a larger z_c distances than in single mode operation and presumably for the same set-point amplitude lower deformation are reached ($\delta = z_c + z(t)$).

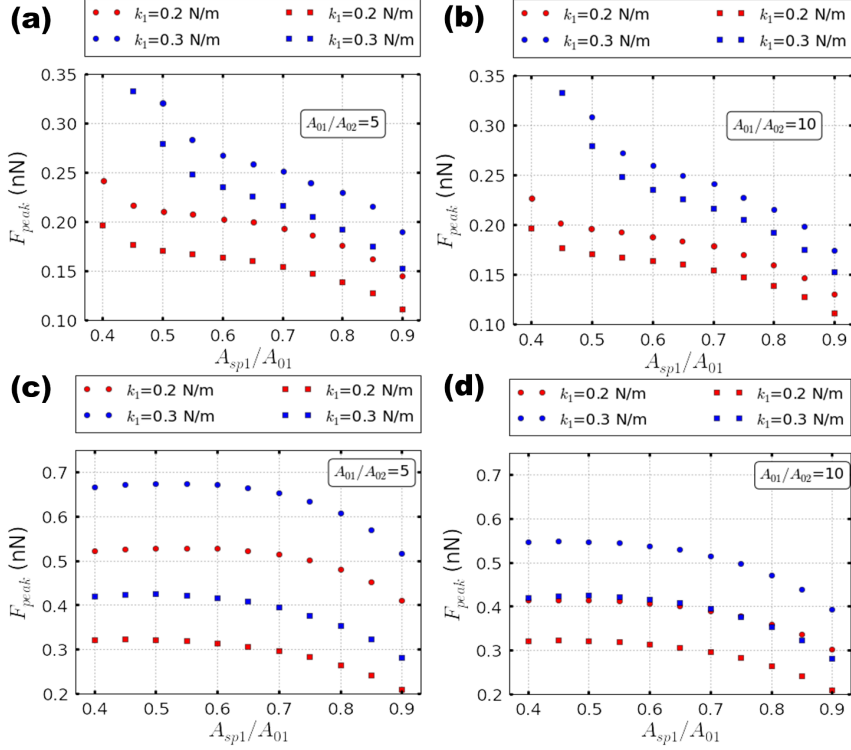


Figure 6.4: Comparison of the peak interaction forces of single and Bimodal AM AFM as a function of the set-point amplitude of the first mode for two different samples Young moduli : $E_s=30$ MPa and $E_s=300$ MPa. (a) Depicts the peak forces for $A_{01}/A_{02} = 5$ and $E_s=30$ MPa. (b) Depicts the peak forces for $A_{01}/A_{02} = 10$ and $E_s=30$ MPa. (c) Depicts the peak forces for $A_{01}/A_{02} = 5$ and $E_s=300$ MPa. (d) Depicts the peak forces for $A_{01}/A_{02} = 10$ and $E_s=300$ MPa. In all cases, the square symbols represent the single mode values while the Bimodal AM ones are symbolized with circles. Common simulation data: $f_{01}=10.0$ kHz, $f_{02}=62.7$ kHz, $Q_1=4$, $Q_2=25.08$, A_0 and $A_{01}=2$ nm, $R_t=5$ nm and two values for the cantilever spring constant: colored in red ($k_1=0.2$ N/m, $k_2=8.0$ N/m) and colored in blue ($k_1=0.3$ N/m, $k_2=12.0$ N/m).

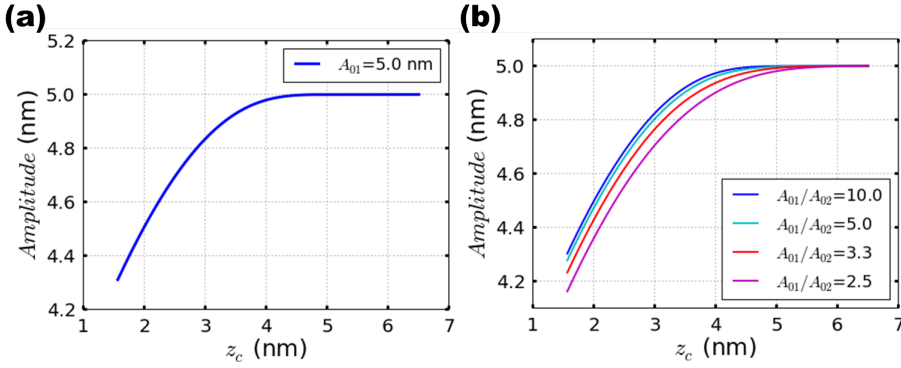


Figure 6.5: Amplitude dependence on z_c . (a) AM-AFM (single-mode) repulsive interaction. (b) Bimodal AM interactions within a range of variable input amplitudes ratios: $A_{01}/A_{02} = 10$ (blue curve), $A_{01}/A_{02} = 5$ (cyan curve), $A_{01}/A_{02} = 3.3$ (red curve) and $A_{01}/A_{02} = 2.5$ (magenta curve). Simulation data: $E_s = 60$ MPa, $k_1 = 0.5$ N/m, $k_2 = 20.0$ N/m, $f_{01} = 10.0$ kHz, $f_{02} = 62.7$ kHz, $Q_1 = 4$, $Q_2 = 25.08$, A_0 and $A_{01} = 5$ nm and $R_t = 5$ nm. The first eigenmode parameters coincide with the AM-AFM ones (Figure (a)).

6.4 Bimodal AFM interplay of the peak interaction forces with k_1 , A_{01} and E_s

Although several studies have been devoted to the input amplitudes ratio and energy ratios in bimodal and multifrequency AFM [181, 188, 183, 37, 185], the interplay of the output amplitudes ratio with the imaging conditions has been only experimentally studied for stiff samples (Mica) [177]. Here, we assume values for the input amplitudes ratio to obtain the maximum output amplitude of the second mode A_2 whereby the amplitude of the first mode is set to A_{sp1} within a specific range of soft materials and imaging conditions summarized in Table 6.1. By analyzing a sufficient amount of oscillation cycles from the Bimodal signal (using the LCM criteria, described previously) the corresponding peak forces have been extracted. Such value depends on the variation of the second mode amplitude due to the material elastic properties (some authors call this behaviour material contrast [188]). Nonetheless, samples with inhomogeneous stiffness in the Z -axis could give rise to perturbations across the surface where a quantitative interpretation of material contrast may become meaningless. The contribution of those perturbations typically follows the trend: the stiffer the material, thus more perturbations in the cantilever oscillation. Here, we address this issue by performing quantitative comparisons for different samples ($30 \text{ MPa} < E_s < 300 \text{ MPa}$) and its operational parameters sensitivity (see Table 6.1). On the other hand, it is important to remark that

Parameters	E_s (MPa)	A_{01} (nm)	k_1 (N/m)	A_{sp1}	A_{02}
Ranges	30-300	3, 5, 7, 10	0.1-0.5	$(0.4-0.9)A_{01}$	$\in (1 \text{ nm}, A_{01})$
Steps	27	4	10	11	—

Table 6.1: Simulations ranges for figures 6.6, 6.7, 6.8 and 6.9.

the energy relation of the first to the second eigenmodes in the cases $A_{01}/A_{02}=10$ and 7 fulfills $E_{02} < E_{01}$ while for the smallest $A_{01}/A_{02}=5$ and 3 it is $E_{02} > E_{01}$. The energy values of the bimodal channels are calculated by $E_{01,02} = 0.5k_{01,02}A_{01,02}^2$ [188]. Note also that the range of operational parameters have been chosen to improve imaging resolution by following previous results shown in Chapter 4 and 5 for AM-AFM.

Figures 6.6, 6.7, 6.8 and 6.9 show contour plots of different oscillation amplitudes, A_{02} varies within the range $(1 \text{ nm}, A_{01})$ and A_{01} is fixed whereby the dependence of the cantilever spring constant k_1 (proportionally $k_2=40 k_1$) is also shown. Moreover, figures 6.6-6.7 correspond to a material with a Young modulus of $E_s=30$ MPa and figures 6.8-6.9 to a stiffer material where $E_s=300$ MPa. In addition, the corresponding fixed values of A_{01} are embedded in each contour plot (see figures 6.6, 6.7, 6.8 and 6.9).

In figure 6.6, four contour plots are shown where the two on the left depict the peak force values for the set-point amplitude $A_{sp1}=0.85 A_{01}$ and the other two on the right side $A_{sp1}=0.65 A_{01}$. Figures 6.6, 6.7, 6.8 and 6.9 share the same panel order of the contour plots with regard to the set-point amplitude. The first trend that can be extracted from the aforementioned figures is that if A_{sp1} decreases from $0.85A_{01}$ to $0.65A_{01}$ the peak forces increase. Another general observation is that the peak interaction is decreased whenever the value of A_{01} decreases (assuming that the permanent contact regime has not been reached). Back to figure 6.6, the upper plots (figure 6.6(a) and (b)) show an expected trend of the cantilever as its stiffness increases the material contrast¹ also improves. However, by decreasing A_{01} to 7 nm this trend is not followed and the highest peak force value in figure 6.6(c) do not correspond to the highest cantilever stiffness (upper right corner in figures 6.6 (a), (b) and (d)). Such behaviour has been also found in figures 6.7 and 6.8. Note that soft cantilevers in low-Q environments could lead to the momentary excitation of higher-eigenmodes [170, 172]. Nonetheless, this phenomenon could be circumvented by increasing the value of k_1 . Moreover, this result coincide in some phenomenon of Bimodal AM that have been previously described [37, 188, 185].

In figure 6.7 we have set a peak force threshold to 1 nN (dashed line in yellow) and hence analyze the relevance of varying A_{02} to the peak forces modulation. The peak forces are sensitive to A_{02} , as illustrated in figures 6.6, 6.7, 6.8 and 6.9. Moreover, using the peak force threshold and projecting its value to A_{02} within a gap of 1 nm to a higher

¹Note that a higher material contrast refers to the increase of A_2 which leads to an increase of the total deformation and hence the peak force.

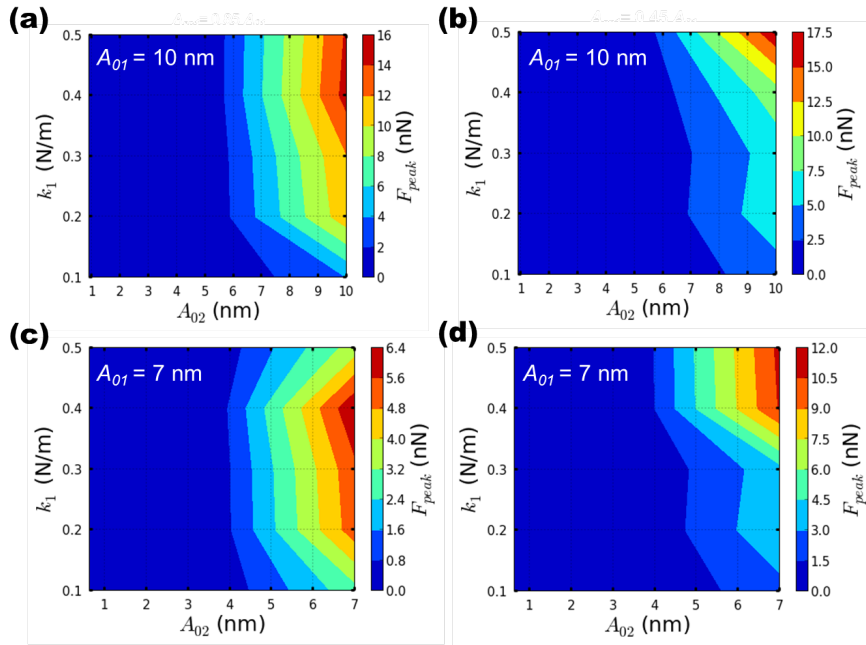


Figure 6.6: Contour plots of the peak forces as a function of the spring constant k_1 and the second mode free amplitude A_{02} . Top row: the first mode free amplitude value is $A_{01}=10$ nm with (a) $A_{sp1}=0.85 A_{01}$ and (b) $A_{sp1}=0.65$. Bottom row: the first mode free amplitude value is $A_{01}=7$ nm with (c) $A_{sp1}=0.85 A_{01}$ and (d) $A_{sp1}=0.65$. Common simulation parameters $E_s=30$ MPa, $Q_1=4$, $Q_2=25.08$, $f_{01}=10$ kHz, $f_{02}=62.7$ kHz, k_2 varies according to the relationship $k_1=40k_2$.

ΔA_{sp1} (nm)	A_{02} range (nm)	ΔA_{02} (nm)	F_{peak} range (nN)	ΔF_{peak} (nN)	Fig.
1	3.2-4.2	1	1.0-2.3	1.3	6.7(a)
	2.85-3.85	1	1.0-5.0	4.0	6.7(b)
0.6	2.0-3.0	1	1.0-2.8	1.8	6.7(c)
	1.9-2.9	1	1.0-4.0	3.0	6.7(d)

Table 6.2: Force modulated values as a function of ΔA_{sp1} and ΔA_{02} according to figure 6.7.

ΔA_{sp1} (nm)	A_{02} range (nm)	ΔA_{02} (nm)	F_{peak} range (nN)	ΔF_{peak} (nN)	Fig.
1.0	3.2-3.9	0.7	3.0-4.0	1.0	6.9(a)
	3.3-4.0	0.7	3.0-6.0	3.0	6.9(b)
0.6	2.7-3.0	0.3	2.8-3.2	0.4	6.9(c)
	2.5-2.8	0.3	3.0-4.2	1.2	6.9(d)

Table 6.3: Force modulated values as a function of ΔA_{sp1} and ΔA_{02} according to figure 6.9.

value of A_{02} the ranges of forces can be modulated. However, this force modulation values depend also on the imaging conditions *i.e.* A_{01} , A_{sp1} and k_1 . Interestingly, the decrease of A_{sp1} have a stronger influence on the peak forces than the variation of A_{02} (within a given set point amplitude A_{sp1} as summarized in table 6.2). Table 6.2 summarizes the peak forces variations for a $\Delta A_{02}=1$ nm and $\Delta A_{sp1}=0.6$ nm as extracted from figure 6.7.

Note also that the values of ΔF_{peak} of table 6.2 are not chosen for optimizing resolution but for showing the Bimodal AM force modulation method.

Figures 6.8 and 6.9 describe a stiffer sample ($E_s=300$ MPa) sharing the same imaging conditions described earlier for figures 6.6 and 6.7. As expected the peak forces increase with stiffer material Young modulus. On the other hand, we expect that by decreasing the material's Young moduli in one order of magnitude the effect of A_{02} on the peak force values will be also decreased.

Notoriously, from table 6.3 we can infer that ΔF_{peak} decreases for smaller A_{01} and higher A_{sp1} which coincides with the observation of the softer material (as shown in table 6.2). In the cases illustrated in figure 6.9, the F_{peak} threshold is 3 nN and the A_{02} gap is 0.5 nm and 0.2 nm for $A_{01}=5$ and 3 nm, respectively.

The values given in table 6.3 also show that the sensitivity of F_{peak}/A_{02} can remain constant for different A_{01} but are very sensitive to A_{sp1} (as detailed in rows 1, 3 and 2, 4 of the same table). This results underlines the need of an insightful computational

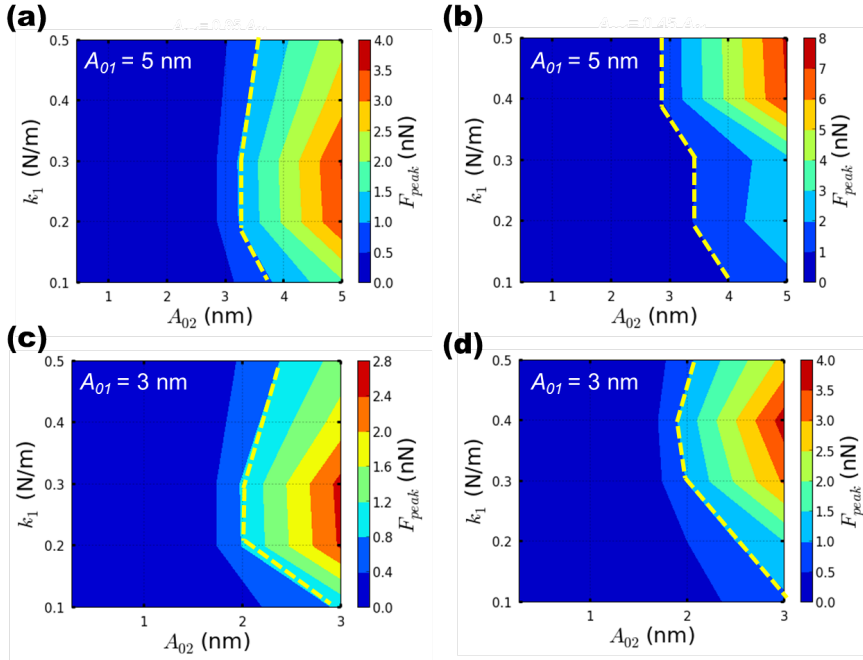


Figure 6.7: Contour plots of the peak forces as a function of the spring constant k_1 and the second mode free amplitude A_{02} . Top row: the first mode free amplitude value is $A_{01}=5$ nm with (a) $A_{sp1}=0.85 A_{01}$ and (b) $A_{sp1}=0.65$. Bottom row: the first mode free amplitude value is $A_{01}=3$ nm with (c) $A_{sp1}=0.85 A_{01}$ and (d) $A_{sp1}=0.65$. The yellow dashed line denotes the peak force threshold $F_{peak}=1$ nN. Common simulation parameters $E_s=30$ MPa, $Q_1=4$, $Q_2=25.08$, $f_{01}=10$ kHz, $f_{02}=62.7$ kHz, k_2 varies according to the relationship $k_1=40k_2$.

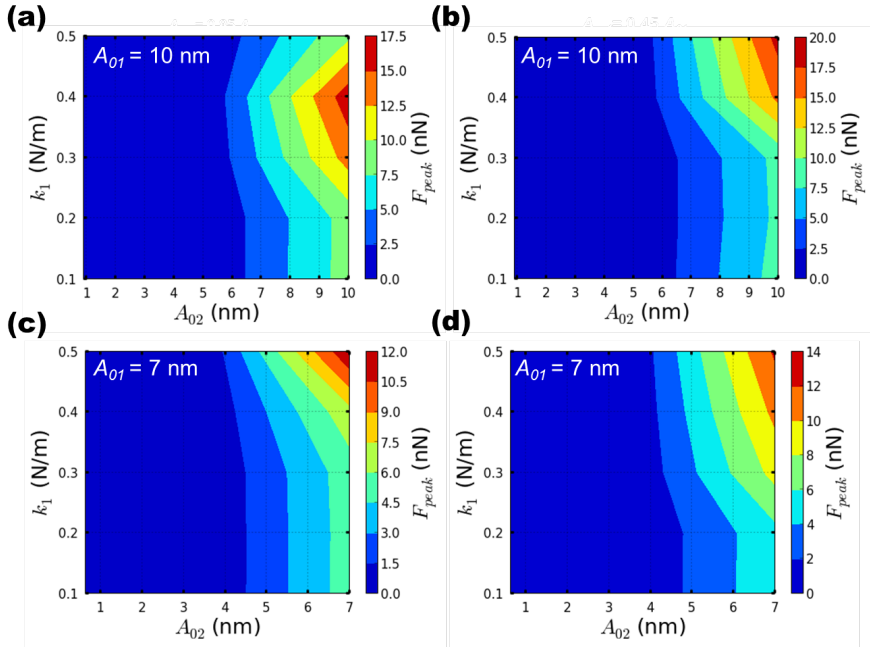


Figure 6.8: Contour plots of the peak forces as a function of the spring constant k_1 and the second mode free amplitude A_{02} . Top row: the first mode free amplitude value is $A_{01}=10$ nm with (a) $A_{sp1}=0.85 A_{01}$ and (b) $A_{sp1}=0.65$. Bottom row: the first mode free amplitude value is $A_{01}=7$ nm with (c) $A_{sp1}=0.85 A_{01}$ and (d) $A_{sp1}=0.65$. Common simulations parameters $E_s=300$ MPa, $Q_1=4$, $Q_2=25.08$, $f_{01}=10$ kHz, $f_{02}=62.7$ kHz, k_2 varies according to the relationship $k_1=40k_2$.

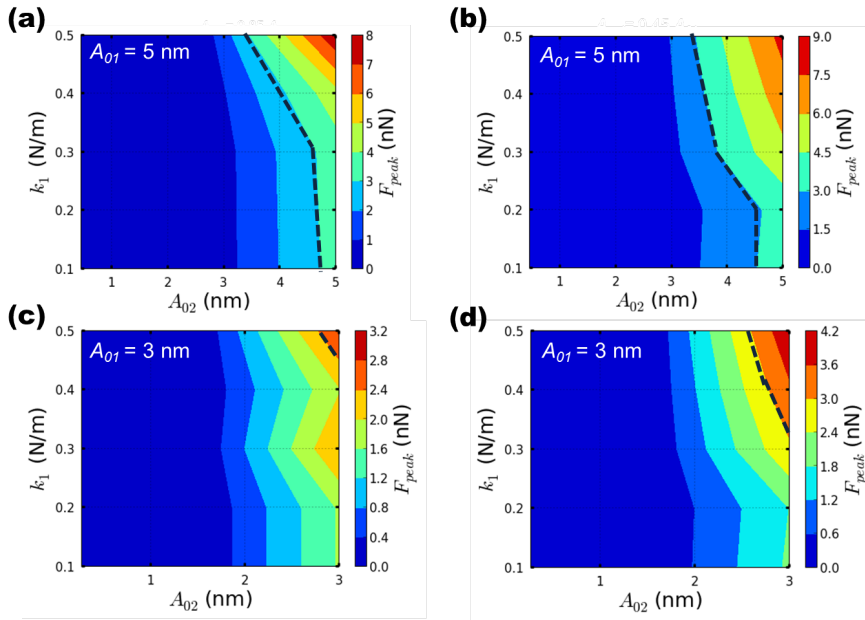


Figure 6.9: Contour plots of the peak forces as a function of the spring constant k_1 and the second mode free amplitude A_{02} . Top row: the first mode free amplitude value is $A_{01}=5$ nm with (a) $A_{sp1}=0.85 A_{01}$ and (b) $A_{sp1}=0.65$. Bottom row: the first mode free amplitude value is $A_{01}=3$ nm with (c) $A_{sp1}=0.85 A_{01}$ and (d) $A_{sp1}=0.65$. The black dashed line denotes the peak force threshold $F_{peak} = 1$ nN. Common simulations parameters $E_s=300$ MPa, $Q_1=4$, $Q_2=25.08$, $f_{01}=10$ kHz, $f_{02}=62.7$ kHz, k_2 varies according to the relationship $k_1=40k_2$.

analysis of the Bimodal AM imaging conditions and also envisages a new method to increase/decrease the peak forces (on demand) with a less sensitive parameter than A_{sp1} .

6.5 Conclusions

In this Chapter the influence of different imaging conditions on the relationship between A_{02} and the Bimodal AM peak forces have been studied for soft and elastic materials (Young moduli: 30 - 300 MPa). The output value of the second mode amplitude A_2 depends on several parameters such as in the single modal case but added complexities are observed while trying to generalize the results under low-Q Bimodal AM operation. Such complexities depend on both input and output amplitudes ratios, the non-harmonic behaviour of the bimodal signal and on the stiffness of the cantilever and Young modulus of the sample that lead to coupled interaction of the driven and even the non-driven eigenmodes [188, 185]. Despite the challenge encountered, we have implemented an extensive computational analysis to track the highest value of the peak force for each simulated case. Our calculations on the range of imaging and sample parameters described in table 6.1 lead us to two main conclusions. First, the second mode amplitude A_{02} modulates the peak forces in a more gentle scale since its sensitivity to the peak forces is less than the one for A_{sp1} . Second, we have verified that observations made to the single modal case (AM-AFM) are valid for Bimodal AM since for smaller A_{01} and higher A_{sp1} the peak forces decrease whereby the permanent contact regime has not been reached. The first and main conclusion of this chapter is that the second mode amplitude A_{02} can be used to track the topographical imaging conditions within a gentle threshold of peak forces. Such gentle threshold of peak forces underlines the fact that the peak forces variation within the same range of *nanometers* for A_{02} is smaller than the one for A_{sp1} whereby the materials are soft and elastic. The proposed Bimodal AM peak forces analysis verifies the recently suggested *indentation control* by higher eigenmodes in multifrequency AFM [161], but it also provides an starting point by analyzing the case of soft materials with relatively small amplitudes (A_{01} and A_{02} within 10 nm). The results presented here provide a good estimation of the peak force values experienced by the materials described earlier. However, there is an open discussion regarding the combination of higher modes excitation and frequency dependent forces such as viscoelasticity that could lead to different operation regimes [188]. Those effects could modify the peak force values reported here, although we expect significant changes may arise only for very soft materials with a high viscosity coefficient due to its sensitivity on the deformation rates.

Chapter 7

Conclusions

7.1 Conclusions

1. We have calculated the peak force during the AFM imaging of soft matter in liquid as a function of both sample properties and instrumental parameters. Specifically, we have focused our study on soft materials with Young modulus ranging between 30 and 500 MPa. The mechanical response of the sample has been simulated by using both the standard Hertz contact mechanics and the Tatara model which considers the finite size of the sample. We have calculated three dimensional maps that show the interplay between different operational parameters to image soft matter at small peak forces. Those forces are the ones required to image non-invasively most proteins. The results show marked qualitative and quantitative differences between soft and stiff materials. We summarize main findings: *(a)* Under the same operational and probe conditions, the peak force depends on the elastic properties of the material. The stiffer the material the larger the peak force. As a consequence images of heterogeneous samples cannot be taken at a constant peak force. *(b)* A viscoelastic response enables the reduction of the peak force. *(c)* The amplitude reduction in stiff materials is dominated by the detuning effect. In soft matter, in addition to the above factor the presence of a positive cantilever deflection is a factor that contributes to the amplitude reduction and then to the peak force. *(d)* Imaging soft matter ($E_s=50$ MPa) at peak forces below 75 pN requires the use of free amplitudes below 2 nm (elastic regime). *(e)* The contact mechanics model has a significant influence on the estimated force. For soft materials, Tatara model gives peak forces that are a factor two smaller than the forces given by Hertz contact mechanics. Finally, we have compared two topography images of IgM pentamers taken with AM-AFM in liquid at different oscillation amplitudes. It has been observed that the antibodies height recovery could be enhanced by a

factor of 11% of the nominal IgM height (6 nm) for smaller oscillation amplitudes. Such observations confirm the interplay between operational imaging conditions and the peak forces of soft materials described along the Chapter 4.

2. We have derived an analytical expression that reproduces the peak forces of Tataro's contact mechanics for low-Q environments and soft materials. The accuracy of two parametrized models (Hertz and Tataro) has been tested for typical soft materials imaging conditions. Remarkably, both approximations resemble the simulated results given by Hertz and Tataro for soft materials, free amplitudes in the range 1-10 nm, and high set-point amplitudes but its quantitative accuracy decreases by reducing the set-point amplitude. The new parametrized expression for Tataro's contact mechanics provides the experimentalist with a quantitative understanding of the exerted forces while imaging soft matter in dynamic AFM for low-Q environments. In contrast to the previous Hertz' based parametrized expression, the Tataro's one considers a finite sample, consequently adding a degree of freedom to better estimate the peak interaction forces of samples containing small features with finite radii.
3. The spatial resolution depends on the operational parameters, the elastic response of the sample, the peak force, and the contact mechanics model. The conditions to achieve a high spatial resolution become more demanding for lower Young moduli of the samples. High spatial resolution in liquid requires the use of rather small oscillation amplitudes. Sub-1 nm lateral resolutions for a soft material of a Young modulus of 50 MPa will require the use of free amplitudes of 0.5 nm or less. The resolution increases in line with the Young modulus of the sample, while keeping the operational parameters constant.
4. In bimodal AM, the output value of the second mode amplitude A_2 depends on several parameters such as in the single modal case but added complexities are observed while trying to generalize the results under low-Q Bimodal AM operation. Such complexities depend on both input and output amplitudes ratios, the non-harmonic behaviour of the bimodal signal and on the stiffness of the cantilever and Young modulus of the sample that lead to coupled interaction of the driven and even the non-driven eigenmodes. Despite the challenge encountered, we have implemented an extensive computational analysis to track the highest value of the peak force for each simulated case. Our calculations on the range of imaging and sample parameters described in table 6.1 lead us to two main conclusions. First, the second mode amplitude A_{02} modulates the peak forces in a more gentle scale since its sensitivity to the peak forces is less than the one for A_{sp1} . Second, we have verified that observations made to the single modal case (AM-AFM) are valid for Bimodal AM since for smaller A_{01} and higher A_{sp1} the peak forces decrease whereby the permanent contact regime has not been reached.

5. A method has been proposed to recover the peak viscoelastic force in AM-AFM by using two spring-dashpot models, namely, the Kelvin-Voigt's (KV) and Standard Linear Solid (SLS) models. This method relies on three dynamic AFM variables: A_{sp} , ϕ and t_c for a prescribed deformation to the sample. For both models KV and SLS, the results show that the method matches the numerical simulations results over a combined range of low driving frequencies f_d where the material relaxation and instrumental timescales follows $\tau \sim t_c$ and low set-point amplitudes $A_{sp} \sim 0.4 A_0$. However, the latter criteria could be extended to higher amplitudes at expense of a decrease in the viscosity of the soft material. Whereby the soft material timescales depend on the viscosity coefficient ν .
6. The force for viscoelastic samples comprises both conservative (F_{sto}) and dissipative (F_{loss}) interactions which show a strong dependence on the deformation δ and $\dot{\delta}$, respectively. At high frequencies $t_c > \tau$ (with $t_c = 1/f_c$ and the relation $f_c > f_d$ is fulfilled) the viscous interactions ($f(\dot{\delta})$) could be dominant over elastic interactions ($f(\delta)$) whereby AM-AFM observables are required to provide an accurate value for $\dot{\delta}$ which at the same time demands a time-resolved signal from the measurement.
7. An interactive scientific computing tool for understanding dynamic force microscopy experiments has been provided. The dynamic AFM simulator (dForce) is a powerful code devoted to the numerical solution of two types of non-linear differential equations, namely, the point-mass (single-frequency) and the modified Euler-Bernoulli (multifrequency AFM) models. In addition it includes over 10 different tip-sample force models. This code has been also designed and developed within this thesis.

7.2 Conclusiones

1. Se han calculado las fuerzas pico durante la toma de imágenes de materiales blandos en líquidos como una función de las propiedades de la muestra y las del microscopio. El enfoque de dicho estudio son materiales blandos entre los 30 y 500 MPa de módulo de Young. La respuesta mecánica se ha simulado usando dos modelos de contacto: Hertz y Tataru. Este último incluye las deformaciones tanto verticales como laterales de la muestra y considera que la muestra tiene dimensiones finitas. Dentro del análisis computacional realizado se calculan mapas en tres dimensiones que muestran las combinaciones de parámetros operacionales del microscopio (amplitudes A_0 , A_{sp} y la constante de fuerzas k) necesarios para obtener imágenes de materiales blandos aplicando fuerzas pico muy pequeñas. Dichas fuerzas son las necesarias para la toma de imágenes de gran parte de proteínas medidas con AM-AFM de manera no-invasiva. Los resultados muestran diferencias cuantitativas y cualitativas entre materiales blandos y relativamente rígidos. Nuestros hallazgos se pueden resumir de la siguiente manera: (a) Bajo las mismas condiciones de la palanca y operativas del microscopio, la fuerza pico depende de las propiedades elásticas del material. Mientras éste sea más rígido por tanto se obtendrá una mayor fuerza pico. En consecuencia las imágenes de muestras heterogéneas no pueden ser tomadas a una fuerza pico constante. (b) La respuesta viscoelástica del material resulta en una reducción de la fuerza pico. (c) En materiales rígidos, la reducción de la amplitud se puede explicar mediante el efecto de no sintonización (o *detuning effect*). Por su parte los materiales blandos, además de dicho *detuning effect* se pudo notar la contribución de una deflexión positiva de la palanca a medida que decrece la amplitud. Así mismo dicha deflexión se debe considerar en el cálculo de la fuerza pico. (d) Para la toma de imágenes de material blando ($E_s=50$ MPa) con fuerzas pico por debajo de 75 pN se requiere usar una amplitud de oscilación menor que 2 nm (dentro del régimen elástico). (e) Los modelos de mecánica de contacto influyen en la fuerza pico estimada. Para los materiales blandos antes descritos, el modelo de Tataru resulta en fuerzas menores que el modelo de Hertz por un factor dos. Por último se han comparado dos imágenes de topografía de los anticuerpos IgM con AM-AFM en líquidos y con diferentes amplitudes de oscilación. Las observaciones de dicho experimento muestran que la altura de los anticuerpos tiene una mejora en un 11% de su altura nominal (6 nm) mediante el uso de amplitudes menores (del orden de 1 nm). Dichas observaciones coinciden con los entregables de fuerzas pico y resolución lateral para materiales blandos descritos en el capítulo 4.
2. Se ha derivado una expresión analítica para reproducir las fuerzas pico (basadas en el modelo de contacto de Tataru) para materiales blandos en medio líquido. Así mismo se ha comprobado la exactitud de los modelos paramétricos de Hertz y Tataru mediante simulaciones numéricas. Específicamente, dentro de las condi-

ciones necesarias para tomar imágenes de materiales blandos a fuerzas pico pequeñas se han probado amplitudes libres entre 1-10 nm y amplitudes de trabajo altas. Por otra parte se ha observado que ambas expresiones incrementan su error respecto a las simulaciones cuando amplitud de trabajo disminuye. La nueva expresión paramétrica para el modelo de Tatara ofrece a los científicos experimentales un entendimiento cuantitativo de las fuerzas máximas ejercidas mientras se toma una imagen. Adicionalmente, el modelo de Tatara considera una muestra finita y por tanto se añade un grado de libertad durante la estimación de dichas fuerzas pico.

3. La resolución espacial depende de los siguientes parámetros operacionales: la respuesta elástica de la muestra, la fuerza pico y el modelo de mecánica de contacto considerado. Las condiciones para conseguir una buena resolución espacial se tornan muchos más exigentes para materiales con módulos de Young pequeños. En líquidos una buena resolución espacial se conseguirá reduciendo la amplitud de oscilación. En concreto para obtener una resolución sub-1 nm en una muestra de 50 MPa de módulo de Young se requerirá una amplitud de oscilación estimada de 0.5 nm o aún menor. La resolución se incrementa en línea con el módulo de Young de la muestra, siempre y cuando se mantengan los parámetros operacionales constantes.
4. En la microscopía Bimodal AM, el valor de amplitud del segundo modo A_2 depende de varios parámetros como es el caso de la microscopía monomodal, sin embargo, existe mayor complejidad cuando uno intenta generalizar dichos resultados en especial para medios con Q – bajos. Dicha complejidad depende de varios factores: las proporciones de amplitudes de entrada y salida de los modos bimodales, el comportamiento no-armónico de la señal bimodal, de la constante de fuerzas de la micropalanca y de las propiedades del material que conllevan acoplamientos de los modos excitados e incluso de otros modos superiores no excitados. A pesar de dicha complejidad se ha realizado un análisis computacional para obtener los valores de la fuerza pico de interacción para cada caso (según la descripción hecha en la tabla 6.1). Los resultados de dicho análisis llevan a dos conclusiones principales. La primera que la modulación de las fuerzas pico se puede hacer de una forma más suave utilizando la variable A_{02} en lugar de usar A_{sp1} . La segunda conclusión es que hemos podido verificar que ciertas observaciones hechas en monomodal (AM-AFM) son válidas para el caso bimodal AM cuando A_{01} se reduce y A_{sp1} se incrementan entonces las fuerzas pico decrecen (criterio válido mientras la interacción no se encuentre en el régimen de contacto permanente).
5. Se ha presentado un método para recuperar la fuerza pico viscoelástica en AM-AFM, utilizando dos modelos de *springs-dashpot*: el de Kelvin-Voigt (KV) y el

Standard Linear Solid (SLS). Este método se basa en 3 variables de AFM en modo dinámico: A_{sp} , ϕ y t_c dada una deformación prescrita de la muestra. En ambos casos KV y SLS, los resultados obtenidos muestran que el método recupera la fuerza pico viscoelástica cuando se combina una frecuencia de excitación f_d (donde la siguiente relación entre el material y el instrumento $\tau \sim t_c$ se cumpla) y una amplitud de trabajo baja $A_{sp} \sim 0.4 A_0$. Sin embargo, el rango de validez de dicho método podría extenderse a medida que el coeficiente de viscosidad ν en el material blando decrece.

6. Las fuerzas de tipo viscoelástico están compuestas por dos elementos: interacciones conservativas (F_{sto}) y disipativas (F_{loss}) que a su vez tienen una dependencia directa con la deformación δ y la tasa de deformación $\dot{\delta}$, respectivamente. Para altas frecuencias $t_c > \tau$ (con $t_c = 1/f_c$ y $f_c > f_d$) las interacciones viscosas ($f(\dot{\delta})$) pueden ser dominantes sobre las de carácter elástico ($f(\delta)$). Este escenario demanda una detección de la señal de interacción $\dot{\delta}$ a ser resuelta en el dominio del tiempo.
7. Se ha diseñado, desarrollado e implementado una plataforma de cálculo científico para entender los experimentos de la microscopía de fuerzas en modo dinámico. El simulador de AFM dinámico (dForce) es un código enfocado a la solución numérica de dos tipos de ecuaciones diferenciales no-lineales a través de dos modelos: el de masa puntual (monomodal) y el de Euler-Bernoulli modificado (multimodal). Así mismo se incluyen más de 10 modelos de fuerza para la interacción entre punta y muestra.

Appendix A

Interactive platform for understanding force microscopy experiments

A.1 Introduction

Dynamic atomic force microscopy (dAFM) is a powerful technique that is capable of imaging material surfaces with nanometer resolution in air, liquid or vacuum environments. These features have awakened the interest of many researchers in the multidisciplinary field of nanotechnology to enhance the technique resolution and the identification/quantification of material properties, among others. However, those enhancements could be accompanied with an increasing complexity in the interpretation and understanding of the intrinsic phenomena in the dynamics of the tip motion and its different tip-sample interactions. Moreover, advanced dAFM techniques such as the multifrequency ones are new developments that can be less intuitive than single-frequency ones. For a more insightful interpretation of single and multifrequency dynamic AFM tip-sample ensembles some tools have been previously developed, such as VEDA [189, 190], but they rely on a legacy web-based environment where the simulations and data handling are carried-out elsewhere which difficult using interactive features or to easily access and visualize off-line simulations. Here, we propose the use of an interactive simulations tool: dForce. The dynamic AFM simulator (dForce) is a powerful scipythonic code [135] devoted to the numerical solution of two types of non-linear differential equations, namely: the point-mass (single-frequency) and Euler-Bernoulli (bimodal and multi-frequency) models. The software platform is designed to offer an interactive graphical user interface (GUI) [141]. To this end, the simulator

breaks up the tip-surface ensemble into easy recognizable sub-systems, such as: the cantilever operational parameters, the medium properties, the tip-sample interaction forces and the numerical integrator precision. Under this framework several analyses can be performed. On one hand, the standard curves analysis of the AFM observables, such as the amplitude, phase, deflection, energy dissipation, among others. On the other hand, the user is able to depict any customized individual or multiple curves for further time, distance or frequency domains analyses. Furthermore, an internal version of dForce offers advanced features like the parametric plots devoted mainly to multifrequency AFM modeling, off-line plotting and comparison of simulations and multiprocessor computing has been also implemented to run exhaustive simulations efficiently. In summary, dForce envisions several applications such as: understanding dynamic AFM experiments, testing new theoretical approaches, optimizing imaging conditions or provide an a priori insight to complex phenomena that may occur within single and multifrequency force microscopy situations. The simulations platform development is based on the numerical libraries, visualization and widgets of a scientific python programming stack as depicted in figure A.1.

A.2 Simulator back and front-end design

The simulation platform developed within this thesis offers: an easy to use graphical environment, robustness¹ and reproducibility in its results. Moreover, from the developer perspective dForce's design is flexible (open for creating new extensions) and easy to maintain. Figure A.1 summarizes the back and front-end design followed to implement the ambitious software design.

The *in-house* developed source-code for the platform covers: modeling the tip-motion (point-mass and the modified Euler-Bernoulli), over 10 different force models, the data handling/storage implementation, the GUI and a customized multiprocessor and multicore module for stand-alone workstations (see figure A.1). The latter has been also adapted to High Performance Computing environments (HPC) whereby we carried out the parametric analyses in this thesis.

A.2.1 Performance in scientific computing

The numerical computation libraries used in scientific computing have been carefully optimized since its first version in *Fortran*, passing through new implementations in *C++* and nowadays promising programming languages such as *Python*, *Julia*, among others. However, only few studies compare the trade-offs in performance of the aforementioned languages. In figure A.2(a) a comparison of the CPU time as a function of the

¹In computer science, robustness is the ability of a computer to cope with errors during execution.

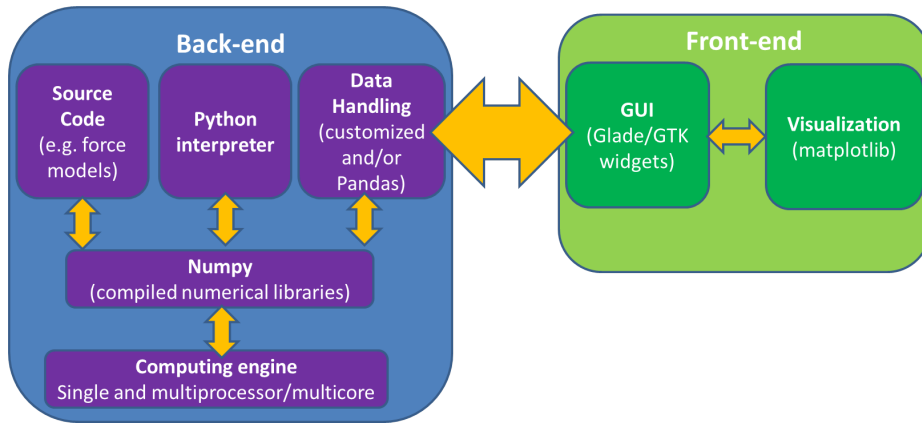


Figure A.1: Back and front-end design of the dynamic force microscopy simulator (dForce).

domain/grid size (data arrays computing steps of double-precision floating point numbers) for *C++* (2 compilers GCC and LLVM), *Fortran* (GCC) and *Python* (CPython and PyPy packages) is shown [139]. *Fortran* gives the shortest execution times for any domain grid sizes which are followed by the timing of *C++* and in the last position the Authors found the *Python* variants (CPython and PyPy packages). Although the newest variants of *Python* for numerical computing (e.g. PyPy) improves drastically the performance whereby for small domain grid sizes can be very close to the values obtained with *C++*. On the other hand, in figure A.2(b), an additional memory footprint analysis has been performed in terms of the peak memory use dependence on the domain/grid size [139]. In this case, the memory footprint analysis is referred to the amount of temporary memory used for array manipulation whereby all cases present an asymptotic reduce of the peak memory in use. Interestingly, for the highest domain size the *Python* variants, CPython and PyPy reaches the footprint of *Fortran* and *C++*, respectively. Remarkably, the growing and promising interest [191] in the optimization mechanisms of *Python* computational packages relies also on the design features that this language offer [135, 133], some of them are described in section A.2.

Furthermore regarding the numerical integration procedures as explained earlier in Chapter 2, we have wrapped them from the numerical integration solvers using the Numpy wrapper *f2py*. Then, the expected performance decrease is minimized in regard to the numerical integration procedures and thus the optimization mechanisms are aimed to the performance metrics on arrays handling discussed in the former paragraph.

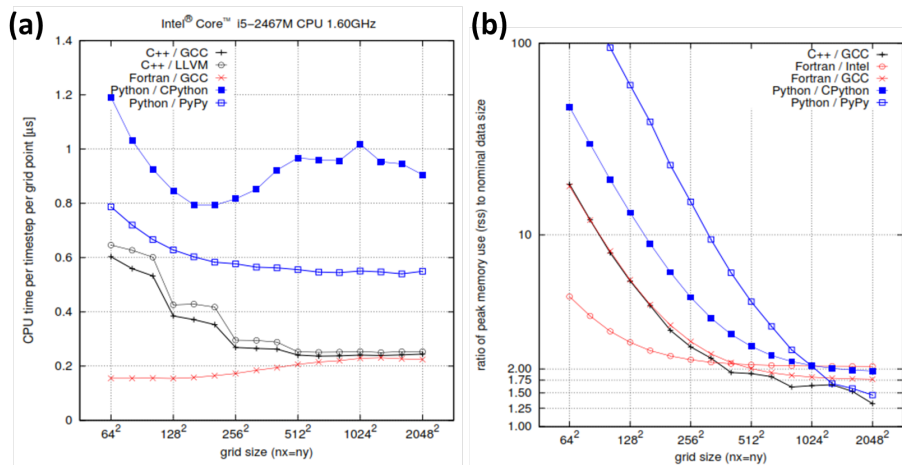


Figure A.2: Performance comparisons for C++ (2 compilers GCC and LLVM), Fortran (GCC) and Python (CPython and PyPy packages). (a) CPU time as a function of the arrays main/grid size. (b) Memory footprint as a function of the arrays main/grid size. Adapted from [139].

A.3 Outlook and discussion

In order to overcome the performance trade-offs shown in the above section, we have planned to further speed-up our python code by using a *Biggish Data*² encapsulation strategy. Such strategy aims to store previous simulations results gathered from dForce developers and contributors and store them in a reduced Hierarchical Data Format [192] whereby all contributors have access and can analyze or visualize the dropped results online without re-computing them. Thanks to the ubiquity of *Python* there are tools within its programming stack that meet our new developments needs [135, 133]. Some preliminary test for a 20 GBytes data batch (of around ten thousand simulation cases) have been carried out where the largest accessing and visualization time relies within two minutes. In addition, the access time to the simulation data can be enhanced by using sampling algorithms based on the simulations events of every data batch. Furthermore, this new perspective in dynamic force simulations can be applied to the massive multivariate analysis of the dynamic AFM variables both simulated and/or experimental ones. One recent example of it within the AFM community is the analysis of biggish experimental data to interpret conductive phenomena on complex oxide interfaces [193].

²Collection of data sets (\sim Gigabytes) that tend to be large and complex and become difficult to process by using on-hand data management tools.

Appendix B

Expression to estimate the peak forces of soft material in liquids

B.1 Asymptotic approximations of the peak interaction forces of soft material in liquids

Asymptotic approximation methods can be used to obtain a closed-form solution of a differential equation based on single or multivariate functions $f(a, b, c, \dots)$ defined within a range of initial conditions [133, 149, 194]. Within those methods we have chosen the multivariate regression analysis to obtain a parametrized expression of peak interaction according to Tataru's model (see Chapter 2).

B.1.1 Multivariate regression analysis

In the framework of this thesis, it is of particular interest to provide a scaling law based on the Tataru's contact mechanics [95, 160, 195]. Such expression has been explicitly obtained for estimating the peak forces of soft materials in liquid. To this end an extensive range of simulations have been performed to obtain the peak forces whereby the parameters used have been summarized in Table B.1.

The multivariate regression analysis has been applied to the aggregated AFM variables, namely: A_{sp} , A_0 , k , Q , R_{eff} and E_{eff} . Then, we assume that the total interaction force can be written as linear cascade function of the total interaction force, leading to,

$$F_{peak} = f(E_{eff}(R_{eff}(Q(k(A_0(A_{sp})))))) \quad (\text{B.1})$$

Parameters	E_s (MPa)	A_0 (nm)	k (N/m)	A_{sp}	Q	R_t
Ranges	30-300	1-10	0.1-1.0	$(0.7-0.95)A_0$	1-5	5,7.5,10
Steps	270	20	10	6	5	—

Table B.1: Simulations ranges for multivariate regression analysis of Tataru's peak forces. Note that in all cases two constants have been set to $E_t=170$ GPa and $R_s=0.8 R_t$.

where $1/E_{eff} = (1 - \nu_t^2)/E_t + (1 - \nu_s^2)/E_s$ and $1/R_{eff} = 1/R_t + 1/R_s$ are the effective Young modulus and tip radius, respectively. Other variables have been previously described in Chapter 4. Equation B.1 reflects a highly complex function of six aggregated AFM variables. In order to reduce the complexity of this function the regression algorithm (*scipy optimize curve fit* [180]) initial guess has been based on equation 5.4. Hence, equation B.1 can be rewritten as,

$$F_{peak} = B_F A_0 \left[1 - \left(\frac{A_{sp}}{A_0} \right)^2 \right]^{1/2} \quad (\text{B.2})$$

where $B_F = f(E_{eff}(R_{eff}(Q(k))))$ is the force coefficient as a function of four aggregated variables k , Q , R_{eff} and E_{eff} . Once the linear coefficient B_F has been obtained we have used both *scipy optimize curve fit* and *scikitlearn model fit* algorithms to obtain,

$$F_{Tataru}^{par} = A_0 \left[\left(\frac{24k}{11Q} \right)^{3/4} E_{eff}^{1/4} R_{eff}^{1/4} - \left(\frac{E_{eff} R_{eff}}{2^{11/2}} \right) \right] \left[1 - \left(\frac{A_{sp}}{A_0} \right)^2 \right]^{1/2} \quad (\text{B.3})$$

with an cumulative cascade coefficient of determination given by $R^2 \sim 0.85$ which in a sixth order multivariate regression analysis is acceptable. However, we have pushed this limit further by using further optimization techniques of the *scikitlearn package* [196]. Letting $R^2 \sim 0.91$ whereby equation becomes,

$$F_{Tataru}^{par} = A_0 \left[\left(\frac{24k}{11Q} \right)^{3/4} E_{eff}^{1/4} R_{eff}^{1/4} - \left(\frac{E_{eff} R_{eff}}{2^{11/2}} \right) \right] \left[1 - \left(\frac{A_{sp}}{A_0} \right)^2 \right]^{2/5} \quad (\text{B.4})$$

This equation has been compared to numerical simulations and it shows a good agreement (see Chapter 5) within the ranges described in Table B.1. However, it could be easily extended to further operational parameters but no correlation coefficient could be guaranteed for that case.

Bibliography

- [1] G. Binnig, H. Rohrer, C. Gerber, and E. Weibel. Tunneling through a controllable vacuum gap. *Applied Physics Letters* **40**(2), 178–180 (1982)
- [2] G. Binnig, C. F. Quate, and C. Gerber. Atomic Force Microscopy. *Physical Review Letters* **56**(9), 930–933 (1986)
- [3] A. San Paulo and R. Garcia. High-Resolution Imaging of Antibodies by Tapping-Mode Atomic Force Microscopy: Attractive and Repulsive Tip-Sample Interaction Regimes. *Biophysical Journal* **78**(3), 1599–1605 (2000)
- [4] D. Martinez-Martin, E. T. Herruzo, C. Dietz, J. Gomez-Herrero, and R. Garcia. Noninvasive Protein Structural Flexibility Mapping by Bimodal Dynamic Force Microscopy. *Phys. Rev. Lett.* **106**, 198101 (2011)
- [5] D. J. Müller, F. Schabert, and G. E. A. Buldt. Imaging purple membranes in aqueous solutions at sub-nanometer resolution by atomic force microscopy. *Biophysical Journal* **68**(5), 1681–1686 (1995)
- [6] J. Mou, S. Sheng, R. Ho, and Z. Shao. Chaperonins GroEL and GroES: views from atomic force microscopy. *Biophys J* **71**(4), 2213–21 (1996)
- [7] C. Möller, M. Allen, V. Elings, A. Engel, and D. J. Müller. Tapping-Mode Atomic Force Microscopy Produces Faithful High-Resolution Images of Protein Surfaces. *Biophysical Journal* **77**(2), 1150–1158 (1999)
- [8] D. J. Müller and A. Engel. Atomic force microscopy and spectroscopy of native membrane proteins. *Nature Protocols* **2**(9), 2191–2197 (2007)
- [9] A. Engel and D. J. Müller. Observing single biomolecules at work with the atomic force microscope. *Nature Structural Biology* **7**(9), 715–718 (2000)
- [10] D. J. Müller, G. Büldt, and A. Engel. Force-induced conformational change of bacteriorhodopsin. *Journal of Molecular Biology* **249**(2), 239–243 (1995)

- [11] Y. Sugimoto, P. Pou, M. Abe, P. Jelinek, R. Perez, S. Morita, and O. Custance. Chemical identification of individual surface atoms by atomic force microscopy. *Nature* **446**(7131), 64–67 (2007)
- [12] O. Custance, R. Perez, and S. Morita. Atomic force microscopy as a tool for atom manipulation. *Nature Nanotechnology* **4**(12), 803–810 (2009)
- [13] L. Gross, F. Mohn, P. Liljeroth, J. Repp, F. J. Giessibl, and G. Meyer. Measuring the Charge State of an Adatom with Noncontact Atomic Force Microscopy. *Science* **324**(5933), 1428–1431 (2009)
- [14] D. Han, S. Pal, Y. Liu, and H. Yan. Folding and cutting DNA into reconfigurable topological nanostructures. *Nature Nanotechnology* **5**(10), 712–717 (2010)
- [15] N. Kodera, D. Yamamoto, R. Ishikawa, and T. Ando. Video imaging of walking myosin V by high-speed atomic force microscopy. *Nature* **468**(7320), 72–76 (2010)
- [16] R. Garcia and R. Perez. Dynamic atomic force microscopy methods. *Surface Science Reports* **47**(6-8), 197–301 (2002)
- [17] H. J. Butt, B. Cappella, and M. Kappl. Force measurements with the atomic force microscope: Technique, interpretation and applications. *Surface Science Reports* **59**(1-6), 1–152 (2005)
- [18] G. Meyer and N. M. Amer. Optical-beam-deflection atomic force microscopy: The NaCl (001) surface. *Applied Physics Letters* **56**(21), 2100–2101 (1990)
- [19] D. Anselmeti, R. Luethi, and E. Meyer. Attractive-mode imaging of biological materials with dynamic force microscopy. *Nanotechnology* **5**(87) (1994)
- [20] E.-L. Florin, M. Radmacher, B. Fleck, and H. E. Gaub. Atomic force microscope with magnetic force modulation. *Review of Scientific Instruments* **65**(3), 639–643 (1994)
- [21] S. J. O’Shea, M. E. Welland, and J. B. Pethica. Atomic force microscopy of local compliance at solid-liquid interfaces. *Chemical Physics Letters* **223**(4), 336–340 (1994)
- [22] W. Han, S. Lindsay, and T. Jing. A magnetically driven oscillating probe microscope for operation in liquids. *Applied Physics Letters* **69**(26), 4111–4113 (1996)
- [23] N. Umeda, S. Ishizaki, and H. Uwai. Scanning attractive force microscope using photothermal vibration. *J. Vac. Sci. Technol. B* **9**(1318) (1991)

- [24] D. Ramos, J. Tamayo, J. Mertens, and M. Calleja. Photothermal excitation of microcantilevers in liquids. *Journal of Applied Physics* **99**(12), 124904 (pages 8) (2006)
- [25] R. Garcia. *Amplitude Modulation AFM in Liquid* (Wiley-VCH, Weinheim, Germany, 2010)
- [26] T. R. Albrecht, P. Grütter, D. Horne, and D. Rugar. Frequency modulation detection using high-kantilevers for enhanced force microscope sensitivity. *Journal of Applied Physics* **69**(2), 668–673 (1991)
- [27] F. J. Giessibl. Forces and frequency shifts in atomic-resolution dynamic-force microscopy. *Physical Review B* **56**(24), 16010 (1997)
- [28] J. Melcher, D. Martínez-Martín, M. Jaafar, J. Gómez-Herrero, and A. Raman. High-resolution dynamic atomic force microscopy in liquids with different feedback architectures. *Beilstein J Nanotechnol* **4**, 153–63 (2013)
- [29] M. Jaafar, D. Martínez-Martín, M. Cuenca, J. Melcher, A. Raman, and J. Gómez-Herrero. Drive-amplitude-modulation atomic force microscopy: From vacuum to liquids. *Beilstein Journal of Nanotechnology* **3**, 336–344 (2012)
- [30] D. Platz, E. A. Tholen, D. Pesen, and D. B. Haviland. Intermodulation atomic force microscopy. *Applied Physics Letters* **92**(15), 153106–3 (2008)
- [31] S. Jesse, S. V. Kalinin, R. Proksch, A. P. Baddorf, and B. J. Rodriguez. The band excitation method in scanning probe microscopy for rapid mapping of energy dissipation on the nanoscale. *Nanotechnology* **18**(43), 435503 (2007)
- [32] S. D. Solares and G. Chawla. Frequency response of higher cantilever eigenmodes in bimodal and trimodal tapping mode atomic force microscopy. *Meas. Sci. Tech.* **21**, 125502 (2010)
- [33] O. Sahin, S. Magonov, C. Su, C. F. Quate, and O. Solgaard. An atomic force microscope tip designed to measure time-varying nanomechanical forces. *Nat. Nanotechnol.* **2**, 507–514 (2007)
- [34] O. Sahin. Time-varying tip-sample force measurements and steady-state dynamics in tapping-mode atomic force microscopy. *Phys. Rev. B* **77**, 115405–6 (2008)
- [35] O. Sahin and N. Erina. High-resolution and large dynamic range nanomechanical mapping in tapping-mode atomic force microscopy. *Nanotechnology* **19**, 445717 (2008)
- [36] M. D. Aksoy and A. Atalar. Force spectroscopy using bimodal frequency modulation atomic force microscopy. *Phys. Rev. B* **83**, 075416 (2011)

- [37] R. Garcia and E. T. Herruzo. The emergence of multifrequency force microscopy. *Nat Nanotechnol* **7**(4), 217–26 (2012)
- [38] T. R. Rodriguez and R. Garcia. Compositional mapping of surfaces in atomic force microscopy by excitation of the second normal mode of the microcantilever. *Applied Physics Letters* **84**(3), 449–451 (2004)
- [39] R. Proksch. Multifrequency, repulsive-mode amplitude-modulated atomic force microscopy. *Applied Physics Letters* **89**(11), 113121–3 (2006)
- [40] N. F. Martinez, S. Patil, J. R. Lozano, and R. Garcia. Enhanced compositional sensitivity in atomic force microscopy by the excitation of the first two flexural modes. *Appl. Phys. Lett.* **89**, 153115–3 (2006)
- [41] R. Garcia and R. Proksch. Nanomechanical mapping of soft matter by bimodal force microscopy. *European Polymer Journal* **49**(8), 1897–1906 (2013)
- [42] J. R. Lozano and R. Garcia. Theory of Multifrequency Atomic Force Microscopy. *Physical Review Letters* **100**(7), 076102–4 (2008)
- [43] J. R. Lozano and R. Garcia. Theory of phase spectroscopy in bimodal atomic force microscopy. *Phys. Rev. B* **79**, 014110–4 (2009)
- [44] N. F. Martinez, J. R. Lozano, E. T. Herruzo, F. Garcia, C. Richter, T. Sulzbach, and R. Garcia. Bimodal atomic force microscopy imaging of isolated antibodies in air and liquids. *Nanotechnology* **19**, 384011 (2008)
- [45] E. T. Herruzo and R. Garcia. Theoretical study of the frequency shift in bimodal FM-AFM by fractional calculus. *Beilstein J Nanotechnol* **3**, 198–206 (2012)
- [46] E. T. Herruzo, A. P. Perrino, and R. Garcia. Fast nanomechanical spectroscopy of soft matter. *Nat Commun* **5**, 3126 (2014)
- [47] Y. Gan. Atomic and subnanometer resolution in ambient conditions by atomic force microscopy. *Surface Science Reports* **64**(3), 99–121 (2009)
- [48] T. P. Weihs, Z. Nawaz, S. P. Jarvis, and J. B. Pethica. Limits of imaging resolution for atomic force microscopy of molecules. *Applied Physics Letters* **59**(27), 3536–3538 (1991)
- [49] H. Hölscher, W. Allers, U. D. Schwarz, A. Schwarz, and R. Wiesendanger. Interpretation of “true atomic resolution” images of graphite (0001) in noncontact atomic force microscopy. *Phys. Rev. B* **62**, 6967–6970 (2000)
- [50] U. Schwarz. *Theory of soft and biomatter*. 1a ed^{ön}. (Ruprecht-Karls-University Heidelberg, 2009)

- [51] L. D. Landau and E. M. Lifshitz. *Theory of Elasticity*. 2 ed^{ón}. (Pergamon, Oxford, 1970)
- [52] F. Ohnesorge and G. Binnig. True Atomic Resolution by Atomic Force Microscopy Through Repulsive and Attractive Forces. *Science* **260**(5113), 1451–1456 (1993)
- [53] A. San Paulo *et al.*. High-resolution imaging of antibodies by tapping-mode atomic force microscopy: Attractive and repulsive tip-sample interaction regimes. *Biophys. J.* **78**, 1599–1605 (2000)
- [54] S. Patil, N. F. Martinez, J. R. Lozano, and R. Garcia. Force microscopy imaging of individual protein molecules with sub-pico Newton force sensitivity. *Journal of Molecular Recognition* **20**(6), 516–523 (2007)
- [55] S. N. Magonov and D. H. Reneker. CHARACTERIZATION OF POLYMER SURFACES WITH ATOMIC FORCE MICROSCOPY. *Annual Review of Materials Science* **27**(1), 175–222 (1997)
- [56] S. Scheuring, J. Seguin, S. Marco, D. Levy, B. Robert, and J.-L. Rigaud. Nanodissection and high-resolution imaging of the Rhodospseudomonas viridis photosynthetic core complex in native membranes by AFM. *Proceedings of the National Academy of Sciences* **100**(4), 1690–1693 (2003)
- [57] J. K. H. Horber and M. J. Miles. Scanning Probe Evolution in Biology. *Science* **302**(5647), 1002–1005 (2003)
- [58] H. Yamada, K. Kobayashi, T. Fukuma, Y. Hirata, T. Kajita, and K. Matsushige. Molecular Resolution Imaging of Protein Molecules in Liquid Using Frequency Modulation Atomic Force Microscopy. *Applied Physics Express* **2**(9), 095007 (2009)
- [59] L. Gross, F. Mohn, N. Moll, P. Liljeroth, and G. Meyer. The Chemical Structure of a Molecule Resolved by Atomic Force Microscopy. *Science* **325**(5944), 1110–1114 (2009)
- [60] T. Ando, N. Kodera, E. Takai, D. Maruyama, K. Saito, and A. Toda. A high-speed atomic force microscope for studying biological macromolecules. *Proceedings of the National Academy of Sciences* **98**(22), 12468–12472 (2001)
- [61] E. T. Herruzo, H. Asakawa, T. Fukuma, and R. Garcia. Three-dimensional quantitative force maps in liquid with 10 piconewton, angstrom and sub-minute resolutions. *Nanoscale* **5**, 2678–2685 (2013)
- [62] J. B. Marion. *Classical Dynamics of Particles and Systems* (Academic Press, New York-London, 1998)

- [63] S. Basak, A. Raman, and S. V. Garimella. Hydrodynamic loading of microcantilevers vibrating in viscous fluids. *Journal of Applied Physics* **99**(11), 114906 (pages 10) (2006)
- [64] J. Chen, R. K. Workman, D. Sarid, and R. Hoper. Numerical simulations of a scanning force microscope with a large-amplitude vibrating cantilever. *Nanotechnology* **5**(4), 199 (1994)
- [65] S. J. O'Shea and M. E. Welland. Atomic Force Microscopy at Solid-Liquid Interfaces. *Langmuir* **14**(15), 4186–4197 (1998)
- [66] J. E. Greenspon. Vibrations of Cross-Stiffened and Sandwich Plates with Application to Underwater Sound Radiators. *The Journal of the Acoustical Society of America* **33**(11), 1485–1497 (1961)
- [67] X. Xu and A. Raman. Comparative dynamics of magnetically, acoustically, and Brownian motion driven microcantilevers in liquids. *Journal of Applied Physics* **102**(3), 034303–8 (2007)
- [68] E. T. Herruzo and R. Garcia. Frequency response of an atomic force microscope in liquids and air: Magnetic versus acoustic excitation. *Applied Physics Letters* **91**(14), 143113–3 (2007)
- [69] D. Kiracofe and A. Raman. Quantitative force and dissipation measurements in liquids using piezo-excited atomic force microscopy: a unifying theory. *Nanotechnology* **22**(48), 485502 (2011)
- [70] A. San Paulo and R. Garcia. Tip surface forces, amplitude, and energy dissipation in amplitude modulation (tapping mode) force microscopy. *Phys. Rev. B* **64**, 193411 (2001)
- [71] L. Nony, R. Boisgard, and J. P. Aime. Nonlinear dynamical properties of an oscillating tip-cantilever system in tapping mode. *J. Chem. Phys* **111**(1615) (1999)
- [72] L. Wang. Analytical descriptions of the tapping-mode atomic force microscopy response. *Appl. Phys. Lett.* **73**(3781) (1998)
- [73] K. Schroeter, A. Petzold, T. Henze, and T. Albrecht. Quantitative analysis of scanning force microscopy data using harmonic models. *Macromolecules* **42-44**(1114)
- [74] S. Hu and A. Raman. Analytical formulas and scaling laws for peak interaction forces in dynamic atomic force microscopy. *Applied Physics Letters* **91**(12), 123106–3 (2007)

- [75] T. Kowalewski and J. Legleiter. Imaging stability and average tip-sample force in tapping mode atomic force microscopy. *J. Appl. Phys.* **99**, 064903 (2006)
- [76] T. R. Rodriguez and R. Garcia. Theory of Q control in atomic force microscopy. *Appl. Phys. Lett.* **82**(26), 4821 (2003)
- [77] W. H. Press, B. P. Flannery, S. A. Teukolsky, and W. T. Vetterling. *Numerical Recipes in FORTRAN 77: The Art of Scientific Computing*. 1a ed^{on}. (Cambridge University Press, Cambridge, 1992)
- [78] J. Tamayo and R. Garcia. Deformation, Contact Time, and Phase Contrast in Tapping Mode Scanning Force Microscopy. *Langmuir* **12**(18), 4430–4435 (1996)
- [79] R. Garcia and A. San Paulo. Attractive and repulsive tip-sample interaction regimes in tapping-mode atomic force microscopy. *Physical Review B* **60**(7), 4961 (1999)
- [80] Garcia and A. San Paulo. Amplitude curves and operating regimes in dynamic atomic force microscopy. *Ultramicroscopy* **82**(1-4), 79–83 (2000)
- [81] H. V. Guzman, A. P. Perrino, and R. Garcia. Peak forces in high-resolution imaging of soft matter in liquid. *ACS Nano* **7**(4), 3198–204 (2013)
- [82] B. Gotsmann, C. Seidel, B. Anczykowski, and H. Fuchs. Conservative and dissipative tip-sample interaction forces probed with dynamic AFM. *Physical Review B* **60**(15), 11051 (1999)
- [83] B. Kumar, P. Pifer, A. Giovengo, and J. Legleiter. The effect of set point ratio and surface Young's modulus on maximum tapping forces in fluid tapping mode atomic force microscopy. *Journal of Applied Physics* **107**(4) (2010)
- [84] S. Timoshenko. *Vibration problems in engineering* (1990)
- [85] L. Meirovitch. *Principles and Techniques of Vibrations*. 2a ed^{on}. (Prentice Hall, Upper Saddle River, NJ, 2000)
- [86] R. W. Stark and W. M. Heckl. Fourier transformed atomic force microscopy: tapping mode atomic force microscopy beyond the Hookian approximation. *Surface Science* **457**(1-2), 219–228 (2000)
- [87] O. D. Payton, L. Picco, M. J. Miles, M. E. Homer, and A. R. Champneys. Modelling oscillatory flexure modes of an atomic force microscope cantilever in contact mode whilst imaging at high speed. *Nanotechnology* **23**(26), 265702 (2012)
- [88] J. W. S. Rayleigh and R. B. Lindsay. *The Theory of Sound*. 2a ed^{on}. (Dover Publications, Mineola, NY, 1976)

- [89] J. Melcher, S. Hu, and A. Raman. Equivalent point-mass models of continuous atomic force microscope probes. *Applied Physics Letters* **91**(5), 053101–3 (2007)
- [90] J. E. Sader. Frequency response of cantilever beams immersed in viscous fluids with applications to the atomic force microscope. *Journal of Applied Physics* **84**(1), 64–76 (1998)
- [91] K. L. Johnson, K. Kendall, and A. D. Roberts. SURFACE ENERGY AND CONTACT OF ELASTIC SOLIDS. *Proceedings of the Royal Society of London Series a-Mathematical and Physical Sciences* **324**(1558), 301–313 (1971)
- [92] K. L. Johnson. *Contact Mechanics*. 2a ed^{on}. (Cambridge University Press, Cambridge, 1985)
- [93] B. V. Derjaguin, V. M. Muller, and Y. P. Toporov. EFFECT OF CONTACT DEFORMATIONS ON ADHESION OF PARTICLES. *Journal of Colloid and Interface Science* **53**(2), 314–326 (1975)
- [94] H. Hertz. On the Contact of Rigid Elastic Solids and on Hardness. *Ch 6: Assorted Papers* (1882)
- [95] Y. Tatara. Extensive Theory of Force-Approach Relations of Elastic Spheres in Compression and in Impact. *J. Eng. Mater. Technol* **111**, 163–168 (1989)
- [96] P. M. Hoffmann, S. Jeffery, J. B. Pethica, H. Ozgur Ozer, and A. Oral. Energy Dissipation in Atomic Force Microscopy and Atomic Loss Processes. *Physical Review Letters* **87**(26), 265502 (2001)
- [97] R. Garcia, C. J. Gomez, N. F. Martinez, S. Patil, C. Dietz, and R. Magerle. Identification of nanoscale dissipation processes by dynamic atomic force microscopy. *Physical Review Letters* **97**(1), 016103–4 (2006)
- [98] J. C. Williams and S. D. Solares. Towards 4-dimensional atomic force spectroscopy using the spectral inversion method. *Beilstein J Nanotechnol* **4**, 87–93 (2013)
- [99] M. Chyasnovichyus, S. L. Young, and V. V. Tsukruk. Probing of Polymer Surfaces in the Viscoelastic Regime. *Langmuir* (2014)
- [100] S. Hudlet, M. Saint Jean, B. Roulet, J. Berger, and C. Guthmann. Electrostatic forces between metallic tip and semiconductor surfaces. *Journal of Applied Physics* **77**(7), 3308–3314 (1995)
- [101] A. Gil, J. Colchero, J. Gomez-Herrero, and A. M. Baro. Electrostatic force gradient signal: resolution enhancement in electrostatic force microscopy and improved Kelvin probe microscopy. *Nanotechnology* **14**(2), 332–340 (2003)

- [102] S. Sadewasser, P. Carl, T. Glatzel, and M. C. Lux-Steiner. Influence of uncompensated electrostatic force on height measurements in non-contact atomic force microscopy. *Nanotechnology* **15**(2), S14 (2004)
- [103] Y. Martin and H. K. Wickramasinghe. Magnetic imaging by “force microscopy” with 1000 [Å-ring] resolution. *Applied Physics Letters* **50**(20), 1455–1457 (1987)
- [104] J. J. Saenz, N. Garcia, P. Grutter, E. Meyer, H. Heinzelmann, R. Wiesendanger, L. Rosenthaler, H. R. Hidber, and H.-J. Guntherodt. Observation of magnetic forces by the atomic force microscope. *Journal of Applied Physics* **62**(10), 4293–4295 (1987)
- [105] S. Schreiber, M. Savla, D. V. Pelekhov, D. F. Iscru, C. Selcu, P. C. Hammel, and G. Agarwal. Magnetic force microscopy of superparamagnetic nanoparticles. *Small* **4**(2), 270–278 (2008)
- [106] J. Israelachvili. *Intermolecular and Surface Forces*. 2a ed^{on}. (Elsevier Academic Press, London, 2005)
- [107] L. Bergstrom. Hamaker constants of inorganic materials. *Advances in Colloid and Interface Science* **70**, 125–169 (1997)
- [108] P. D. Ashby, L. W. Chen, and C. M. Lieber. Probing intermolecular forces and potentials with magnetic feedback chemical force microscopy. *Journal of the American Chemical Society* **122**(39), 9467–9472 (2000)
- [109] J. Boussinesq. Application des Potentials a l’etude de l’equilibre et du mouvement des solids eelastiques (1885)
- [110] D. Tabor. Surface forces and surfaces interactions. *J. Colloid Interface Sci.* **58**, 2–23 (1976)
- [111] D. S. Dugdale. Yielding of steel sheets containing slits. *J. Mech. Phys. Solids* **8**, 100–108 (1960)
- [112] D. S. Grierson, E. E. Flater, and R. W. Carpick. Accounting for the JKR-DMT transition in adhesion and friction measurements with atomic force microscopy. *Journal of Adhesion Science and Technology* **19**(3), 291–311 (2005)
- [113] K. Johnson and J. Greenwood. An Adhesion Map for the Contact of Elastic Spheres. *Journal of Colloid and Interface Science* **192**(2), 326–333 (1997)
- [114] D. Maugis. Adhesion of spheres: The JKR-DMT transition using a dugdale model. *Journal of Colloid and Interface Science* **150**(1), 243–269 (1992)

- [115] M. A. Lantz, S. J. O'Shea, M. E. Welland, and K. L. Johnson. Atomic-force-microscope study of contact area and friction on NbSe₂. *Phys. Rev. B* **55**(10776) (1997)
- [116] R. Carpick, D. Ogletree, and M. Salmeron. Lateral stiffness: A new nanomechanical measurement for the determination of shear strengths with friction force microscopy. *Applied Physics Letters* **70**(12), 1548–1550 (1997)
- [117] R. W. Carpick and M. Salmeron. Scratching the Surface: Fundamental Investigations of Tribology with Atomic Force Microscopy. *Chem. Rev.* **97**(4), 1163–1194 (1997)
- [118] B. Luan and M. O. Robbins. The breakdown of continuum models for mechanical contacts. *Nature* **435**, 929–932 (2005)
- [119] W. N. Unertl. Implications of contact mechanics models for mechanical properties measurements using scanning force microscopy. *Journal of Vacuum Science & Technology A* **17**(4), 1779–1786 (1999)
- [120] H. J. Butt and M. Kappl. Surface and interfacial forces. *Wiley-VCH Verlag GmbH & Co. KGaA* pags. 120–125 (2010)
- [121] H. V. Guzman and R. Garcia. Peak forces and lateral resolution in amplitude modulation force microscopy in liquid. *Beilstein J Nanotechnol* **4**, 852–9 (2013)
- [122] H.-J. Butt, M. Jaschke, and W. Ducker. Measuring surface forces in aqueous electrolyte solution with the atomic force microscope. *Bioelectrochemistry and Bioenergetics* **38**(1), 191–201 (1995)
- [123] L. D. Landau, E. M. Lifshitz, L. P. Pitaevskii, and M. J. Kearsley. Electrodynamics of continuous media
- [124] H. Li, X. Peng, L. Wu, M. Jia, and H. Zhu. Surface Potential Dependence of the Hamaker Constant. *Journal of Physical Chemistry C* **113**(11), 4419 (2009)
- [125] D. J. Müller, D. Fotiadis, S. Scheuring, S. A. Müller, and A. Engel. Electrostatically balanced subnanometer imaging of biological specimens by atomic force microscope. *Biophys. J.* **76**(2), 1101–11 (1999)
- [126] N. W. Tschoegl. *The Phenomenological Theory of Linear Viscoelastic Behavior* (1989)
- [127] S. R. Cohen and E. Kalfon-Cohen. Dynamic nanoindentation by instrumented nanoindentation and force microscopy: a comparative review. *Beilstein J Nanotechnol* **4**, 815–33 (2013)

- [128] D. Tranchida, Z. Kiflie, S. Acierno, and S. Piccarolo. Nanoscale mechanical characterization of polymers by atomic force microscopy (AFM) nanoindentations: viscoelastic characterization of a model material. *Measurement Science and Technology* **20**(9), 095702 (2009)
- [129] A. Raman, S. Trigueros, A. Cartagena, A. Stevenson, M. Susilo, E. Nauman, and S. Antoranz Contera. Mapping nanomechanical properties of live cells using multi-harmonic atomic force microscopy. *Nat. Nanotech.* **6**, 809–814 (2011)
- [130] D. G. Yablon, J. Grabowski, and I. Chakraborty. Measuring the loss tangent of polymer materials with atomic force microscopy based methods. *Measurement Science and Technology* **25**(5), 055402 (2014)
- [131] A. Cartagena and A. Raman. Local viscoelastic properties of live cells investigated using dynamic and quasi-static atomic force microscopy methods. *Biophys. J.* **106**(5), 1033–43 (2014)
- [132] W. H. Press, B. P. Flannery, S. A. Teukolsky, and W. T. Vetterling. *Numerical Recipes in Fortran 77: The Art of Scientific Computing*. 2 ed^{on}. (Cambridge University Press, 1992)
- [133] E. Bressert. *Scipy and Numpy: An Overview for Developers..* 1a ed^{on}. (O’Reilly Media., 2012)
- [134] M. Lutz. *Learning Python*. 2 ed^{on}. (O’Reilly, 2003). URL <http://www.bibsonomy.org/bibtex/2bb91dd9fe3197e784e32556d62fd46e5/wikier>
- [135] E. Jones, T. Oliphant, and P. Peterson. SciPy: Open Source Scientific Tools for Python (2001), URL <http://www.scipy.org>; <http://www.bibsonomy.org/bibtex/24b71448b262807648d60582c036b8e02/neurokernel>
- [136] J. Van der Plas. Why Python is Slow: Looking Under the Hood (2014), URL <http://jakevdp.github.io/blog/2014/05/09/why-python-is-slow>
- [137] A. B. Downey, J. Elkner, and C. Meyers. *How to Think Like a Computer Scientist: Learning with Python*. 2nd edition ed^{on}. (Green Tea Press, Wellesley, Massachusetts, 2002). L^AT_EX-Quellen: <http://openbookproject.net/thinkCSpy/thinkCSpy2.tgz> – <http://www.ibiblio.org/obp/thinkCSpy/> – last visited 3rd October 2008
- [138] P. Peterson. F2PY: a tool for connecting Fortran and Python programs. *IJCSE* **4**(4), 296–305 (2009)

- [139] S. Arabas, D. Jarecka, A. Jaruga, and M. Fijalkowski. Formula translation in Blitz++, NumPy and modern Fortran: A case study of the language choice trade-offs. *Scientific Programming* **22**(3) (2014)
- [140] S. M. Baxter, S. W. Day, J. S. Fetrow, and S. J. Reisinger. Scientific software development is not an oxymoron. *PLoS Comput. Biol.* **2**(9), e87 (2006)
- [141] L. Pautet and S. Tardieu. GLADE: a framework for building large object-oriented real-time distributed systems. In *Object-Oriented Real-Time Distributed Computing, 2000. (ISORC 2000) Proceedings. Third IEEE International Symposium on*, pags. 244–251 (2000)
- [142] J. D. Hunter. Matplotlib: A 2D Graphics Environment. *Computing in Science and Engineering* **9**(3), 90–95 (2007)
- [143] A. J. Howard, R. R. Rye, and J. E. Houston. Nanomechanical basis for imaging soft materials with tapping mode atomic force microscopy. *J. Appl. Phys.* **79**(1885) (1996)
- [144] I. Chakraborty and D. G. Yablon. Cantilever energy effects on bimodal AFM: phase and amplitude contrast of multicomponent samples. *Nanotechnology* **24**(47), 475706 (2013)
- [145] J. Tamayo and R. Garcia. Relationship between phase shift and energy dissipation in tapping-mode scanning force microscopy. *Applied Physics Letters* **73**(20), 2926–2928 (1998)
- [146] R. Proksch and D. G. Yablon. Loss tangent imaging: Theory and simulations of repulsive-mode tapping atomic force microscopy. *Applied Physics Letters* **100**(7), 073106 (2012)
- [147] I. M. Ward and J. Sweeney. *Mechanical Properties of Solid Polymers* (2004)
- [148] J. R. Lozano. Teoría de Microscopia de Fuerzas Bimodal y su aplicación para la medida de propiedades superficiales a escala nanométrica. *Universidad Autónoma de Madrid* (2010)
- [149] J. A. Sanders and V. F. *Averaging Methods in Nonlinear Dynamical Systems* (Springer, New York, 1985)
- [150] A. San Paulo and R. Garcia. Unifying theory of tapping-mode atomic-force microscopy. *Physical Review B* **66**(4), 041406 (2002)
- [151] D. Kiracofe and A. Raman. Nonlinear dynamics of the atomic force microscope at the liquid-solid interface. *Phys. Rev. B* **86**, 205405 (2012)

- [152] T. G. Fox and P. J. Floy. Viscosity molecular weight and viscosity temperature relationships for polystyrene and polyisobutylene. *J. Am. Chem. Soc.* **70**(7) (1948)
- [153] S. Tripathy and E. J. Berger. Measuring viscoelasticity of soft samples using atomic force microscopy. *J Biomech Eng* **131**(9), 094507 (2009)
- [154] M. L. Williams, R. F. Landel, and J. D. Ferry. The Temperature Dependence of Relaxation Mechanisms in Amorphous Polymers and Other Glass-forming Liquids. *J. Am. Chem. Soc.* **77**, 3701–3707 (1955)
- [155] R. Lakes. *Viscoelastic Materials* (2009)
- [156] N. Aksel. On the impact of a rigid sphere on a viscoelastic half-space. *Ingenieur Archiv* **56**, 38–54 (1986)
- [157] J. P. Cleveland, B. A. Anczykowski, S. E., and E. V. B. Energy dissipation in tapping-mode atomic force microscopy. *Applied Physics Letters* **72**(20), 2613–2615 (1998)
- [158] J. Tamayo and R. Garcia. Effects of elastic and inelastic interactions on phase contrast images in tapping-mode scanning force microscopy. *Applied Physics Letters* **71**(16), 2394–2396 (1997)
- [159] J. Melcher, C. Carrasco, X. Xu, J. L. Carrascosa, J. Gomez-Herrero, P. J. de Pablo, and A. Raman. Origins of phase contrast in the atomic force microscope in liquids. *Proceedings of the National Academy of Sciences of the United States of America* **106**(33), 13655–13660 (2009)
- [160] Y. Tatara. Large Deformations of Ruber Sphere under Diametral Compression. *JSME* **36**, 190–196 (1993)
- [161] D. Ebeling, B. Eslami, and S. D. J. Solares. Visualizing the Subsurface of Soft Matter: Simultaneous Topographical Imaging, Depth Modulation, and Compositional Mapping with Triple Frequency Atomic Force Microscopy. *ACS Nano* **7**(11), 10387–10396 (2013)
- [162] G. Stan, S. D. Solares, B. Pittenger, N. Erina, and C. Su. Nanoscale mechanics by tomographic contact resonance atomic force microscopy. *Nanoscale* **6**(2), 962–9 (2014)
- [163] K. K. Mandadapu, S. Govindjee, and M. R. Mofrad. On the cytoskeleton and soft glassy rheology. *Journal of Biomechanics* **41**(7), 1467–1478 (2008)
- [164] T. Uchihashi, R. Iino, T. Ando, and H. Noji. High-speed atomic force microscopy reveals rotary catalysis of rotorless F^o-ATPase. *Science* **333**(6043), 755–8 (2011)

- [165] I. Casuso, J. Khao, M. Chami, P. Paul-Gilloteaux, M. Husain, J.-P. Duneau, H. Stahlberg, J. N. Sturgis, and S. Scheuring. Characterization of the motion of membrane proteins using high-speed atomic force microscopy. *Nat Nanotechnol* **7**(8), 525–9 (2012)
- [166] D. M. Czajkowsky and Z. Shao. The human IgM pentamer is a mushroom-shaped molecule with a flexural bias. *Proceedings of the National Academy of Sciences* **106**(35), 14960–14965 (2009)
- [167] H. Edwards, J. F. Jorgensen, J. Dagata, Y. Strausser, and J. Schneir. Influence of data analysis and other factors on the repeatability of vertical SPM calibration Measurements. *J. Vac. Sci. Technol. B* **16**(2) (1998)
- [168] S. Santos, V. Barcons, H. K. Christenson, D. J. Billingsley, W. A. Bonass, J. Font, and N. H. Thomson. Stability, resolution, and ultra-low wear amplitude modulation atomic force microscopy of DNA: Small amplitude small set-point imaging. *Applied Physics Letters* **103**(6), 063702–063702–4 (2013)
- [169] T. R. Rodriguez and R. Garcia. Tip motion in amplitude modulation (tapping-mode) atomic-force microscopy: Comparison between continuous and point-mass models. *Applied Physics Letters* **80**(9), 1646–1648 (2002)
- [170] J. Melcher, X. Xu, and A. Raman. Multiple impact regimes in liquid environment dynamic atomic force microscopy. *Applied Physics Letters* **93**(9), 093111–3 (2008)
- [171] K. Voitchovsky. Anharmonicity, solvation forces, and resolution in atomic force microscopy at the solid-liquid interface. *Phys. Rev. E* **88**, 022407 (2013)
- [172] X. Xu, J. Melcher, S. Basak, R. Reifenberger, and A. Raman. Compositional Contrast of Biological Materials in Liquids Using the Momentary Excitation of Higher Eigenmodes in Dynamic Atomic Force Microscopy. *Phys. Rev. Lett.* **102**, 060801 (2009)
- [173] D. Ramos, J. Tamayo, J. Mertens, and M. Calleja. Photothermal excitation of microcantilevers in liquids. *Journal of Applied Physics* **99**(12), 124904–124904–8 (2006)
- [174] J. A. Sanders and F. Verhulst. *Averaging Methods in Nonlinear Dynamical Systems*. 2 ed^{on}. (Springer, 1985)
- [175] X. Xu, C. Carrasco, P. J. de Pablo, J. Gomez-Herrero, and A. Raman. Unmasking imaging forces on soft biological samples in liquids when using dynamic atomic force microscopy: a case study on viral capsids. *Biophys. J.* **95**(5), 2520–8 (2008)

- [176] S. Santos, A. Verdaguer, and M. Chiesa. The effects of adsorbed water layers on the apparent height of nanostructures in ambient amplitude modulation atomic force microscopy. *J. Chem. Phys* **137**(4) (2012)
- [177] D. Ebeling and S. D. Solares. Amplitude modulation dynamic force microscopy imaging in liquids with atomic resolution: comparison of phase contrasts in single and dual mode operation . *Nanotechnology* **24**(135702) (2013)
- [178] J. Legleiter and T. Kowalewski. Insights into fluid tapping-mode atomic force microscopy provided by numerical simulations. *Applied Physics Letters* **87**(16), 163120–3 (2005)
- [179] S. D. Solares, J. Chang, J. Seog, and A. U. Kareem. Utilization of simple scaling laws for modulating tip-sample peak forces in atomic force microscopy characterization in liquid environments. *Journal of Applied Physics* **110**(9), 094904 (2011)
- [180] F. J. Blanco-Silva. Learning SciPy for Numerical and Scientific Computing (2013)
- [181] R. W. Stark. Spectroscopy of higher harmonics in dynamic atomic force microscopy. *Nanotechnology* **15**(3), 347 (2004)
- [182] R. Proksch. Bimodal Dual AC Imaging of Collagen Fiber Ultra-structure (2009)
- [183] A. M. Gigler, C. Dietz, M. Baumann, N. F. Martinez, R. García, and R. W. Stark. Repulsive bimodal atomic force microscopy on polymers. *Beilstein J Nanotechnol* **3**, 456–63 (2012)
- [184] B. Eslami, D. Ebeling, and S. D. Solares. Trade-offs in sensitivity and sampling depth in bimodal atomic force microscopy and comparison to the trimodal case. *Beilstein Journal of Nanotechnology* **5**, 1144–1151 (2014)
- [185] S. D. Solares. Challenges and complexities of multifrequency atomic force microscopy in liquid environments. *Beilstein J Nanotechnol* **5**, 298–307 (2014)
- [186] S. Santos. Anharmonicity in multifrequency atomic force microscopy. *Arxiv* (2014)
- [187] C. Dietz, E. T. Herruzo, J. R. Lozano, and R. Garcia. Nanomechanical coupling enables detection and imaging of 5 nm superparamagnetic particles in liquid. *Nanotechnology* **22**(12), 125708 (2011)
- [188] D. Kiracofe, A. Raman, and D. Yablon. Multiple regimes of operation in bimodal AFM: understanding the energy of cantilever eigenmodes. *Beilstein J Nanotechnol* **4**, 385–93 (2013)

- [189] J. Melcher, S. Hu, and A. Raman. Invited Article: VEDA: A web-based virtual environment for dynamic atomic force microscopy. *Review of Scientific Instruments* **79**(6), 061301 (pages 11) (2008)
- [190] D. Kiracofe, J. Melcher, and A. Raman. Gaining insight into the physics of dynamic atomic force microscopy in complex environments using the VEDA simulator. *Rev Sci Instrum* **83**(1), 013702 (2012)
- [191] J. Van der Plas. Why Python is the Last Language You'll Have to Learn (2012), URL <http://jakevdp.github.io/blog/2014/05/09/why-python-is-the-last>
- [192] L. Gosink, J. Shalf, K. Stockinger, K. Wu, and W. Bethel. HDF5-FastQuery: Accelerating Complex Queries on HDF Datasets using Fast Bitmap Indices. In *Scientific and Statistical Database Management, 2006. 18th International Conference on*, pages 149–158 (2006)
- [193] E. Strelcov, A. Belianinov, Y.-H. Hsieh, S. Jesse, A. P. Baddorf, Y.-H. Chu, and S. V. Kalinin. Deep data analysis of conductive phenomena on complex oxide interfaces: physics from data mining. *ACS Nano* **8**(6), 6449–57 (2014)
- [194] Z. Iveicic, A. Conolly, and J. Van der Plas. *Statistics, Data Mining, and Machine Learning in Astronomy: A Practical Python Guide for the Analysis of Survey Data* (Princeton University Press, 2014)
- [195] A. Ikai, R. Afrin, and H. Sekiguchi. Pulling and Pushing protein Molecules by AFM. *Current Nanoscience* **3**, 17–29 (2007)
- [196] F. Pedregosa, G. Varoquaux, A. Gramfort, V. Michel, B. Thirion, O. Grisel, M. Blondel, P. Prettenhofer, R. Weiss, V. Dubourg, J. VanderPlas, A. Passos, D. Cournapeau, M. Brucher, M. Perrot, and E. Duchesnay. Scikit-learn: Machine Learning in Python. *Journal of Machine Learning Research* **12**, 2825–2830 (2011)

Publications

During the course of this thesis we published our results in several scientific journals:

1. Peak forces in high-resolution imaging of soft-matter in liquid
Horacio V. Guzman, Alma P. Perrino and R. Garcia
ACS Nano **7** (4), 3198-3204, 2013
2. Peak forces and lateral resolution in amplitude modulation force microscopy in liquid
Horacio V. Guzman and R. Garcia
Beilstein J. Nanotechnol. **4**, 852-859, 2013
3. Dynamic force microscopy simulator (dForce): Interactive platform for understanding force microscopy experiments
Horacio V. Guzman, Pablo D. Garcia and R. Garcia
Submitted to the Beilstein Journal of Nanotechnology.
4. AM-AFM peak force scaling law for soft and finite elastic samples
Horacio V. Guzman and R. Garcia
Under submission.
5. Retrieving the peak viscoelastic interactions from AM-AFM operation at different timescales
Horacio V. Guzman and R. Garcia
Manuscript in preparation.
6. Gentle peak force modulation in Bimodal AM
Horacio V. Guzman and R. Garcia
Manuscript in preparation.